Springer Tracts in Modern Physics 242

S.C. Pancholi

Exotic Nuclear Excitations

Springer

Springer Tracts in Modern Physics

Volume 242

For further volumes:
http://www.springer.com/series/426

Springer Tracts in Modern Physics

Springer Tracts in Modern Physics provides comprehensive and critical reviews of topics of current interest in physics. The following fields are emphasized: elementary particle physics, solid-state physics, complex systems, and fundamental astrophysics.

Suitable reviews of other fields can also be accepted. The editors encourage prospective authors to correspond with them in advance of submitting a manuscript. For reviews of topics belonging to the above mentioned fields, they should address the responsible editor, otherwise the managing editor.

See also springer.com

S. C. Pancholi

Exotic Nuclear Excitations

Springer

S. C. Pancholi
Inter University Accelerator Centre
New Delhi 110067
India
scpancholi@hotmail.com

ISSN 0081-3869 e-ISSN 1615-0430
ISBN 978-1-4419-8037-3 e-ISBN 978-1-4419-8038-0
DOI 10.1007/978-1-4419-8038-0
Springer New York Dordrecht Heidelberg London

Library of Congress Control Number: 2011923071

Printed on acid-free paper

Springer is part of Springer Science+Business Media (www.springer.com)

Foreword

Nuclei are very special objects. They carry energy and angular momentum like any other macroscopic objects. At the same time, being quantum mechanical entities, they carry it in two different ways—as collective rotations and aligned single particle motions. This unique property of nuclei has given rise to range of exotic research topics in nuclear structure studies. Starting with the discovery of rotational alignment and band crossing phenomenon in the early 1970s, several other topics on exotic nuclear excitations are of immense current interest such as rotational alignment and band crossings, magnetic rotation, triaxial strong deformation and wobbling motion and chirality in nuclei.

I am happy that one of my old-time friend and colleague Prof. Suresh C. Pancholi, with his long career in teaching and research in nuclear structure physics at one of the premier Universities in India, the University of Delhi, and at several Laboratories abroad has chosen to bring out this unique monograph. While there is no doubt that this monograph will be a very valuable resource to the young researchers in our universities and institutions, this will also fill a major vacuum in good quality and up-to-date text books across the world in contemporary nuclear physics.

I personally wish all the best for his endeavour.

Bangaluru, India
May 21, 2010

V. S. Ramamurthy

Preface

This monograph on high spin physics is geared towards the beginners in research or the young researchers, in the exciting field of high spin nuclear structure physics. New and interesting phenomena have and are being discovered in this field which is providing a microscopic insight into the behaviour of nuclei under the extreme conditions of high excitation energy, highest spins and abnormal neutron-to-proton ratios. The quest for achieving the highest spin states has resulted in remarkable success in this direction. An attempt has been made in this monograph to provide the reader an up-to-date knowledge of some of the recent exotic phenomena at high spins in a collective and consolidated manner. The topics covered are the rotational alignment and bandcrossings, magnetic rotation, triaxial strong deformation and wobbling motion and chirality in nuclei. The earliest discovered is the phenomenon of bandcrossings which is generally known as backbending in nuclei. This discovery led to great excitement and interest in high spin nuclear spectroscopy and has been responsible for the present development so that a very large volume of useful information is available now. Magnetic rotation is a relatively newly discovered phenomenon in which the generation of angular momentum in nuclei is caused by the 'shears mechanism'. It gives rise to rotation-like magnetic dipole bands in nearly spherical nuclei. Axially symmetric shapes in nuclei are known for the last several decades. Recently, success was achieved in finding the occurrence of stable triaxial shapes in odd-Z Lu nuclei at high spins through the observation of wobbling motion at high quadrupole deformation. Although chirality is known in other fields like chemistry, the search for the observation of chirality is being extensively pursued presently in particle physics—in nuclei at moderate spins. Chirality can also provide evidence for the existence of stable triaxial shapes in nuclei.

Due to the monograph nature of this volume, I have purposely left out a number of other very interesting phenomena. These are identical bands, superdeformation and energy correlation in superdeformed states known as C_4 symmetry, hyperdeformation, smooth band termination, enhanced and highly deformed bands, particle–hole excitations, tetrahedral symmetry, isomers at high spins, research area in neutron-rich nuclei providing new physics concepts in nuclear physics in nuclei away from the line of beta stability, etc., to name some of these observations.

The key contributors to this field of research activity are the parallel development of heavy-ion accelerators providing a large variety of heavy-ion beams and gamma detector arrays with large photopeak detection efficiencies. A new avenue in high spin nuclear spectroscopy is now emerging with the development of gamma-ray tracking arrays which are likely to enhance the gamma-ray detection efficiency by several folds.

The emphasis throughout the book has been on a simple and up-to-date treatment of the topics covered. The pre-requisites for a proper appreciation are basic and advanced courses in nuclear physics and nuclear models as well as measurement techniques of observables like gamma-ray energies, intensities, multi-fold coincidences, angular correlations or distributions, linear polarisation, internal conversion coefficients, short lifetime (picosecond range) of excited states, etc. and instrumentation and data analysis methods.

I very gratefully acknowledge the encouragement and support that I received from Professor Deepak Pental, Vice Chancellor, University of Delhi.

The major part of the work on the monograph was carried out at the Inter University Accelerator Centre (IUAC), New Delhi. I am grateful to Dr. Amit Roy, Director, IUAC, and Dr. R. K. Bhowmik, Senior Scientist, IUAC, for providing excellent work atmosphere and allowing me to avail of the facilities.

This work would not have been possible without enthusiastic support that I received from a number of my colleagues and friends in India and abroad. Especially, I would like to acknowledge the advice and comments that I received from Professors Ashok Kumar Jain, Mark Riley and Herbert Hübel. Dr. Anukul Dhal helped me in the preparation of the manuscript. I am thankful to him for the same.

This monograph is based upon the works done by a large number of physicists whose painstaking investigations contributed to the advancement of knowledge. I am indebted to them.

Last but not the least, I thank my family—my wife Rani, daughter Bela, son Vineet, daughter-in-law Ranju and grand-daughter Meghna for their patience, tolerance and perseverance during the course of this project.

The work on the monograph was catalysed and supported by the Department of Science and Technology, under its Utilisation of Scientific Expertise of Retired Scientists Scheme. This is gratefully acknowledged.

New Delhi
April 11, 2010

Suresh C. Pancholi

Contents

Chapter 1
Rotational Alignment and Bandcrossings

1.1 Introduction

In the year 1971, in ^{160}Dy [1] nucleus, a discontinuity in the pattern of gamma-ray spectra normally observed in the decay of rotational states, was discovered at angular momentum, $I \sim 14\hbar$. This was interpreted in [2] as due to the decoupling of a pair of high-j nucleons from the rotating nuclear core and subsequent alignment of their angular momenta along the rotation axis at particular rotational frequency. A few years later, in 1977, a second discontinuity was observed in the gamma-ray spectra at angular momentum, $I \sim 28\hbar$ in ^{158}Er [3]. These two were the most significant discoveries in the initial phases of high spin physics. Most of the present day knowledge and the huge amount of information both experimental and theoretical, in a very large number of nuclei at high spins, owe its existence to the interest developed as a result of these discoveries. As will be explained later in this chapter, the rotation alignment of high-j low-Ω pairs of nucleons manifests as bandcrossing (popularly known as 'backending') between rotational bands. This mode of quasiparticle excitation is imposed on the collective nuclear rotational motion.

Since these early discoveries and the quest to populate and investigate nuclei at the highest spins, a number of different types of bandcrossings at high rotational frequencies involving pairs of quasineutrons and pairs of quasiprotons in nuclei in different mass regions, have been found and understood in terms of the cranked shell model (CSM). Such experimental investigations were made possible due to the availability of heavy-ion beams from accelerators and the parallel development of gamma detector arrays with large photopeak detection efficiencies (up to ~9%). In the present chapter, an attempt is made to give the reader a glimpse of this bandcrossing phenomenon through a first order description.

A number of articles which discuss this topic in details exist in the literature [4–11]. A short highly educative movie by Professor Mark Riley and group beautifully explains the phenomenon of rotational alignment and backbending. This can be accessed at: http://www.physics.fsu.edu/TheBackBender/.

S. C. Pancholi, *Exotic Nuclear Excitations,* Springer Tracts in Modern Physics 242,
DOI 10.1007/978-1-4419-8038-0_1, © Springer Science+Business Media, LLC 2011

1.2 Rotational Alignment and Bandcrossings

The discovery of the discontinuity in the gamma-ray spectrum mentioned above was observed in an experiment to investigate the high spin states in the even–even nucleus ^{160}Dy, using the ^{160}Gd (α, 4n) reaction at 43 MeV α-particle beam energy by Johnson, Ryde and Sztarkier [1]. The gamma–gamma coincidences were detected in a two 43 cm^3 Ge (Li) detector set-up. From the experimentally measured gamma-ray energies, the effective moment of inertia, $2\mathcal{J}/\hbar^2\{=(4I-2)/[E(I)-E(I-2)]\}$ was calculated and plotted as a function of square of rotational frequency, $(\hbar\omega)^2\{=(1/4)E\gamma^2\}$. This plot exhibited a deviation from the normal monotonous increase of moment of inertia, at $I=14\hbar$ onwards to the highest observed spin of $18\hbar$. The backbending of the moment of inertia generated tremendous interest and excitement. The numerous investigations that followed it, paved the way for the modern era in high spin nuclear structure physics.

The above experimental observation was explained by Stephens and Simon [2] in terms of Coriolis effects on high-j low-Ω particles due to rotational motion of the nucleus. The strong Coriolis force $\omega \cdot \vec{j}$ gradually breaks up the pairing correlations and decouples the particles from the core. It (the Coriolis force) tends to align the particle angular momentum, j with that of the rotor. The alignment tendency is stronger, the larger the value of j for the particle. The maximal aligned spin for two nucleons in a pure-j shell (e.g. a pair of neutrons in $i_{13/2}$ orbital) is $2j-1$ (i.e. $j+j-1$). Therefore, in an even–even rare-earth nucleus, for a pair of $i_{13/2}$ neutrons, an angular momentum of $12\hbar$ can be obtained through the rotation alignment of the pair along the rotation axis. The energy cost for breaking the nucleon pair is about twice the odd–even mass difference (~2Δ). In the situation where the Fermi level is close to the low-Ω orbitals, the alignment will give rise to a 2-quasineutron rotational band. The ground state rotational band and the 2-quasineutron band will cross each other at a certain critical rotational frequency, called the bandcrossing frequency, $\hbar\omega_c$. This will happen as the 2-quasineutron band will drop in energy with respect to the continuation of the ground state band above the crossing frequency (spin) due to the decrease in pairing energy.

A number of other theoretical explanations were provided in several of the works available in literature, e.g. that using the angular momentum projection method [12].

Let us consider, as a typical case, the even–even nucleus ^{158}Er. Figure 1.1 shows the partial level scheme of ^{158}Er [13]. On the left of the figure is shown the positive parity ground state Yrast band with signature $\alpha=0$. This band is fed at spin $I=12\hbar$ by a 2-quasiparticle positive parity $\alpha=0$ band which is also Yrast. The states above spin $12\hbar$ on the left is the continuation of the ground state band. The Yrast 2-quasiparticle band is populated to high spins. In Fig. 1.2 are plotted the spin of the states of the Yrast bands as a function of energy of gamma-rays de-exciting the states. This figure shows two discontinuities in gamma-ray energies, one near $I=14\hbar$ and the other near $I=28\hbar$. In this discussion, particular attention will be given to these

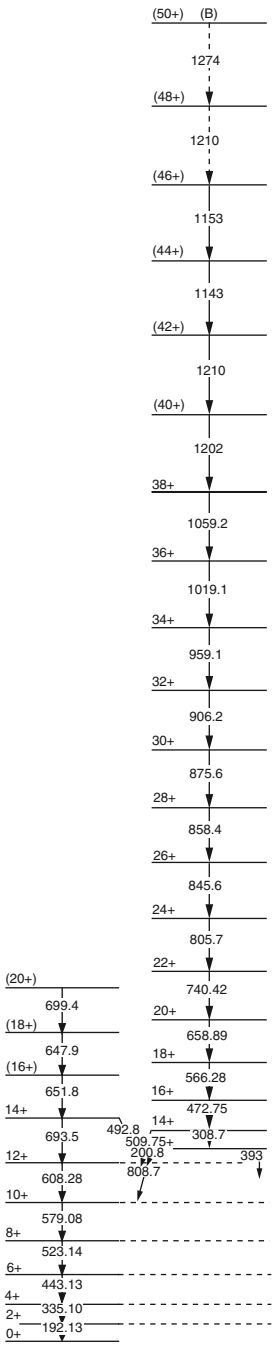

Fig. 1.1 Partial level scheme of ^{158}Er [13]. (Figure with permission reproduced in part from [13])

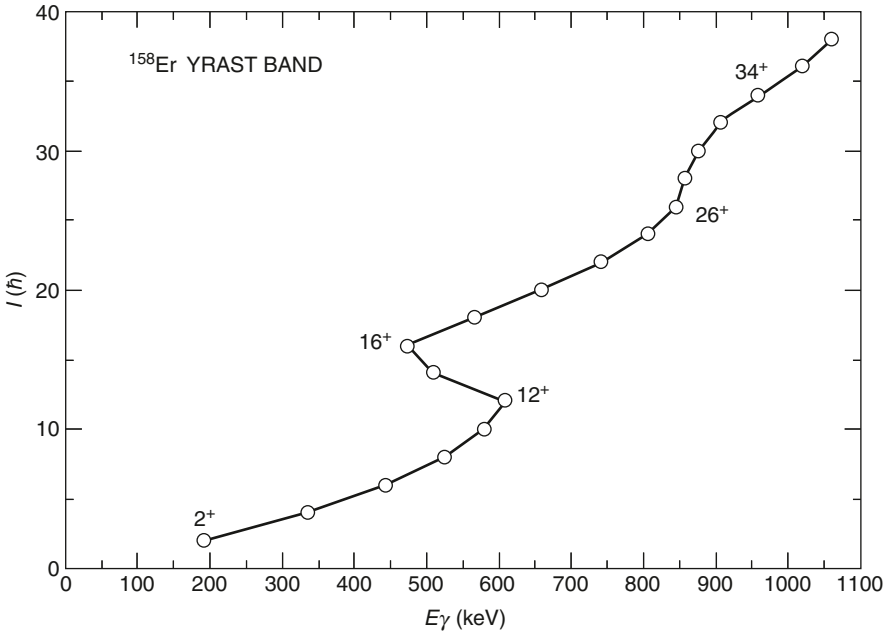

Fig. 1.2 Plot of spin vs. $E\gamma$, for the Yrast rotational band in the even–even ^{158}Er nucleus. (Data from [13])

discontinuities. The rotational bands shown in Fig. 1.1 are interpreted in terms of the CSM to characterize the bandcrossings (the discontinuities) and identify the quasiparticles which contribute to the band. The CSM calculations give the quasiparticle energies, e', in the rotating intrinsic frame (Routhians) and aligned quasiparticle angular momenta, $i_x\hbar$, along the rotation (x) axis. To facilitate comparison between experiment and theory, the values of e' and i_x as a function of rotational frequency, $\hbar\omega$, are extracted from the experimental data. This extraction is done through a transformation prescription which is available in the literature, e.g. [4, 14, 15]. The data for the positive parity Yrast band in ^{158}Er are plotted in Fig. 1.3 [15]. In the bottom panel is the plot of the quasiparticle energies as a function of rotational frequency. The 0-quasiparticle band (the ground state band) is crossed by a 2-quasiparticle band at a bandcrossing frequency, $\hbar\omega_c = 0.272$ MeV. This, as we will see in due course is due to the lowest neutron $\nu i_{13/2}$ pair decoupling from the core and aligning their angular momenta along the axis of rotation. In simple terms, this critical frequency can be thought of as the angular frequency of rotation at which the Coriolis plus the centrifugal energies of the high-j low-Ω aligning $\nu i_{13/2}$ neutrons balances the pairing energy of the aligning neutrons. Further on in rotational frequency, another band crosses the 2-quasiparticle band at $\hbar\omega_c = 0.427$ MeV. As mentioned earlier, this second bandcrossing in ^{158}Er was first observed in [3]. In the top panel of the figure, i_x is plotted as a function of $\hbar\omega$ from the same data.

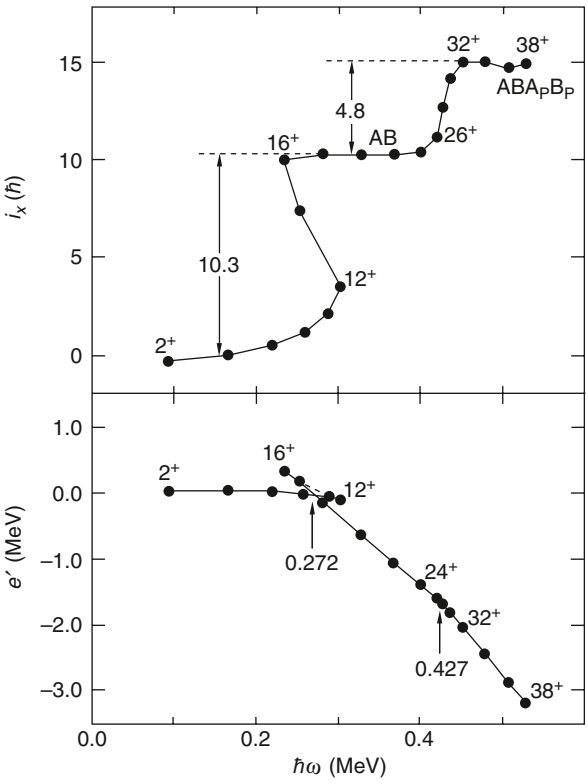

Fig. 1.3 Plots of quasiparticle energies, e', and aligned angular momenta, i_x, versus rotational frequency, $\hbar\omega$, for the Yrast band in ^{158}Er, using $\mathcal{J}_0 = 18.5$ MeV$^{-1}\hbar^2$ and $\mathcal{J}_1 = 85.0$ MeV$^{-3}\hbar^4$ in the parameterization of the ground state band. The bandcrossing frequencies, $\hbar\omega_c$, for the alignments are marked (↑) in the *bottom panel* and the aligned angular momentum gains, Δi_x mentioned in the *upper panel* [15]. (Figure in part reproduced with permission from [15])

This figure shows a typical backbending nature and a second bandcrossing which has a shape between a vertical and a gradual upbender. Also given in the figure are the alignment gains Δi_x (for the first backbending) = 10.3$\hbar$ and for the second bandcrossing $\Delta i_x = 4.8\hbar$.

Let us further characterize these bandcrossings. The experimental values of $\hbar\omega_c$ and Δi_x can be compared with the CSM predictions. Also, the bandcrossings in an even–even nucleus can be interpreted in terms of bandcrossings observed in the neighbouring odd-N and odd-Z nuclei, on the basis of the Pauli blocking arguments. Following these arguments, we examine the experimental data on bandcrossings in odd-Z ^{157}Ho [16] and odd-N ^{159}Er [17] nuclei. Plots of experimental values of aligned angular momentum, i (same as i_x), as a function of rotational frequency, $\hbar\omega$, for these nuclei are shown in Figs. 1.4 and 1.5, respectively. In ^{157}Ho, the first bandcrossing occurs at $\hbar\omega_c = 0.27$ MeV with an alignment gain of $\Delta i = 9.0\hbar$. This crossing has been identified to be due to the rotation alignment of AB pair of $i_{13/2}$ quasineutrons in the bands based on the lowest energy Ap and Bp proton orbitals. (A, B and Ap, Bp is the nomenclature for nucleon configurations used in the CSM. See Sect. 1.3.1 for details of these notations.) The bandcrossing frequency of

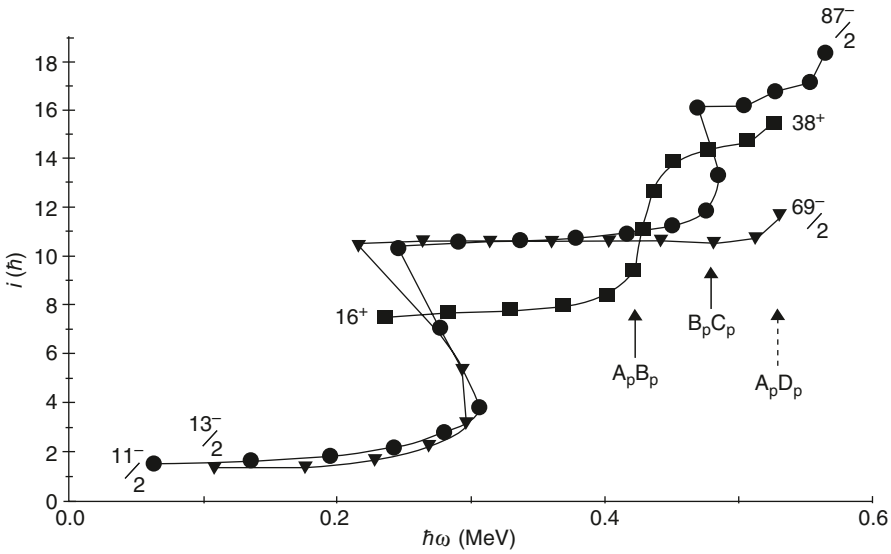

Fig. 1.4 Experimental values of aligned angular momentum, i (same as i_x), as a function of rotational frequency, $\hbar\omega$, for the bands based on Ap (•) and Bp (▼) configurations in the odd-Z nucleus ^{157}Ho [16]. Only data up to $\hbar\omega \sim 0.45$ MeV will be considered in the text. After alignment of 2-quasineutrons, the 3-quasiparticle configuration of these bands is ApAB and BpAB, respectively. A partial alignment plot for ^{158}Er from spin $I = 16^+$–38^+ is also shown. Alignments like, ApBp in ^{158}Er and BpCp and ApDp in ^{157}Ho are also marked. (Figure reproduced with permission from [16])

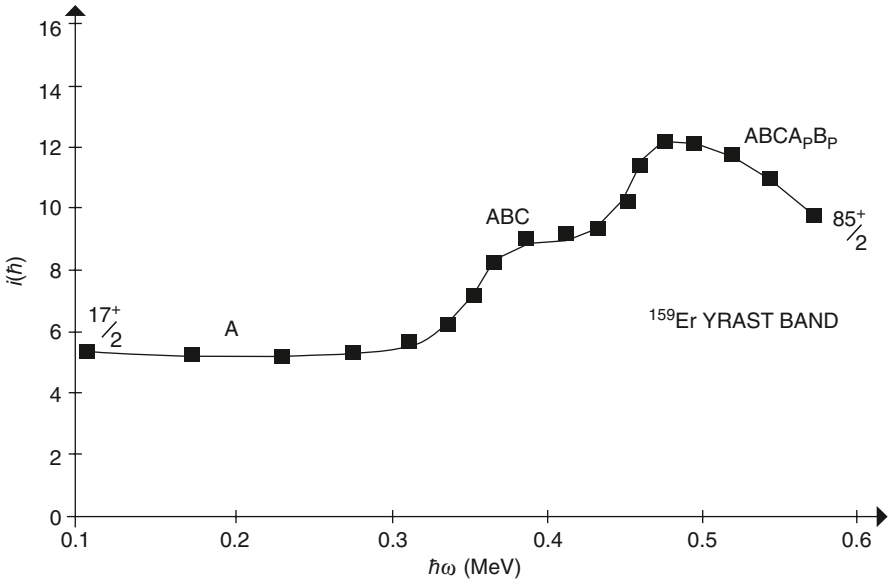

Fig. 1.5 Plot of experimental aligned angular momentum, i (same as i_x), as a function of rotational frequency, $\hbar\omega$, for the positive parity Yrast band in odd-N ^{159}Er nucleus [17]. (Figure in part reproduced with permission from [17])

$\hbar\omega_c = 0.27$ MeV and an alignment gain of $\Delta i = 9.0\hbar$ in ^{157}Ho are in agreement with the results $\hbar\omega_c = 0.272$ MeV and the alignment gains $\Delta i_x = 10.3\hbar$ for the first bandcrossing in ^{158}Er mentioned above. For ^{159}Er [14, 17], the aligned angular momenta for the bands based on A and B neutron configurations are $i_x = 5.8\hbar$ and $4.6\hbar$, respectively. In Fig. 1.5 [17], the alignment plot only for the A configuration in ^{159}Er is shown. These aligned angular momenta add up to $10.4\hbar$ as compared to $\Delta i_x = 10.3\hbar$ obtained for the first bandcrossing in ^{158}Er. These results, therefore, firmly establish that the first bandcrossing in ^{158}Er is due to the rotation alignment of the lowest $\nu i_{13/2}$ AB quasineutron pair. In the same alignment plot (Fig. 1.5) in ^{159}Er [17], it is observed that the Yrast band based on A neutron configuration undergoes the first bandcrossing as a gradual upbend at $\hbar\omega_c = 0.355$ MeV. This crossing has been interpreted as due to the rotational alignment of the BC quasineutron pair because the AB bandcrossing is blocked as the Yrast band occupies trajectory A. The next gradual/upbend bandcrossing in ^{159}Er is found at a higher rotational frequency of $\hbar\omega_c = 0.453$ MeV [17]. This has been interpreted as the alignment of the lowest ApBp quasiproton pair [17, 18]. A similar bandcrossing has also been seen in the Yrast band of the neighbouring $N = 90$ isotone ^{160}Yb at $\hbar\omega_c = 0.42$ MeV [15, 19] which has been interpreted as due to the ApBp quasiproton pair. Independently, in the framework of a cranked Hartree-Fock-Bogoliubov (HFB) approach with particle number projection, it was suggested in [20] that this crossing at $I = 26$–30 in ^{158}Er is due to the rotational alignment of a pair of $h_{11/2}$ protons. In [21], through the cranked HFB method in the pairing +Q.Q model, a second backbend around $I = 26$ in ^{158}Er was also predicted due to the anti-pairing effect among protons. Based on these arguments and facts, it can be concluded that the second bandcrossing observed in the Yrast band of ^{158}Er (see Fig. 1.3) is due to the rotational alignment of the $\pi h_{11/2}$ ApBp quasiproton pair.

1.3 Systematics of Bandcrossings

A large body of experimental data exists in literature on bandcrossing(/alignment) frequencies, alignment gains and band interaction strengths for bandcrossings involving different aligning neutron and proton pairs at high spins in nuclei throughout the nuclear chart. Such data have been interpreted by comparison with the predictions of the CSM calculations and successfully and very widely utilized not only in the assignment of nucleon configurations to the crossing bands but also in unfolding the details of nuclear structure. The supportive pair blocking arguments have also proved very useful in data interpretation.

In this section, the nomenclature used in the CSM calculations to define the participating specific quasiparticles in bandcrossings will be outlined. It will be followed by a plot of quasiparticle trajectories (quasiparticle energies, e' in the rotating frame as a function of rotational frequency), as an example and the CSM predictions of bandcrossing frequencies and alignment gains from it. These are required

for an understanding of the systematics of bandcrossings described later in this section.

Excellent treatment of the CSM is available, e.g. see [4 and references therein].

1.3.1 Nomenclature for Quasiparticle Trajectories

In the CSM, the quasiparticle energies, e' in the rotating frame (called Routhians[1]), are calculated as a function of rotational frequency, $\hbar\omega$. At $\omega=0$, the levels are labelled by the asymptotic Nilsson quantum numbers $| Nn_z \hat{} \Omega |$ and at $\omega\neq 0$, the trajectories can be identified by the quantum numbers, parity (π) and signature (α). The short-hand notation used to label the quasiparticle trajectories in the model is described below. In the region of the neutron $\nu i_{13/2}$ and proton $\pi h_{11/2}$ intruder orbitals and the $h_{9/2}$, $f_{7/2}$ neutron orbitals, the alphabetic labelling convention is used [4, 23, 24]. The notations are: $A=(\pi, \alpha)_n=(+, ½)_1$, $B=(+, -½)_1$, $C=(+, ½)_2$, $D=(+, -½)_2$, for the lowest positive parity quasineutron trajectories from the $i_{13/2}$ intruder orbital and for the negative parity, $E=(\pi, \alpha)_n=(-, ½)_1$ and $F=(-, -½)_1$ quasineutron trajectories from the $h_{9/2}$ and $f_{7/2}$ orbitals respectively. At $\omega=0$, the levels A and B, C and D, E and F and G and H correspond to the Nilsson states [651, 3/2], [660, ½], [532, 3/2] and [521, 3/2], respectively. Similarly, $Ap=(-, -½)_1$, $Bp=(-, ½)_1$ and $Cp=(-, -½)_2$ for the lowest quasiproton trajectories from the mid-shell $h_{11/2}$ ($\Omega\sim 7/2$) orbitals. The subscript 'n' is the nth such aligned quasiparticle.

The experimental rotational band sequences are designated by (π, α) and by their quasiparticle composition. A band may have 0-quasiparticle composition (ground state band) in an even–even nucleus or a 1-quasineutron configuration A, B, C, etc., in an odd-N nucleus or a 1-quasiproton Ap, Bp etc., configuration in an odd-Z nucleus. The ground state band will have $(\pi, \alpha)=(+, 0)_1$. For 1-quasiparticle bands the (π, α) labelling is given above. Multi-quasiparticle bands may be based on 2-, 3-, 4- and higher quasiparticle configurations. For such bands, the parity, π is the product of the parities of individual quasiparticle orbitals and the signature, α is the sum of the single-quasiparticle values, e.g. AB band will have (π, α)=(+, 0). Further, bands of configurations ApAB, BpAB and 0-ABApBp will have (π, α)=(−, −½), (−, ½) and (+, 0), respectively.

The total signature, α, of a state is related to the total angular momentum I as follows [4]:

$$\alpha = \begin{cases} -1/2 \\ 1/2 \\ \\ 0 \\ 1 \end{cases} \quad \text{if} \quad I = \begin{cases} 3/2, 7/2, 11/2, \ldots \\ 1/2, 5/2, 9/2, \ldots \\ \\ 0, 2, 4, \ldots \\ 1, 3, 5, \ldots \end{cases}$$

[1] The term Routhian is used for excitation energy in the rotating frame, since the transformation from the laboratory to the intrinsic rotating frame is equivalent to Routh procedure [22] for a change of variables in classical mechanics.

1.3.2 Quasiparticle Trajectories

A typical simplified version of the plot of quasineutron energies, e', in the rotating frame as a function of rotational frequency, $\hbar\omega$, i.e. the quasineutron trajectories are shown in Fig. 1.6 for ^{160}Yb [19]. These energies were calculated in [19] using the CSM. In these calculations, the input parameters used were $\varepsilon_2 = 0.2$, $\varepsilon_4 = -0.02$, $\Delta n = 1.06$ MeV, $\lambda = 6.38\hbar\omega_o$ and $N = 90$. In this diagram, only the positive parity trajectories A, B, C and D (marked in the figure) are shown. As the nucleus rotates, the $\nu i_{13/2}$ particle begins to align their angular momenta along the axis of rotation until the pairing correlations for the two aligning neutrons are zero. The maximum aligned spin for the two nucleons in a pure-j shell is $(2j-1)$. Three different bandcrossings are shown by vertical arrows in the figure: AB bandcrossing at $\hbar\omega_c = 0.23$ MeV with a gain in aligned angular momentum, $\Delta i \approx 9.9\hbar$; BC bandcrossing at $\hbar\omega_c = 0.36$ MeV with $\Delta i \approx 6.6\hbar$ and AD band crossing at $\hbar\omega_c = 0.37$ MeV with $\Delta i \approx 7.2\hbar$. These bandcrossing frequencies and alignment gains can be compared with the corresponding experimental values to ascertain the quasiparticles which

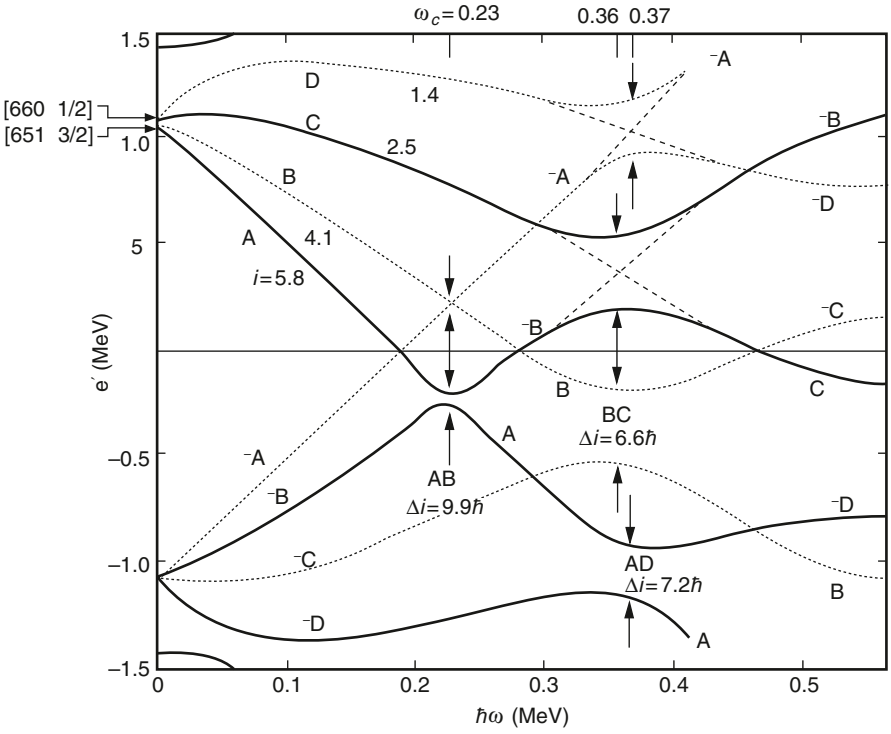

Fig. 1.6 Neutron quasiparticle energies, e', from CSM calculations, in the rotating frame as a function of rotational frequency, $\hbar\omega$ for a few selected trajectories (marked in the figure as A, B,…), in ^{160}Yb [19]. See text for details. (Figure reproduced with permission from [19])

contribute to a particular crossing band, thus assigning the quasiparticle configuration to a rotational band (see, e.g. Table 3 in [19]).

Comparison to experimental data is made by transforming the measured level energies and spins in the level scheme to the rotating frame. Standard prescriptions to perform this transformation are available in the literature, e.g. see [4, 14] and also see [11]. Experimental values of quasiparticle energies, e', aligned angular momenta, i_x (also written sometimes as only 'i') and rotational frequencies, $\hbar\omega$, are then obtained. Plots of e' and i_x as a function of $\hbar\omega$ are made (e.g. see Fig. 1.3) to determine the experimental values of bandcrossing frequencies $\hbar\omega_c$ and the gain in the aligned angular momentum Δi, in the bandcrossing. These values are compared to the predictions of the CSM.

In the following sub-sections, in large part, the discussion is limited to bandcrossing frequencies in the lowest energy neutron $\nu i_{13/2}$ AB bandcrossings and in the mass $A \sim 120$–130 nuclei, the proton $\pi h_{11/2}$ bandcrossings are also included. Specifically, the systematics of neutron $\nu i_{13/2}$ AB bandcrossings in even–even rare earth, evidence of decreased pairing energies in odd-N $A \sim 160$, bandcrossings in $A \sim 120$–130 and delayed bandcrossings in odd-Z $A \sim 160$–170 nuclei, are discussed. A discussion on bandcrossings in the magnetic rotational bands is given in Chap. 2 on 'Magnetic Rotation'.

1.3.3 Neutron $\nu i_{13/2}$ AB Bandcrossing Frequencies in Even–Even Nuclei

Let us consider the crossing of 0-quasiparticle bands (ground state bands) and the 2-quasineutron $\nu i_{13/2}$ AB bands in even–even rare-earth nuclei. The quasineutron $\nu i_{13/2}$ AB bandcrossing frequencies, $\hbar\omega_c$, for these bands versus neutron number, N, in even–even Er ($Z=68$), Yb ($Z=70$), Hf ($Z=72$) and W ($Z=74$) nuclei are plotted in Fig. 1.7 [10 and references therein]. The filled symbols are the experimental values. Solid lines to guide the eye connect the values for the isotopes. It is observed that the crossing frequencies for isotones increase with decrease in Z and increase with neutron number. The latter effect is simply due to the neutron shell fillings (increase in deformation). The crossing frequencies as obtained from (CSM) calculations [10] are also shown in the figure by open symbols. It is apparent from this figure that the calculated crossing frequencies are underestimated especially for the lighter nuclei. The quadrupole deformation β_2 and the neutron pairing gap Δn parameters are required to calculate the crossing frequencies in CSM. To solve this discrepancy between the theoretical and the experimental values, there is a need to critically examine the values of β_2 and Δn for the even–even nuclei considered. It was suggested in [25] that the pairing strength should include the higher order pairing, like the quadrupole pairing. Larger values of β_2 and Δn increase the crossing frequency.

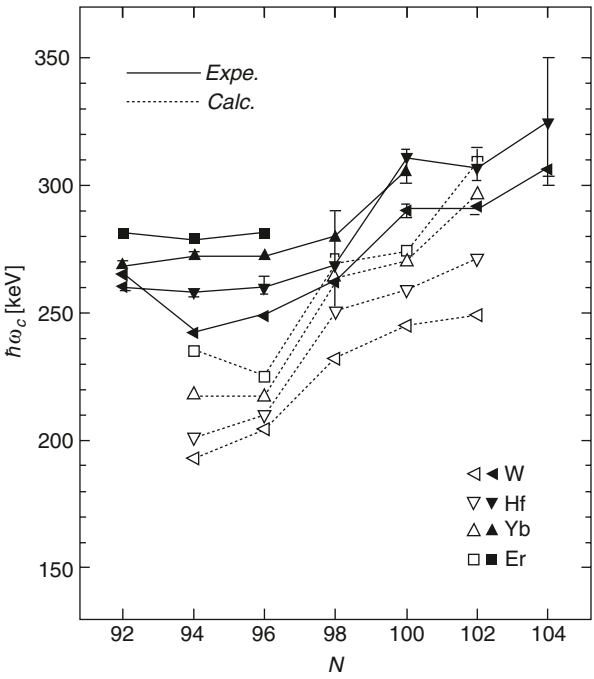

Fig. 1.7 Systematics of neutron $vi_{13/2}$ AB bandcrossing frequencies, $\hbar\omega_c$, as a function of neutron number, N, for the Yrast bands in even–even Er, Yb, Hf and W nuclei between $N=92$–104. *Closed symbols* are experimental data from [10 and references therein]. The *open symbols* are the values of bandcrossing frequencies from CSM predictions [10]. (Figure reproduced with permission from [10])

1.3.4 Evidence of Decreased Pairing Energies in Odd-N Nuclei

The quasineutron $vi_{13/2}$ AB bandcrossing frequencies, $\hbar\omega_c$, in even–even rare-earth nuclei are considered in Sect. 1.3.3 and shown in Fig. 1.7 as a function of neutron number. These, as mentioned earlier, correspond to the crossing of the positive parity ground state band (0-quasiparticle band) and the positive parity 2-quasineutron AB band. In the negative parity bands in neighbouring odd-N nuclei, the lowest energy 1-quasineutron bands are based on the E or F configuration. The AB bandcrossing which is not blocked in these bands, occurs as the crossing between the 1-quasineutron (E or F) and the 3-quasineutron (EAB or FAB) bands. The AB bandcrossings in the even–even and the neighbouring odd-N nuclei are expected to occur at the same bandcrossing frequencies. Instead, it is found that in odd-N nuclei Er, Yb, Hf and W these crossings occur systematically about 40 keV lower [26] compared to that in even–even nuclei.

Figures 1.8 and 1.9 show the plots of bandcrossing frequencies, $\hbar\omega_c$ as a function of neutron number for AB crossings in even–even and odd-N Yb [5 and references therein] and Hf [27 and references therein] isotopes respectively. The closed symbols are for positive parity bands in even–even and the open symbols for the negative parity bands in odd-N isotopes. The lines joining the data points are to guide the eye. On an average, the bandcrossing frequencies in the odd-N nuclei are reduced by ~40 keV in comparison to those in the neighbouring even–even nuclei. This re-

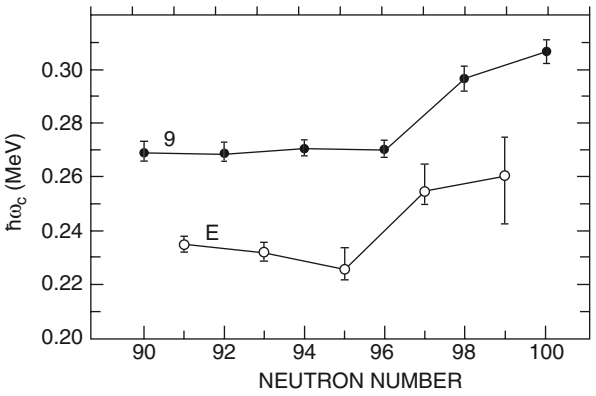

Fig. 1.8 Bandcrossing frequencies, $\hbar\omega_c$, as a function of neutron number, N, for the $vi_{13/2}$ AB bandcrossings in the positive parity bands in even–even and the negative parity bands in odd-N Yb isotopes [5 and references therein]. *Closed (open) symbols*, for the even(odd)-N isotopes. (Figure in part reproduced with permission from [5])

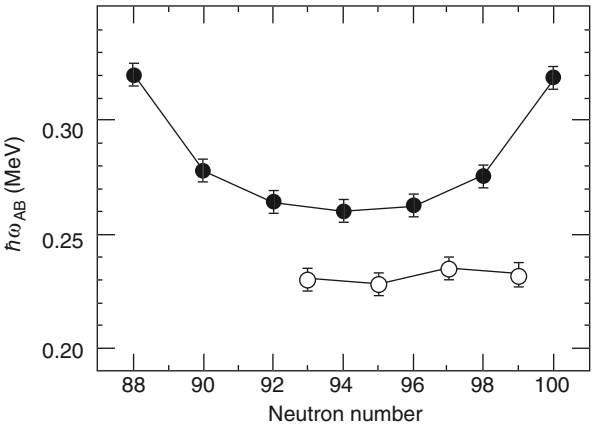

Fig. 1.9 Same as in Fig. 1.8, except that the plots are for the Hf isotopes [27 and references therein]. (Figure in part reproduced with permission from [27])

duction in the bandcrossing frequencies has been attributed [26] to reduced neutron pair correlations resulting from the blocking of the pairing contributions from the quasineutron orbit near the Fermi surface. Cranked shell model calculations [26] have shown that a decrease in the neutron pairing correlation parameter decreases the bandcrossing frequency. Investigation of bandcrossings in such nuclei, therefore, provide an insight into the pairing phenomena in nuclei.

1.3.5 Bandcrossings in A ~ 120–130 Nuclei

The investigation of lowest energy rotational alignments of pairs of high-j quasineutrons and quasiprotons and thereby of their bandcrossings are particularly interesting in the neutron-deficient nuclei in the mass region $A \sim 120$–130. The Fermi levels for both the protons and the neutrons in these nuclei lie within the $h_{11/2}$ subshell. For protons, it lies in the low-Ω prolate shape driving orbitals whereas for neutrons it is near the middle of the high-Ω oblate shape driving orbitals. As the neutron number

decreases in this mass region, the neutron Fermi level moves closer to the lower-Ω orbitals. An added advantage in this region is that the nuclei are γ-soft and so are amenable to shape changes induced by neutron and proton alignments. Therefore, nuclei in this mass region allow a detailed study of the shape-driving properties of the rotational alignment processes in the different regions of the $h_{11/2}$ high-j subshell. The properties of bandcrossings give an insight into the details of nuclear structure and information on the participating aligning high-j nucleons. The nucleon configurations for the multi-quasiparticle deformed rotational bands can also thus be determined. For nuclei closer to the lower mass region, i.e. near $A \sim 120$, since the neutron and the proton Fermi levels lie close to each other, nuclear structure may get influenced by the 'pn' interaction.

The Woods–Saxon CSM calculations [28, 29] predict that the quasiproton and quasineutron alignments in the ground state rotational bands in these nuclei will occur at nearly the same rotational frequencies. The alignment properties like the bandcrossing frequency, $\hbar\omega_c$, and the aligned angular momentum gain, Δi, can be calculated in specific cases from the CSM calculations.

Let us consider rotation alignments in even–even Ba isotopes $^{120, 122, 124, 126}$Ba. In these nuclei, the ground state band forks into two rotation aligned bands, at a particular spin ($J \sim 10\hbar$), due to the alignment of quasiprotons and the alignment of quasineutrons at nearly similar rotational frequencies. As an example, in Fig. 1.10 is shown the partial level scheme of ^{126}Ba [30] in which the forking of the ground state band occurs at $I = 10\hbar$.

Table 1.1 lists the experimental values of bandcrossing frequencies and alignment gains and the CSM predictions for the quasiproton $\pi(h_{11/2})^2$ rotational alignments in the even–even and the neighbouring odd-N Ba isotopes. In Table 1.2 are listed similar values for the quasineutron $\nu(h_{11/2})^2$ alignments in the even–even and the neighbouring odd-Z Cs isotopes.

Since the odd neutron in the neutron $\nu h_{11/2}$ favoured and the unfavoured bands are occupied, the first neutron bandcrossing in the odd-N Ba isotopes is blocked (Pauli blocking). On the basis of this argument, the first bandcrossings in these nuclei are due to the rotational alignment of a quasiproton pair $\pi(h_{11/2})^2$. On similar blocking arguments, the first alignment in the $\pi h_{11/2}$ bands in the odd-Z Cs isotopes is due to the rotational alignment of a quasineutron pair $\nu(h_{11/2})^2$.

Figure 1.11 shows a plot of the lowest rotational alignment frequencies, $\hbar\omega_c$, as a function of neutron number for the alignment of quasiproton $\pi(h_{11/2})^2$ and quasineutron $\nu(h_{11/2})^2$ pairs in even–even $^{120, 122, 124, 126}$Ba isotopes. No lowest $\nu(h_{11/2})^2$ alignment is observed in ^{122}Ba [33]. In this figure, also are plotted the lowest $\nu(h_{11/2})^2$ bandcrossing frequencies observed in the $\pi h_{11/2}$ bands in odd-Z Cs isotopes and the lowest $\pi(h_{11/2})^2$ bandcrossing frequencies in the favoured (α_f) and unfavoured (α_u) $\nu h_{11/2}$ bands in odd-N Ba isotopes. The lines connecting the data points are to guide the eye. The proton $\pi(h_{11/2})^2$ bandcrossing frequencies in the favoured (α_f) partner bands are systematically higher as compared to those in the unfavoured (α_u) partners in the $\nu h_{11/2}$ bands in odd-N Ba isotopes. This may be attributed to subtle difference in deformation between the bands. But these data points do lie close on either side of the quasiproton $\pi(h_{11/2})^2$ bandcrossing frequencies in the even–even

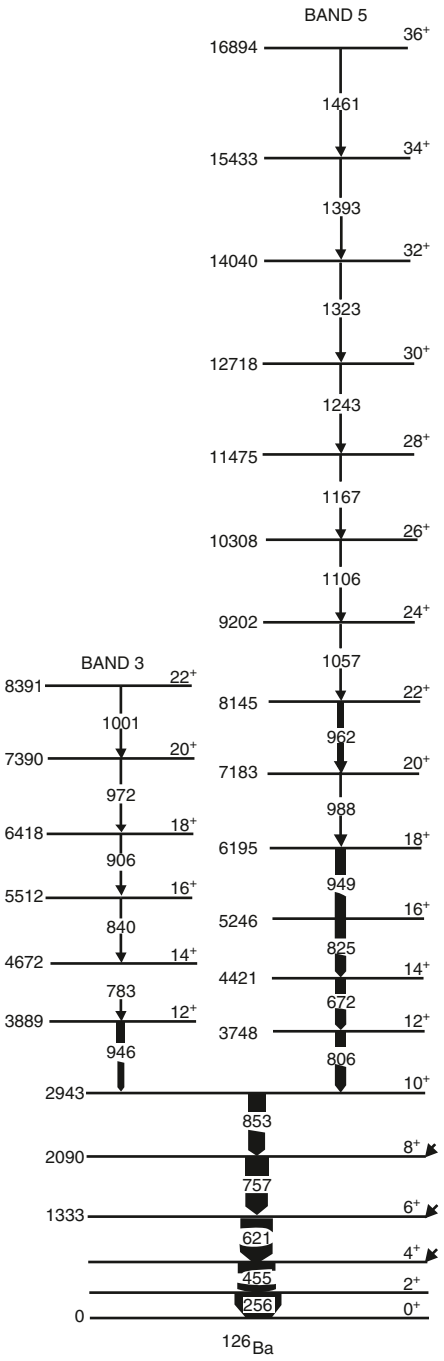

Fig. 1.10 Partial level scheme of ^{126}Ba showing the forking of the ground state band into two aligned 2-quasiparticle bands [30]. (Figure in part reproduced with permission from [30])

Table 1.1 Experimental values of bandcrossing frequencies, $\hbar\omega_c$, and gain in aligned angular momenta, Δi, for the 0 to 2-quasiproton $\pi(h_{11/2})^2$ and the 1-quasineutron $\nu h_{11/2}$ to 3-quasiparticle $\nu(h_{11/2}) \otimes \pi(h_{11/2})^2$ aligned bands in even–even and neighbouring odd-N Ba ($Z=56$) isotopes, respectively. Theoretical predictions of $\hbar\omega_c$ and Δi, from CSM calculations, wherever available, are also given for comparison

Nucleus	Experimental		Theoretical		Reference
	$\hbar\omega_c$ (MeV)	Δi ($\hbar$)	$\hbar\omega_c$ (MeV)	Δi ($\hbar$)	
$^{120}Ba_{64}$	0.38	6–7	0.41	6	[31]
$^{119}Ba_{63}$	0.41[a]	7[a]	0.36		[32]
	0.36[b]	7[b]			[32]
$^{122}Ba_{66}$	~0.36				[33]
$^{121}Ba_{65}$	0.38[a]	~7			[34]
	0.35[b]	~7			[34]
$^{124}Ba_{68}$	0.37	8.2	0.34	8.3	[35, 36]
$^{123}Ba_{67}$	~0.38[a]	~7			[37]
	~0.35[b]	~7			[37]
$^{126}Ba_{70}$	0.39	6.3	0.34	7	[30]
$^{125}Ba_{69}$	0.380[a]				[38]
	0.365[b]	~7[b]			[38]

[a] For favoured $\alpha=-1/2$ signature band
[b] For unfavoured $\alpha=+1/2$ signature band

Table 1.2 Experimental values of bandcrossing frequencies, $\hbar\omega_c$, and gain in aligned angular momenta, Δi, for the 0 to 2-quasineutron $\nu(h_{11/2})^2$ and the 1-quasiproton $\pi h_{11/2}$ to 3-quasiparticle $\pi(h_{11/2}) \otimes \nu(h_{11/2})^2$ aligned bands in even–even Ba and neighbouring odd-Z Cs isotopes, respectively. Theoretical predictions of $\hbar\omega_c$ and Δi, from CSM calculations, wherever available, are also given for comparison

Nucleus	Experimental		Theoretical		Reference
	$\hbar\omega_c$ (MeV)	Δi ($\hbar$)	$\hbar\omega_c$ (MeV)	Δi ($\hbar$)	
$^{120}Ba_{64}$	0.41	–	–	–	[31]
$^{119}Cs_{64}$					
$^{122}Ba_{66}$	–	–	–	–	–
$^{121}Cs_{66}$	~0.45[a]	~5[a]	0.40	–	[39]
$^{124}Ba_{68}$	0.41	6.2	0.40	6.7	[35, 36]
$^{123}Cs_{68}$	~0.43[a,b]	4.5[a,b]	0.40	–	[39, 40]
$^{126}Ba_{70}$	0.43	~5	0.44	5.5	[30]
$^{125}Cs_{70}$	0.44[a]	~5[a]	–	–	[38]

[a] For favoured $\alpha=-1/2$ signature band
[b] For unfavoured $\alpha=+1/2$ signature band

Ba isotopes. The neutron $\nu(h_{11/2})^2$ bandcrossing frequencies in even–even Ba isotopes are near to those in odd-Z Cs isotopes.

The blocking arguments justify that the rotational alignments in the odd-N Ba isotopes and odd-Z Cs isotopes are due to the quasiproton $\pi(h_{11/2})^2$ and quasineutron $\nu(h_{11/2})^2$ pairs respectively. The quasineutron $\nu(h_{11/2})^2$ bandcrossing frequencies in odd-Z Cs isotopes are in agreement with those in the even–even Ba isotopes for $N=68$ and 70. Also, the quasiproton $\pi(h_{11/2})^2$ bandcrossing frequencies in the odd-

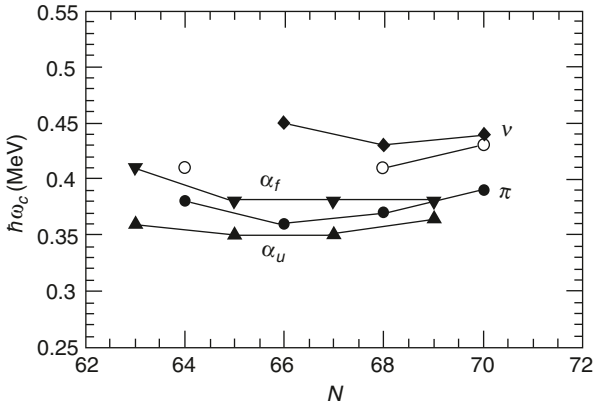

Fig. 1.11 Experimental values of bandcrossing frequencies, $\hbar\omega_c$, as a function of neutron number, N. Quasineutron $\nu(h_{11/2})^2$ bandcrossing frequencies in even–even Ba (○) and odd-Z Cs isotopes (♦). Quasiproton $\pi(h_{11/2})^2$ bandcrossing frequencies in even–even Ba (●) and favoured (α_f) (▼) and unfavoured (α_u) (▲) bands in odd-N Ba isotopes. (See Tables 1.1 and 1.2 for data)

N Ba isotopes are in agreement with those in the even–even Ba isotopes. These evidences not only establish that there are two types of bandcrossings, namely, quasiproton $\pi(h_{11/2})^2$ and quasineutron $\nu(h_{11/2})^2$ in the even–even Ba isotopes but also the proton and the neutron bandcrossings in these nuclei can be distinguished and identified. For the case of ^{126}Ba (see level scheme in Fig. 1.10), the rotational band shown on the right side, before further bandcrossing, is a 2-quasiproton $\pi(h_{11/2})^2$ aligned band and the one on the left side is a 2-quasineutron $\nu(h_{11/2})^2$ aligned band.

Excellent review articles on the topic are available in the literature [6, 9].

1.3.6 Delayed Bandcrossings in odd-Z A~160–170 Nuclei

A typical level scheme of an odd-Z nucleus ^{167}Lu [41] showing the proton $\pi h_{9/2}$ [541]1/2$^-$ band (second band from left side) is given in Fig. 1.12. The quasineutron $\nu i_{13/2}$ AB bandcrossing frequencies for the proton $\pi h_{9/2}$ [541]1/2$^-$ energy favoured rotational sequences in odd-Z Tm (Z=69), Lu (Z=71), Ta (Z=73), Re (Z=75) and Ir (Z=77) nuclei are plotted versus neutron number, N, in Fig. 1.13 [10 and references therein]. In this figure the experimental data points for ^{157}Ho (Z=67; $\hbar\omega_c$=347(+10, −13) keV [10, 42], ^{159}Ho ($\hbar\omega_c$~350 keV [43] and ^{177}Ta (Z=73; $\hbar\omega_c$~390 keV [44]) are not shown. Compared to the crossing frequencies in neighbouring even–even isotones the crossing frequencies in the $\pi h_{9/2}$ bands especially in Ho, Tm, Lu and Ta odd-Z nuclei are systematically exceptionally large (delayed by as much as ~80 keV). In this figure, one may notice that there is a dip in the crossing frequencies at N=98 where there is also a shell gap in the Nilsson diagram. The band crossing frequencies as calculated from the CSM calculations [10] are also plotted in the figure. It is seen that the discrepancy as large as ~100 keV between the experimental and the theoretical values exists. The CSM values are low. This anomaly (delay) in the experimental values of bandcrossing frequencies, has been a long-standing problem in odd-Z nuclei in this mass region. It is not fully understood

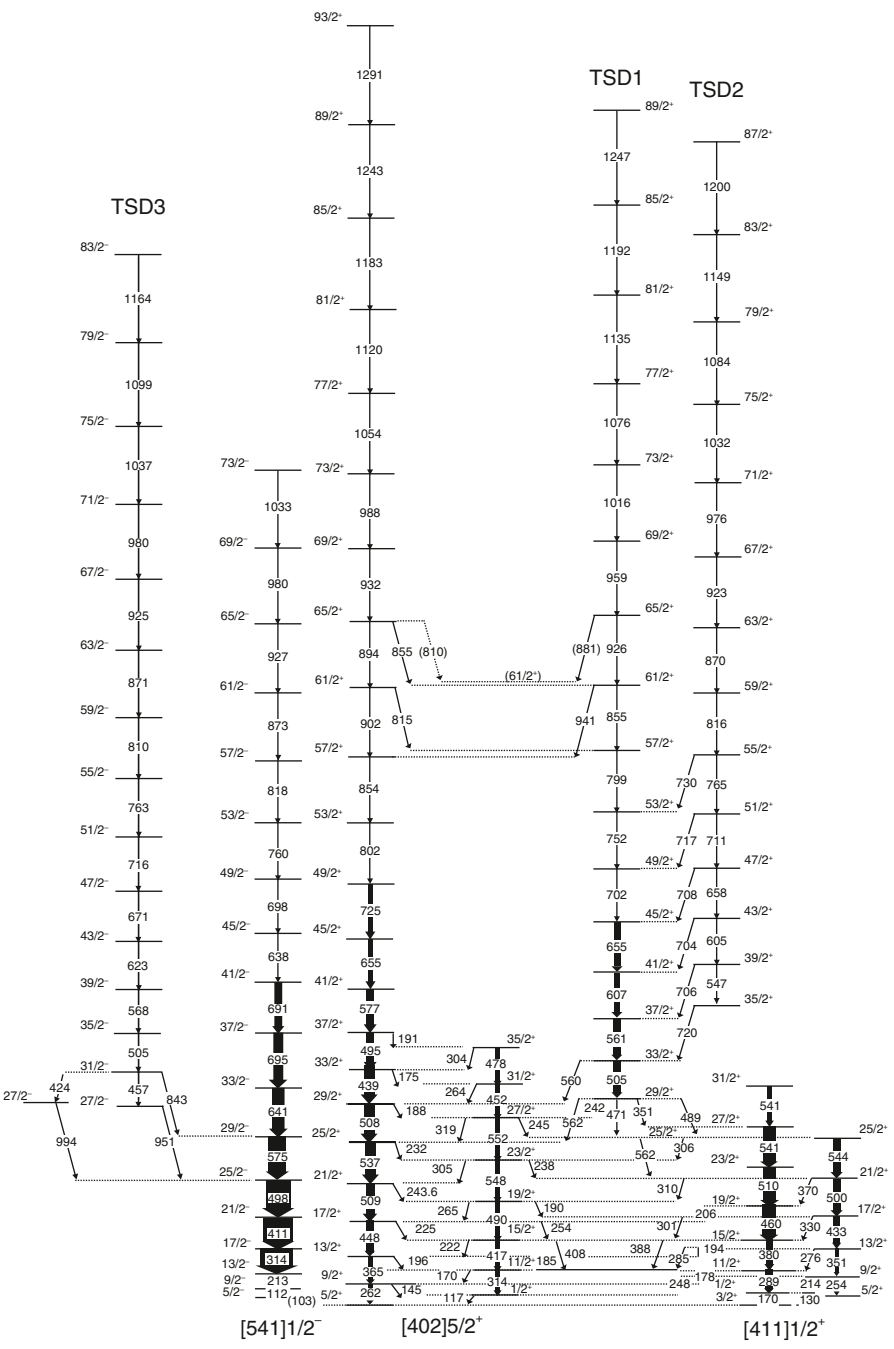

Fig. 1.12 Partial level scheme of ^{167}Lu [41] showing also the proton $\pi h_{9/2}$ [541]1/2$^-$ band (*second from left side*). (Figure reproduced with permission from [41])

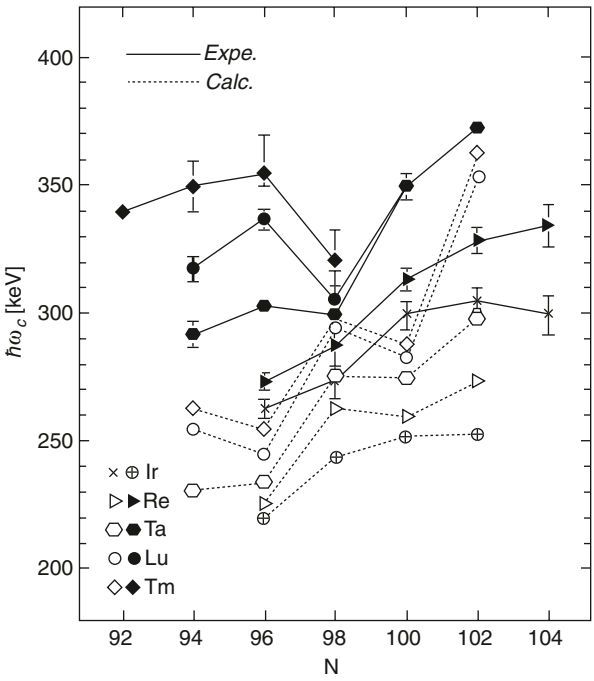

Fig. 1.13 Neutron $\nu i_{13/2}$ AB bandcrossing frequencies, $\hbar\omega_c$, as a function of neutron number, N, for the energy favoured proton $\pi h_{9/2}$ [541]1/2$^-$ bands in odd-Z Tm, Lu, Ta, Re and Ir nuclei for N=92–104. The *filled symbols* are the experimental values from [10 and references therein]. The *open symbols* are the values of bandcrossing frequencies calculated [10] using the CSM. *Solid* and *dotted lines*, to guide the eye, connect the values for the isotopes. (Figure reproduced with permission from [10])

yet. Various theoretical attempts [10, 25, 45–48] have been made to explain this anomaly. These attempts are mentioned below:

1. CSM calculations.
2. Projected shell model analysis and the effect of higher order pairing interactions as mentioned earlier (see Sect. 1.3.3.).
3. Particle-rotor model calculations with inclusion of residual proton–neutron interaction.

In the CSM analysis for calculation of bandcrossing frequencies, the two main input parameters for each nucleus, are the quadrupole deformation β_2 (actually ε_2 is used, $\varepsilon_2 = 0.95\beta_2$ for small deformations) and the neutron pairing gap, Δn, as already mentioned. (For a full set of input parameters for CSM calculations see [4].)

Instead of the values for deformation obtained from total Routhian surface calculations, one can also use the experimentally deduced values, where available. These can be obtained from lifetime measurements of the band members of the proton $\pi h_{9/2}$ bands in the above mentioned nuclei. Accurate lifetime measurements have been done for these bands in ^{157}Ho [42], ^{161}Tm [49], ^{165}Tm [10], ^{165}Lu [50], ^{169}Lu [51], ^{171}Ta [52, 53] and ^{173}Ta [54]. In Fig. 1.14 [53], the β_2 values as deduced from lifetime measurements for the one (before bandcrossing) and three (after neutron $\nu i_{13/2}$ bandcrossing) quasiparticle bands in ^{171}Ta [52, 53], as a function of rotational frequency, are shown. This indicates that the deformation before and after bandcrossing is nearly the same except at higher spins there is an indication of decrease

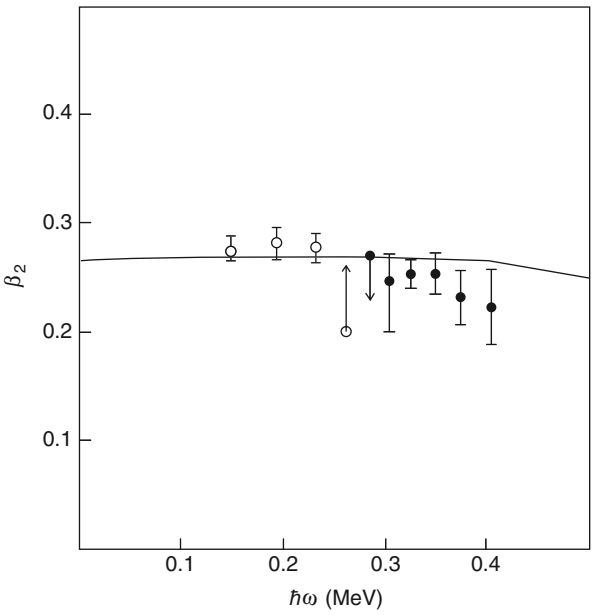

Fig. 1.14 Plot of quadrupole deformation, β_2, as a function of rotational frequency, $\hbar\omega$, for the energy favoured proton $\pi h_{9/2}$ [541]1/2$^-$ band in ^{171}Ta [52, 53]. (Figure reproduced with permission from [53])

in collectivity. Systematic theoretical total Routhian surface (TRS) calculations [10] also indicate that the alignment of the two $\nu i_{13/2}$ neutrons does not change the deformation in the band. The band maintains a constant deformation value. It is, therefore, safe to deduce an average experimental value of deformation for nuclei where lifetime measurements are available for these bands. The experimentally deduced and the theoretically calculated values of quadrupole deformations for the π [541]1/2$^-$ bands in the above mentioned odd-Z nuclei agree within 10–15%. In most of the above mentioned bands in the odd-Z nuclei, using either the experimental deformation values or those from TRS calculations, the bandcrossing frequencies obtained from CSM calculations fail to account for the observed delays in bandcrossing frequencies.

Let us now turn to the neutron pairing gap parameter, Δn. The experimental values of this parameter are determined from the four point odd–even mass difference formula [4]:

$$\Delta n = (1/4)[B(Z, N-2) - 3B(Z, N-1) + 3B(Z, N) - B(Z, N+1)]$$

where the nuclear binding energies are to be taken from the latest mass data tables [55]. In the case of protons, for the Δp parameter, a similar expression is used. The question is how to get realistic values of the parameter, Δn, for the CSM calculations. One way is to fit the experimental values of the AB neutron bandcrossing frequencies for the even–even neighbours taking the accepted values of deformation for these nuclei and deduce the average value of the pairing gap parameter, Δn which could then be used in CSM calculations for calculating the bandcrossing frequencies. For example, in ^{175}Ta [46], Δn=0.730 MeV as extracted from odd–even

mass difference formula and that obtained by fitting the bandcrossing frequencies in even–even neighbours is $\Delta n = 0.916$ MeV. Using the latter value of Δn, the CSM calculations even then give too low a value, $\hbar\omega_c = 293$ keV which is ~80 keV below the experimental value of $\hbar\omega_c = 375$ keV [46]. To reproduce the experimental value one has to use a large value of deformation $\varepsilon_2 \sim 0.30$ [46]. As was pointed out in [56], increase in deformation decreases the pairing gap parameter. Smaller values of Δn are expected to decrease the bandcrossing frequency. Various authors, e.g. [10, 50] have come to the conclusion that the abnormal shift in the bandcrossing frequencies can only be partially explained by the enhanced deformation. The remaining discrepancy, therefore, cannot be explained in terms of the CSM.

The results of the *Projected shell model calculations* [25, 46] are given as plots of rotational frequency as a function of angular momentum rather than bandcrossing frequency, for different values of quadrupole pairing strengths. These calculations have been able to reproduce agreement with experiment for the proton $\pi h_{9/2}$ band in ^{175}Ta.

Particle-rotor model calculations [48] with an empirical approach for the residual interaction between the $\pi h_{9/2}$ protons and $\nu i_{13/2}$ neutrons have succeeded to a good extend in predicting the additional delayed bandcrossing frequencies. However, a *3-quasiparticle-rotor model* which includes the residual np interactions may be another possible approach to understand the bandcrossing frequency anomaly [48].

1.4 Comments and Conclusions

The rotational alignment of nucleons along the rotational axis and consequent bandcrossings in nuclei has a historical importance in that this discovery in effect led to the whole growth in high spin nuclear structure physics. In this chapter, a first order description of bandcrossings has been given. This topic is vast spanning a large number of nuclei in different mass regions where rotational alignments and bandcrossings have been found. The observed bandcrossings involve different types of quasineutron and quasiproton pairs, like, AB, BC, etc., for neutrons and ApBp, BpCp, etc., for protons. The reason for keen interest in investigation of bandcrossings is multifold. The most general use is for the assignment of configurations to rotational bands in nuclei. Useful information is also obtained about the strength of pairing correlations and the 'np' interactions.

In the very high spin regime, $I \sim 40$–$50\hbar$, unpaired bandcrossings between bands of different configurations have been found in Er nuclei [57].

It is very difficult to cover the various types of bandcrossings observed experimentally in nuclei in different mass regions. As an illustration, discussion on the systematics of neutron $\nu i_{13/2}$ AB bandcrossings in even–even rare-earth nuclei, evidence of decreased pairing energies in odd-N $A \sim 160$ nuclei, evidence of proton $\pi(h_{11/2})^2$ and neutron $\nu(h_{11/2})^2$ bandcrossings in ground state band forking in even–even Ba isotopes in $A \sim 120$–130 region and delayed bandcrossings in the $[541]1/2^-$ bands in odd-Z $A \sim 160$–170 nuclei have been discussed here.

It is well known that there are discrepancies between the experimentally determined band crossing frequencies and the predictions of the CSM calculations. It will be useful to pursue the investigation of bandcrossing phenomena under other theoretical approaches like, e.g. the projected shell model and the particle-rotor model.

References

1. A. Johnson et al., Phys. Lett. 34B, 605 (1971).
2. F. S. Stephens and R. S. Simon, Nucl. Phys. A 183, 257 (1972).
3. I. Y. Lee et al., Phys. Rev. Lett. 38, 1454 (1977).
4. R. Bengtsson et al., At. Data Nucl. Data Tables, 35, 15 (1986).
5. S. Jónsson et al., Nucl. Phys. A 449, 537 (1986).
6. R. Wyss et al., Nucl. Phys. A 505, 337 (1989).
7. R. Wyss et al., in Proc. International Conference on high spin physics and gamma-soft nuclei, eds. J. X. Saladin, R. A. Sorensen and C. M. Vincent, (World Scientific, 1991) p. 123.
8. L. L. Riedinger et al., Prog. Part. Nucl. Phys., 28, 75 (1992).
9. A. Granderath et al., Nucl. Phys. A 597, 427 (1996).
10. H. J. Jensen et al., Nucl. Phys. A 695, 3 (2001).
11. Niel Rowley et al., Phys. Rev. C 80, 024323 (2009).
12. K. Hara and Y. Sun, Nucl. Phys. A 529, 445 (1991).
13. Data from Evaluated Nuclear Structure Data File (ENSDF) at http://www.nndc.bnl.gov/ensdf/. See references therein.
14. J. Simpson et al., J. Phys. (London) G 10, 383 (1984).
15. R. Holzmann et al., Phys. Rev. C 31, 421 (1985).
16. J. Simpson et al., Phys. Rev. Lett. 54, 1132 (1985).
17. M. A. Riley et al., Phys. Lett. 135B, 275 (1984).
18. R. Holzmann et al., Phys. Rev. Lett. 50, 1834 (1983).
19. L. L. Riedinger et al., Nucl. Phys. A 347, 141 (1980).
20. A. Faessler and M. Ploszajczak, Phys. Lett. 76 B, 1 (1978).
21. A. Ansari and S. C. K. Nair, Phys. Rev. Lett. 41, 1768 (1978).
22. J. J. Routh, in The advanced part of a treatise on the dynamics of a system of rigid bodies, 6th ed. (Macmillian, London, 1905).
23. L. L. Riedinger et al., Phys. Rev. Lett. 44, 568 (1980).
24. M. A. Riley et al., Phys. Rev. C 39, 291 (1989).
25. Yang Sun et al., Phys. Rev. Lett. 72, 3483 (1994).
26. J. D. Garrett et al., Phys. Rev. Lett. 47, 75 (1981).
27. M. Murzel et al., Nucl. Phys. A 516, 189 (1990).
28. W. Nazarewicz et al., Nucl. Phys. A 435, 397 (1985).
29. S. Cwiok et al., Comput. Phys. Commu. 46, 379 (1987).
30. D. Ward et al., Nucl. Phys. A 529, 315 (1991).
31. J. F. Smith et al., Phys. Lett. B 483, 7 (2000).
32. J. F. Smith et al., Phys. Rev. C 61, 044329 (2000).
33. C. M. Petrache et al., Eur. Phys. J. A 12, 135 (2001).
34. B. Cederwall et al., Nucl. Phys. A 529, 410 (1991).
35. S. Pilotte et al., Nucl. Phys. A 514, 545 (1990).
36. A. Al – Khatib et al., Phys. Rev C 74, 014305 (2006).
37. R. Wyss et al., Z. Phys. A 330, 123 (1988).
38. J. P. Martin et al., Nucl. Phys. A 489, 169 (1988).
39. F. Liden et al., Nucl. Phys. A 550, 365 (1992).

40. Kuljeet Singh et al., Eur. Phys. J. A 25, 345 (2005).
41. H. Amro et al., Phys. Rev. C 71, 011302 (2005).
42. J. Gascon et al., Nucl. Phys. A 513, 344 (1990).
43. Ma Ying-Jun et al., J. Phys. G: Nucl. Part. Phys. 26, 43 (2000).
44. D. E. Archer et al., Phys. Rev. C 52, 1326 (1995).
45. C. S. Wu, Phys. Rev. C 51, 1819 (1995).
46. Shu-Xian Wen et al., Phys. Rev. C 54, 1015 (1996).
47. W. Satula et al., Nucl. Phys. A 565, 573 (1993).
48. R. A. Bark et al., Nucl. Phys. A 630, 603 (1998).
49. S. J. Warburton et al., Nucl. Phys. A 591, 323 (1995).
50. K. Andgren et al., Phys. Rev. C 71, 014312 (2005).
51. S. Ogaza et al., Nucl. Phys. A 559, 100 (1993).
52. P. Joshi et al., Phys. Rev. C 60, 034311 (1999).
53. L. H. Zhu et al., Eur. Phys. J. A 27, 137 (2006).
54. P. Joshi et al., Phys. Rev. C 64, 034303 (2001).
55. G. Audi et al., Nucl. Phys. A 729, 337 (2003).
56. H. J. Jensen et al., Z. Phys. A 340, 351 (1991).
57. J. Simpson et al., Phys. Rev. C 62, 024321 (2000).

Chapter 2
Magnetic Rotation

2.1 Introduction

Sequences of rotational-like bands with strong M1 transitions ($\Delta I = 1$ bands) were observed in nearly spherical nuclei in the neutron-deficient Pb isotopes in the early 1990s [1–7]. These sequences were later interpreted [8] as occurring due to a new nuclear excitation mode—*Magnetic Rotation*. A $\Delta I = 1$ rotational band was already reported in the literature in the year 1986 in ^{83}Kr [9] which was later found to possess all the experimental features to qualify as a magnetic rotational band [10].

These $\Delta I = 1$ bands have a number of interesting properties. One of the most interesting aspects of these bands is the rotational-like behaviour which was till then a concept associated only with normally deformed and super-deformed nuclei. One of the first examples of such $\Delta I = 1$ bands in the Pb isotopes was found in ^{199}Pb nucleus [1, 3]. Figure 2.1 shows the gamma-ray spectrum of a $\Delta I = 1$ magnetic rotational band in ^{199}Pb [11]. The striking regularity in energy spacing between the consecutive gamma-rays is surprising. These gamma-ray transitions were later found to be of M1 character [12, 13]. In Fig. 2.2 is shown the gamma-ray spectrum of a super-deformed band in ^{196}Pb [11]. The spectrum in Fig. 2.1 is amazingly similar in the regularity of energy spacing to that in Fig. 2.2. But in the latter figure the connecting gamma-ray transitions are of E2 character. In both the $\Delta I = 1$ band and the super-deformed band, the observed energy levels follow the relation $(E-E_0) \propto I(I+1)$, where E is the excitation energy of a state, E_0 is the energy of the lowest energy state ($E_0 = 0$ for the ground state of a normally deformed band in an even–even nucleus) and I is the spin of the excited state. The above relationship holds when the nucleus does not change its structure. In normally deformed nuclei, for example in the mass $A \sim 160$ region, M1 gamma-ray transitions are observed between the signature partners of a deformed band. These M1 transitions are in competition with strong E2 intra-band transitions, indicating substantial quadrupole deformation of the nucleus. In the $\Delta I = 1$ bands, as in ^{199}Pb, the strong M1 transitions are associated with weak or very weak cross-over E2 transitions. This indicates small deformation of the nucleus depicting the $\Delta I = 1$ bands.

A large number of $\Delta I = 1$ magnetic rotational bands have been observed in different mass regions [14] in nuclei near magic numbers where the nuclei are weakly deformed. In the sections to follow, a review of the available experimental informa-

S. C. Pancholi, *Exotic Nuclear Excitations,* Springer Tracts in Modern Physics 242,
DOI 10.1007/978-1-4419-8038-0_2, © Springer Science+Business Media, LLC 2011

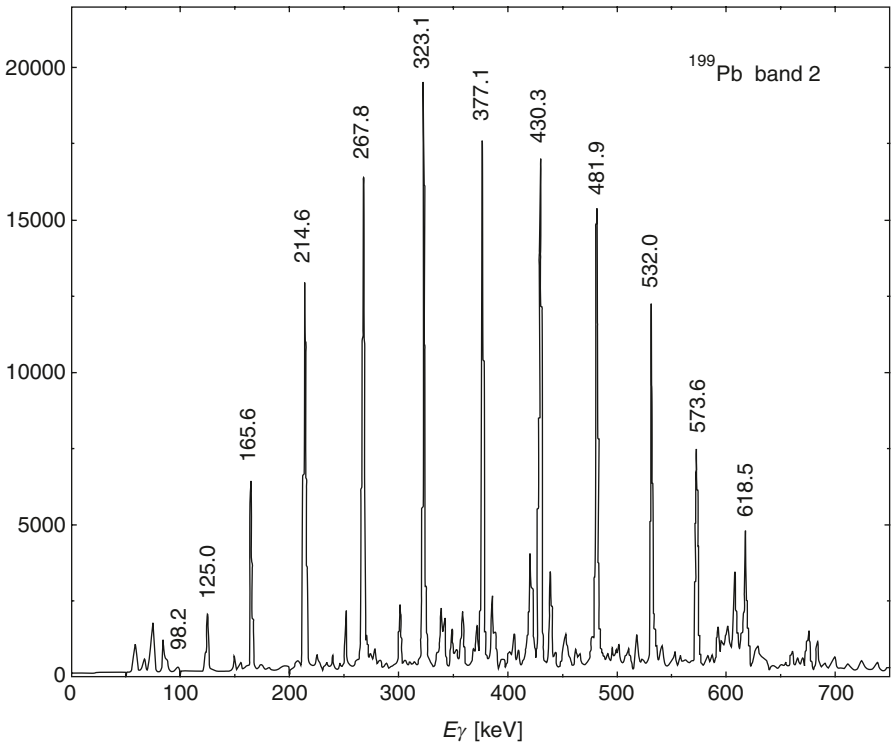

Fig. 2.1 Gamma-ray spectrum of a magnetic rotational band in ^{199}Pb. The gamma-ray peak energies are marked in keV. (Figure reproduced with permission from [11])

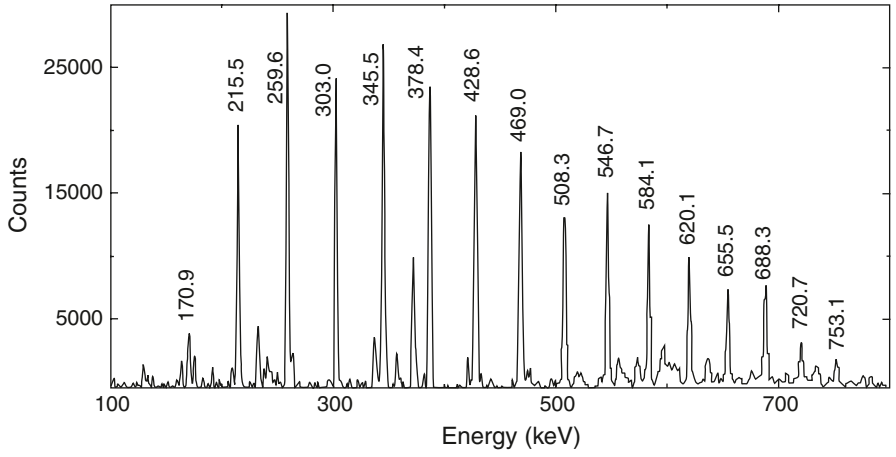

Fig. 2.2 Gamma-ray spectrum of a super-deformed band in ^{196}Pb. The gamma-ray energies of the peaks are marked in keV. (Figure reproduced with permission from [11])

tion on the properties of magnetic rotational bands in Pb region will be given. A brief mention about such bands observed in the lighter mass regions will be made. This will be followed by theoretical interpretation of these $\Delta I = 1$ bands.

Excellent review articles on magnetic rotational bands are available in the literature [11, 15].

2.2 Magnetic Rotational Bands in the Pb Region

2.2.1 General Nuclear Structure in Light Pb Nuclei

For a discussion of the properties of magnetic rotational bands in the neutron-deficient Pb region $A \sim 190$–200, it is helpful to first know the general nuclear structure in these single closed shell $Z = 82$ nuclei. For $N \leq 125$ odd-A Pb nuclei, the low-lying spherical states are the $p_{1/2}$, $f_{5/2}$ and $p_{3/2}$ single neutron hole states. In addition to these, the $3/2^-$, $5/2^-$, $7/2^-$ and $9/2^-$ states may be described as weak-coupling multiplets—$f_{5/2}$, $p_{3/2}$, $p_{1/2}$ neutron hole states coupled to the 2^+ state of an even–even core.

The $J^\pi = 13/2^+$ states in these odd-mass nuclei are the $(\nu i_{13/2})^{-1}$ one-quasi-neutron hole states. The $33/2^+$ states are the $(\nu i_{13/2})^{-3}$ three-quasi-neutron hole states, whereas in the even–even Pb nuclei, the 12^+ and the 20^+ states are $(\nu i_{13/2})^{-2}$ two-quasi-neutron and the $(\nu i_{13/2})^{-4}$ four-quasi-neutron hole states, respectively.

In many closed shell and near closed shell nuclei in the $Z = 82$ Pb region, intruder states have been observed. Low-lying 0^+ states have been found in $^{190-198}$Pb isotopes [16, 17]. In addition, 8^+ and 11^- isomeric states have been found in many of the even isotopes of Pb (e.g. see [18]). These have been interpreted as proton 2p–2h (two particle–two hole) excitations across the $Z = 82$ shell gap; that is two $3s_{1/2}$ protons have been excited to the $h_{9/2}$ orbital (8^+ state) or one proton to $h_{9/2}$ and the other to $i_{13/2}$ orbital (11^- state) leaving two proton holes in the $s_{1/2}$ orbital. An interesting feature of the Pb nuclei is that these 2p–2h excited states which coexist with the other spherical $\nu i_{13/2}$ neutron hole states show different shapes. Enhanced E3 transitions from the 11^- states were reported in $^{190-196}$Pb [19, 20] and were interpreted as evidence that these states are of oblate deformed shape. Spectroscopic quadrupole moments were measured for the 11^- states in $^{192-196}$Pb [21, 22]. Assuming oblate deformation, the average quadrupole deformation was obtained to be $\beta_2 = -0.146(14)$ for these states. The basic nucleon configurations assigned [23–25] to these proton intruder states are as follows:

J^π	Configuration	Nilsson configuration
8^+	$\pi\left[h_{9/2}{}^2\right]_{8^+}$	$\left[\{\pi h_{9/2}\,[505]\,9/2^-\} \otimes \{\pi h_{9/2}\,[514]\,7/2^-\}\right]_{K^\pi = 8^+}$
11^-	$\pi\left[h_{9/2} i_{13/2}\right]_{11^-}$	$\left[\{\pi h_{9/2}\,[505]\,9/2^-\} \otimes \{\pi i_{13/2}\,[606]\,13/2^+\}\right]_{K^\pi = 11^-}$

It may be mentioned that no rotational bands are built on these intruder states.

So far, the independent coexistence of spherical states and the weakly collective oblate 2p–2h states in the light Pb isotopes has been described here. In the next section, properties of the $\Delta I = 1$ magnetic rotational bands built on the 2p–2h proton states coupled with the $(\nu i_{13/2})^{-n}$ ($n = 1, 2, 3,\ldots$) neutron hole states will be discussed.

2.2.2 The Magnetic Rotational Bands—Experimental Results

Soon after the discovery of a $\Delta I = 1$ band in ^{199}Pb [1, 3], intense experimental investigations of these bands were undertaken by several groups [11 and references therein] and, as a result, a large number of these bands were found in the odd and even light Pb isotopes and in several other medium and light mass near spherical nuclei [14]. In this section, spectroscopic observations of such $\Delta I = 1$ bands and their properties in the odd Pb isotopes $^{193, 195, 197, 199}$Pb and the even Pb isotopes $^{194, 196, 198}$Pb will be described and discussed. In Figs. 2.3, 2.4, 2.5, 2.6, 2.7 and 2.8 the level schemes of ^{197}Pb [26], ^{199}Pb [11 and references therein], ^{194}Pb [27], ^{196}Pb [28] and ^{198}Pb [26] are shown. These level schemes were investigated using high detection efficiency gamma detector arrays GAMMASPHERE and different versions of the EUROGAM and EUROBALL. The identified $\Delta I = 1$ bands are marked by band numbers in the figures. In addition to the measurement of gamma-ray energies of the $\Delta I = 1$ transitions in the bands and of the cross-over $\Delta I = 2$ transitions wherever these could be detected along with their relative gamma-ray intensities, a number of different measurements, such as the *g*-factor and quadrupole moment of the bandhead states and of the component neutron and proton states, internal conversion coefficients and linear polarisation of gamma-ray transitions and angular correlation ratios R_{DCO}, were done in separate experiments. Another important class of measurements was that of accurate lifetimes of the excited states of the $\Delta I = 1$ bands.

Let us now talk about the properties of these $\Delta I = 1$ bands as deduced from the above-mentioned experiments.

2.2.2.1 Multipolarity and Character of the Inter-connecting Transitions

For the determination of multipole order of the gamma-ray transitions, angular distribution coefficients and directional correlations from oriented states (DCO ratios—R_{DCO}) have been measured in a number of $\Delta I = 1$ bands in the Pb isotopes [23, 26–30]. Such measurements take advantage of the fact that in heavy-ion fusion reactions, anisotropy of the gamma-ray angular distributions is induced as a result of preferential population of some of the magnetic sub-states of excited nuclear state, causing nuclear alignment. Let us take the case of band 1 in ^{197}Pb (see Fig. 2.3) which gives a good representation of the properties of $\Delta I = 1$ bands in Pb region. This band in this nucleus will often be referred as a 'case study'. In Fig. 2.9 a plot of R_{DCO} ratios versus gamma-ray transition energy for the band [26] is shown. The

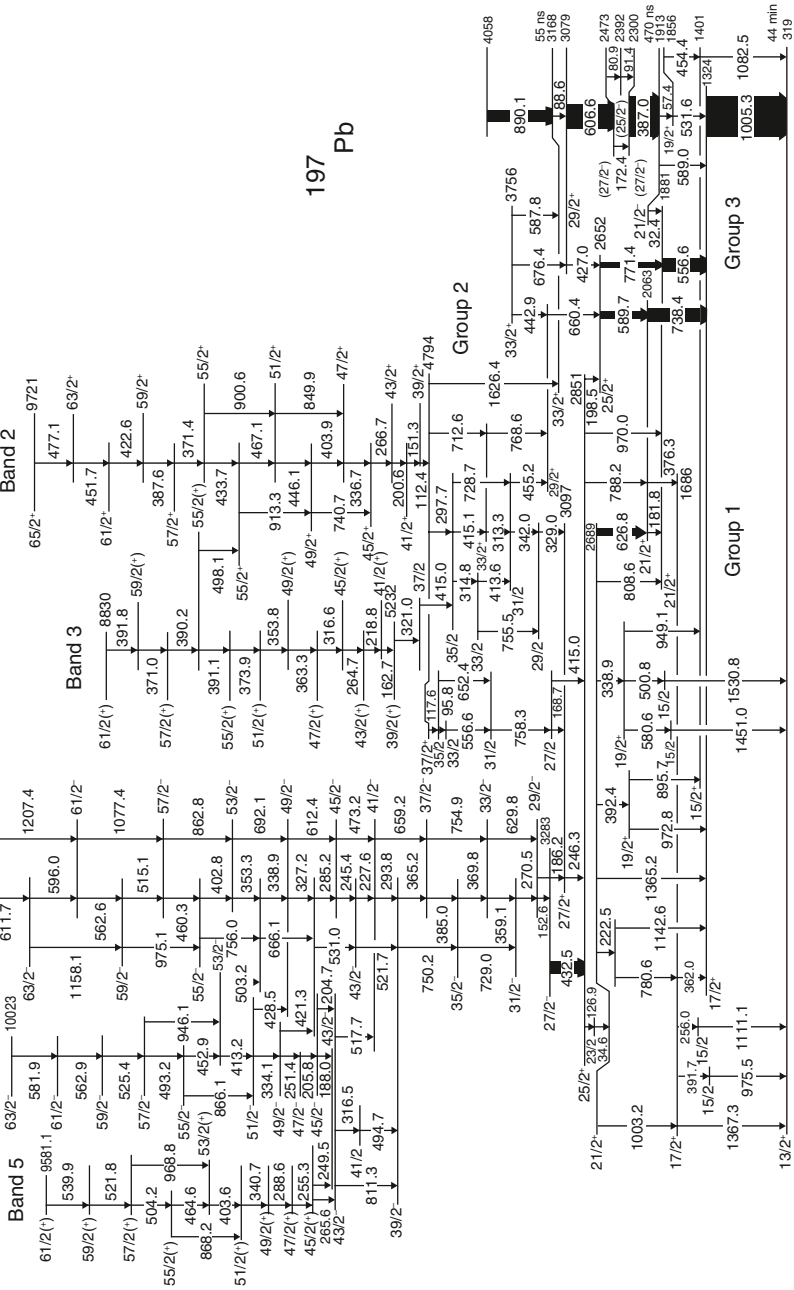

Fig. 2.3 Level scheme of ^{197}Pb [26]. (Figure reproduced with permission from [26])

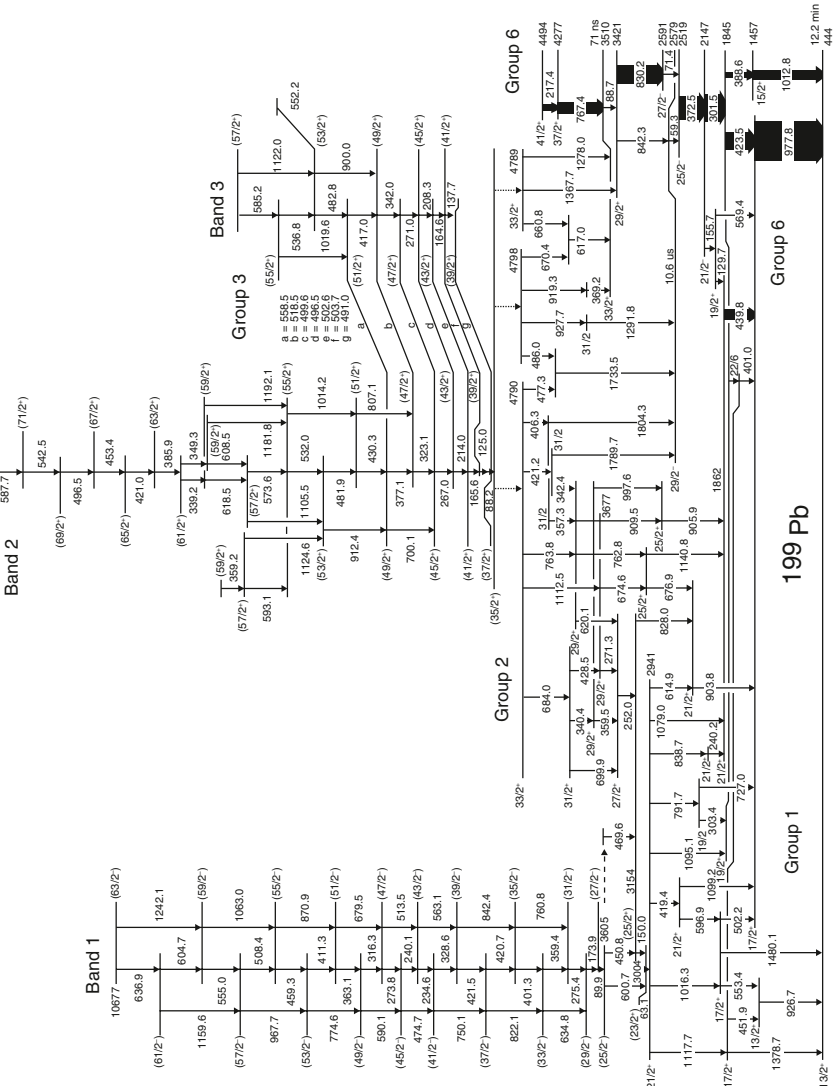

Fig. 2.4 Partial level scheme of ^{199}Pb [11 and references therein]. (Figure reproduced with permission from [11])

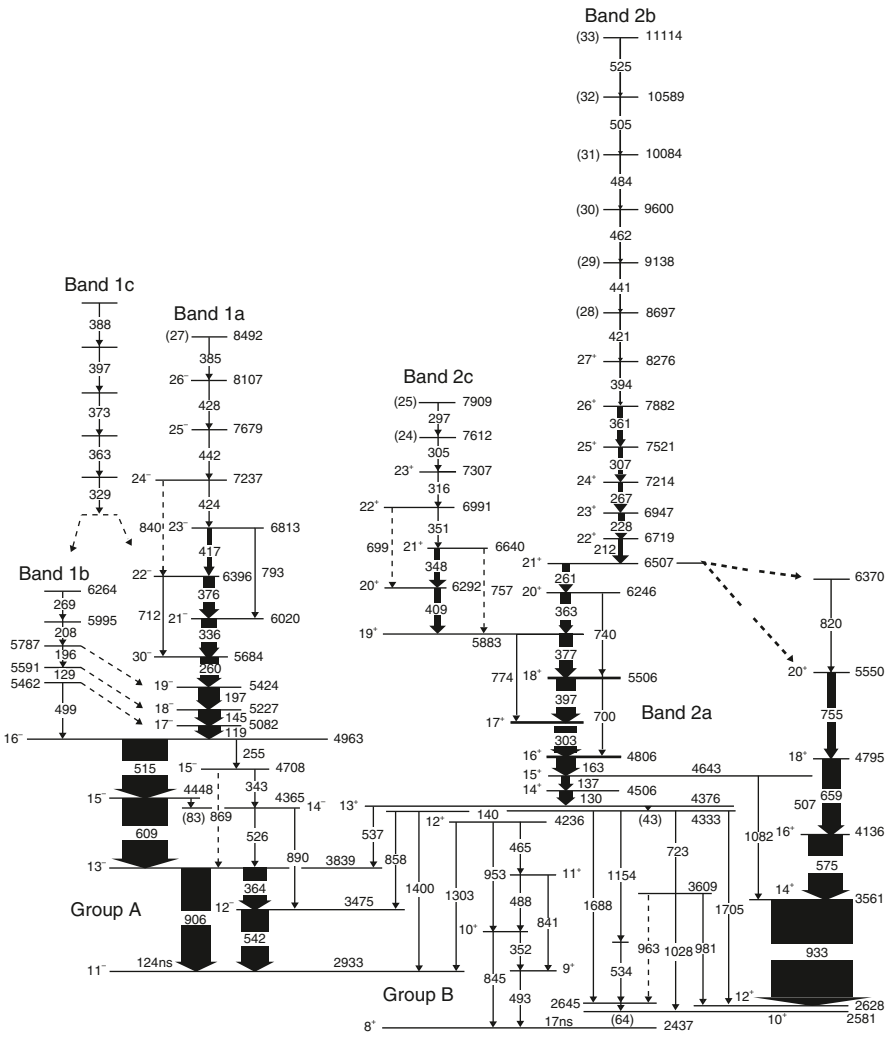

Fig. 2.5 Partial level scheme of ^{194}Pb [27]. (Figure reproduced with permission from [27])

low-energy in-band gamma-ray transitions are dipoles as the R_{DCO} values for these lie around a value $R_{DCO} = 0.6$ for pure stretched dipole transitions for the EUROGAM 2 array geometry. The high-energy cross-over transitions, for example 729.0, 750.2, 754.9 and 975.1 keV, are quadrupoles with the R_{DCO} values which scatter around $R_{DCO} = 1$ for pure stretched quadrupole transitions.

Relative parities of excited nuclear levels can be determined by the measurement of linear polarisation of gamma-ray transitions between states as these measurements depend upon the electric or magnetic character of the transition and supplement the multipole order information obtained from the R_{DCO} ratio measurement.

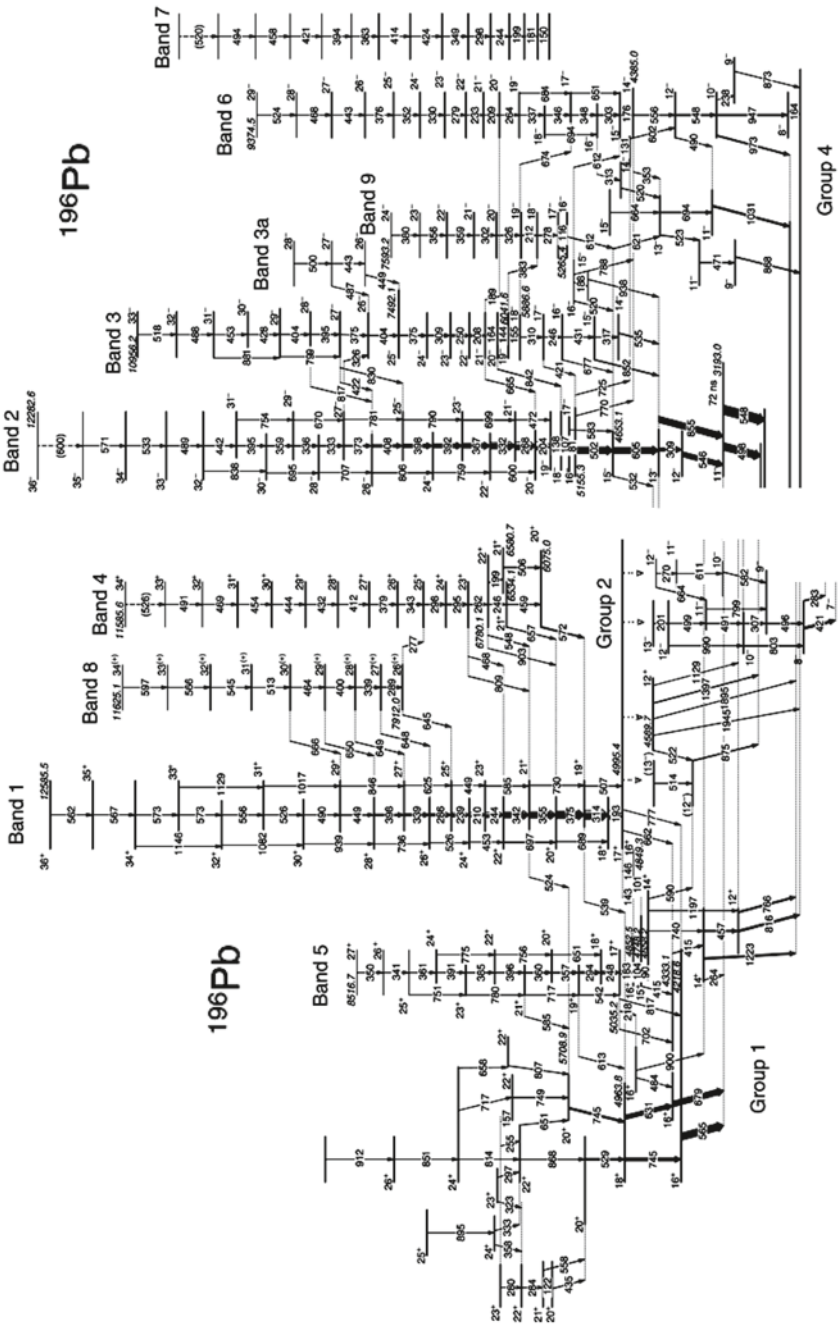

Fig. 2.6 Level scheme of ^{196}Pb [28]. (Figure reproduced with permission from [11])

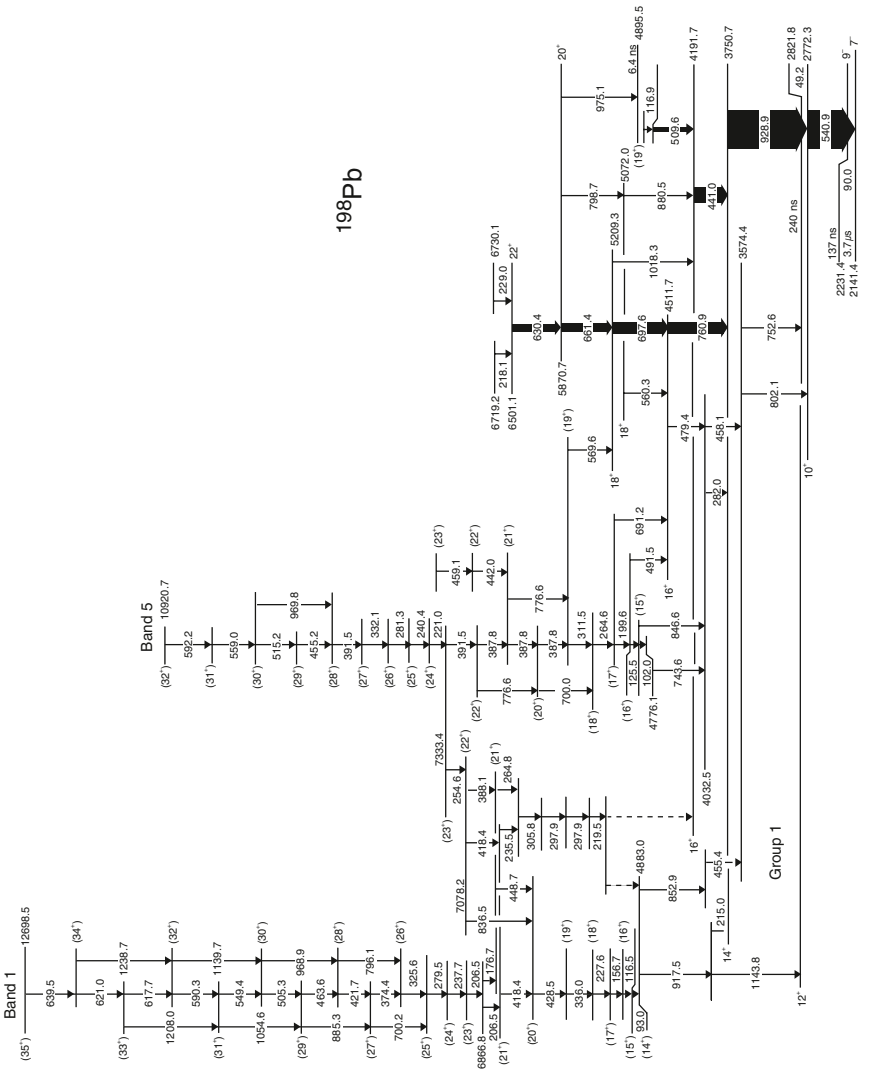

Fig. 2.7 Partial level scheme (Part 1) of ^{198}Pb [26]. (Figure reproduced with permission from [26])

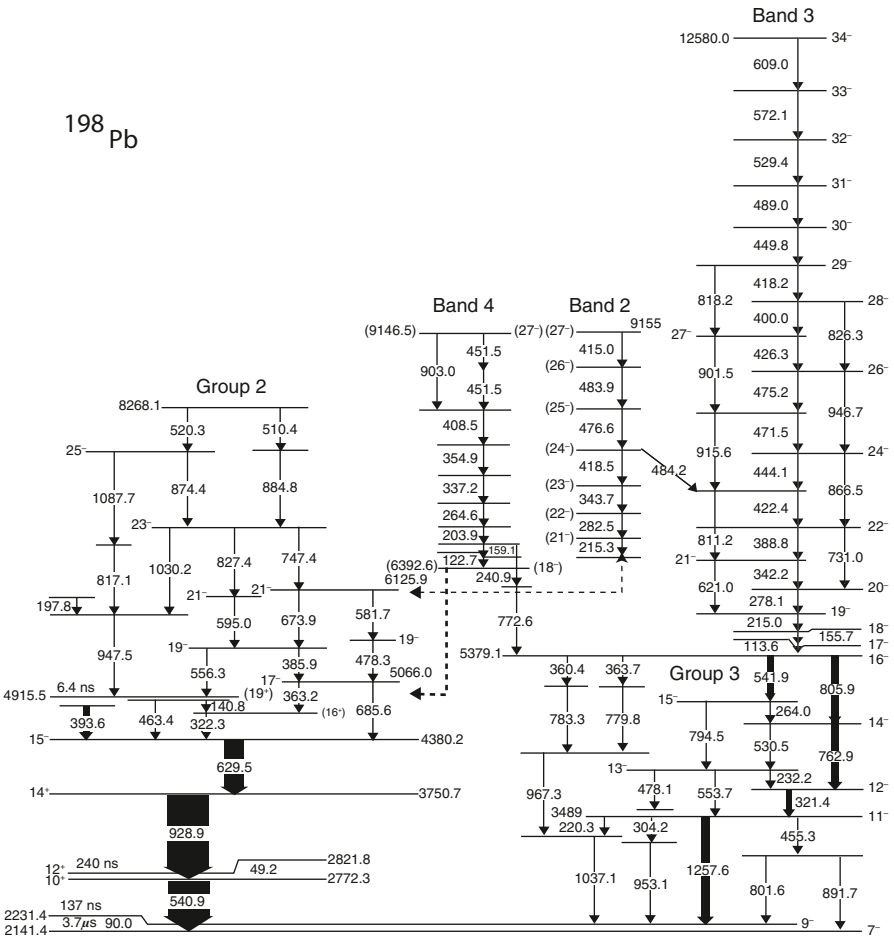

Fig. 2.8 Partial level scheme (Part 2) of ^{198}Pb [26]. (Figure reproduced with permission from [26])

Linear polarisation measurements have been done for the in-band low-energy gamma-ray transitions in the $\Delta I = 1$ bands in ^{196}Pb [28] and ^{197}Pb [26] by using the Clover detectors of the EUROGAM 2 and EUROBALL–IV spectrometers. General description of the details of linear polarisation measurement of gamma-ray transitions using Compton polarimeters, like a Clover detector or three Ge-detectors, can be found in [26, 31 and references therein]. The nuclear alignment in heavy-ion reactions, which induces the anisotropy of angular distribution, also manifests linear polarisation of gamma-rays. In linear polarisation measurements, advantage is taken of the fact that Compton scattering depends upon the polarisation of gamma-rays. The linear polarisation effect is largest near 90° to the beam direction where the Clover detectors are placed. In a Clover detector, the Ge crystal which is hit by an emitted gamma-ray acts as a scatterer and the two adjacent Ge crystals act as absorbers. A reference plane for each gamma-ray is defined by the beam direction

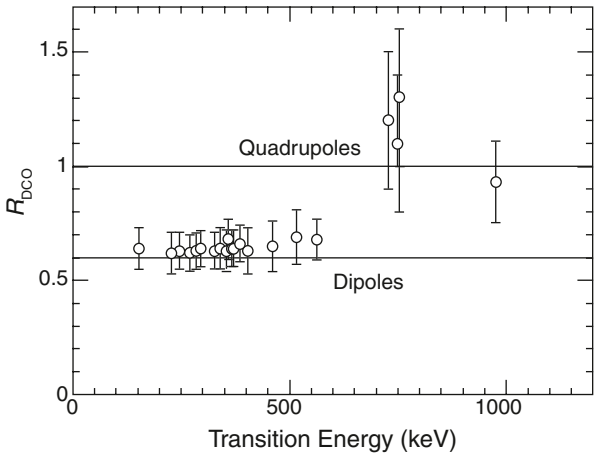

Fig. 2.9 R_{DCO} values as a function of gamma-ray transition energy for band 1 in ^{197}Pb. (Data taken from [26])

and the direction of emission of the gamma-ray. Intensity (I_h) of the full energy gamma-ray peak formed by Compton-scattered gamma-rays parallel (or horizontally) to the reference plane in one adjacent absorber Ge crystal in coincidence with the partial energy events in the scatterer and (I_v) of the peak in similar Compton scattering coincidences vertically to the plane are analysed separately. Such a polarimeter can be used to determine the electric or magnetic character of a gamma-ray as magnetic transitions favour parallel (horizontal) Compton scattering whereas the electric transitions favour perpendicular (vertical) Compton scattering [32]. The asymmetry ratio

$$A(E\gamma) = \frac{[I_v(E\gamma) - I_h(E\gamma)]}{[I_v(E\gamma) + I_h(E\gamma)]}$$

defined in [33] is measured [26]. The polarisation asymmetry ratio $A(E\gamma)$ is negative for unmixed stretched magnetic transitions and positive for electric transitions. In order to deduce the linear polarisation, $P = A(E\gamma)/Q(E\gamma)$, where $Q(E\gamma)$ is the polarisation sensitivity of the Compton polarimeter which in the experiment on ^{197}Pb for the Clover detectors is $Q \approx 0.2$–0.25 in the gamma-ray energy range 300 to 700 keV [26 and references therein]. In Fig. 2.10 is shown the difference gamma-ray spectrum of the linear polarisation spectra, vertical and horizontal, of the same band 1 in ^{197}Pb (see Fig. 2.3). Gamma-ray transitions with magnetic character result in negative gamma-ray peaks whereas electric transitions give positive peaks [26]. The low-energy transitions are the in-band magnetic transitions and the high-energy cross-over transitions 750.2 and 754.9 keV (marked as 'x' in the figure) are of electric character. The other positive peaks of energies 556.6, 626.8 and 738.4 keV in the figure are some E2 transitions in the low-energy part of the level scheme. The 432.5 keV positive peak is an E1 transition which depopulates band 1.

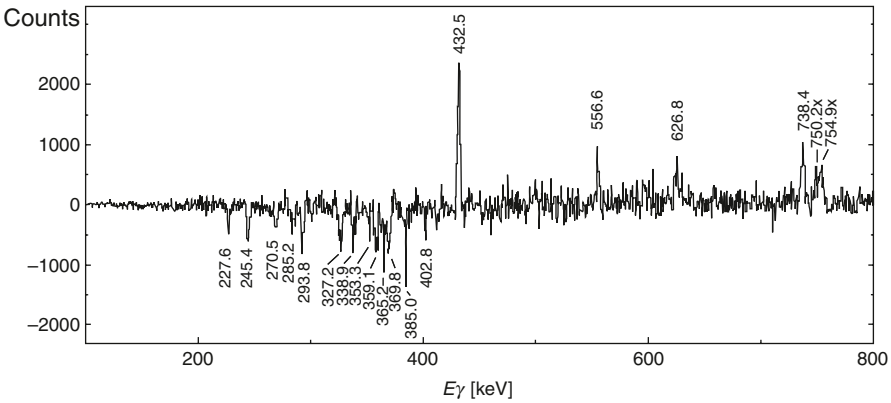

Fig. 2.10 Difference gamma-ray linear polarisation spectra for parallel and perpendicular Compton scattering of transitions in band 1 in ^{197}Pb. Transitions with magnetic character result in negative peaks whereas the electric transitions result in positive peaks [26]. (Figure reproduced with permission from [26])

Multipole order and the electric or magnetic character of gamma-ray transitions can also be determined by the measurement of *internal conversion coefficients* of the transitions and their comparison with the theoretical values for pure transitions. Such measurements have been done for the $\Delta I = 1$ bands in ^{197}Pb and ^{199}Pb [12, 13]. Let us again consider band 1 in ^{197}Pb (Fig. 2.3). Figure 2.11 shows the experimental values of the K-shell internal conversion coefficients, α_K, for the low- energy in-band gamma-ray transitions in this band versus transition energy. The solid lines in the figure are the theoretical values [34] of α_K for the pure M1, E2 and E1 transitions in the energy range ~100 to 400 keV. From this figure, it is clear that these in-band transitions are M1 transitions.

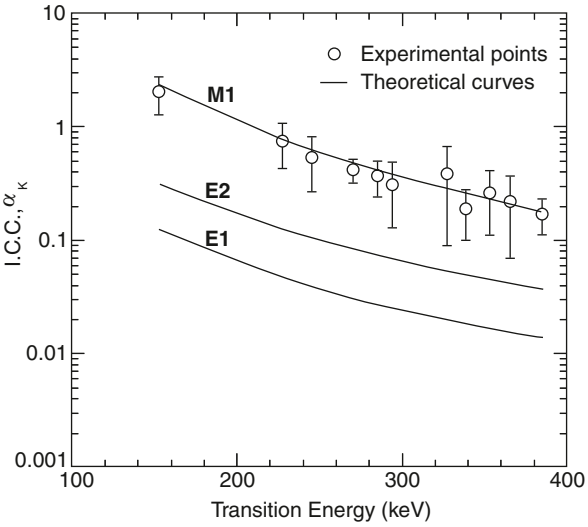

Fig. 2.11 The experimental values of K-shell internal conversion coefficients, α_K [13] versus transition energy, for the in-band, low-energy gamma-ray transitions for band 1 in ^{197}Pb. The *solid lines* are the corresponding theoretical values [34] for the pure M1, E2 and E1 transitions

The spins and parities of the $\Delta I = 1$ bands in most of the Pb isotopes have been assigned from the information on multipole order and character of the in-band transitions and those of the decay-out transitions connecting the $\Delta I = 1$ band to the low spin states in the nucleus and from the knowledge of J^{π} of the low spin states.

Having now known the level schemes, the magnetic dipole nature of the in-band transitions and the assignment of spins and parities of the levels in the $\Delta I = 1$ bands in the Pb isotopes, attention will now be paid to the nucleon configuration and the coupling of angular momenta of the participating nucleons for the bandhead states of these bands. We shall then talk about deformation of the bandhead states.

2.2.2.2 Nucleon Configurations and Coupling of Angular Momenta

Amongst the several $\Delta I = 1$ bands observed in Pb nuclei, the most intense are the lowest lying negative parity and the positive parity bands. These bands are built on $[\pi(s_{1/2}{}^{-2}\, h_{9/2}i_{13/2})11^{-} \otimes \nu i_{13/2}{}^{-n}]$ configuration (where $n = 1, 2, 3,\ldots$) with the possible addition for some bands of one or more low-j neutrons of $f_{5/2}$ and $p_{3/2}$ origin. For the negative parity $\Delta I = 1$ bands in the odd Pb isotopes, the suggested [26 and references therein] configuration of the band head states is $[\pi(s_{1/2}{}^{-2}h_{9/2}\, i_{13/2})11^{-} \otimes \nu i_{13/2}{}^{-1}]$. The g-factor of the $29/2^{-}$ $T_{1/2} = 9$ ns band head state of band 1 in ^{193}Pb was determined [35] by the time-dependent perturbed angular distribution (TDPAD) method. The result obtained is

$$g_{\mathrm{exp}}[2584\ \mathrm{keV\ level}] = 0.68\ (3).$$

The g-factor of the state can be calculated using the experimental values of the g-factors of the individual components of the nucleon configuration for which the average values [36] are

$$g\left[\pi\left(h_{9/2}\, i_{13/2}\right)11^{-}\right] = 1.11\ (2)$$

and

$$g\left(\nu i_{13/2}{}^{-1}\right) = 0.150\ (6).$$

Using the additivity relation for magnetic moments

$$g_{\mathrm{calc}}\left[\pi\left(h_{9/2}\, i_{13/2}\right)11^{-} \otimes \nu i_{13/2}{}^{-1}\right] = 0.71\ (4),$$

which agrees well with the experimentally determined value of g-factor. Other plausible nucleon configurations give g-factor values in disagreement with the measured result. This confirms the above-mentioned-suggested configuration for the band head state on which $\Delta I = 1$ band 1 in ^{193}Pb is based.

The lowest energy for this repulsive particle–hole coupling is expected for a perpendicular orientation of the proton and neutron spins. Since the g-factor is determined by component of magnetic dipole moment along the spin vector, the

agreement between the experimental and the calculated g-factors confirms approximately perpendicular coupling of the proton particle and the neutron-hole spins.

The nucleon configuration $\left[\pi\left(h_{9/2}\, i_{13/2}\right)11^- \otimes \nu\left(i_{13/2}{}^{-1}\right)\right]$ and the approximately perpendicular coupling of the proton-particle and neutron-hole spins have, therefore, been adopted for all the negative parity $\Delta I = 1$ bandhead states in odd-mass Pb isotopes.

For the lowest lying positive parity $\Delta I = 1$ bands in odd Pb isotopes, the suggested configuration [26 and the references therein] for the bandhead states is

$$\left[\pi\left(h_{9/2}\, i_{13/2}\right)11^- \otimes \nu\left(i_{13/2}{}^{-2}\, f_{5/2}{}^{-1}\right)\right].$$

Let us now consider the lowest energy $\Delta I = 1$ bands in the even-mass Pb isotopes. A glance at the 16^- bandhead states in ^{194}Pb (band 1a in Fig. 2.5), ^{196}Pb (band 2 in Fig. 2.6) and ^{198}Pb (band 3 in Fig. 2.8) shows that most of the band intensity passes through the $\pi(h_{9/2}\, i_{13/2})\ 11^-$ states. This suggests the involvement of the $\pi(h_{9/2}\, i_{13/2})\ 11^-$ configuration in the 16^- bandhead states of the negative parity $\Delta I = 1$ bands. The suggested [26 and references therein] configuration of the bandhead states for these bands is

$$\left[\pi\left(h_{9/2}\, i_{13/2}\right)11^- \otimes \nu\left(i_{13/2}{}^{-2}\right)\right].$$

The suggested [26 and references therein] configuration of the lowest energy positive parity $\Delta I = 1$ bandhead states in ^{194}Pb (band 2a in Fig. 2.5), ^{196}Pb (band 1 in Fig. 2.6) and ^{198}Pb (band 1 in Fig. 2.7) is

$$\left[\pi\left(h_{9/2}\, i_{13/2}\right)11^- \otimes \nu\left(i_{13/2}{}^{-1}\, f_{5/2}{}^{-1}\right)\right].$$

2.2.2.3 Deformation of Bandhead States

Deformation of the bandhead states of the $\Delta I = 1$ bands can be estimated through the measurement of spectroscopic quadrupole moments, Q_s, of the states. The level lifetimes for most of the states are too short for such measurements. As mentioned earlier, the $29/2^-$ bandhead state of band 1 in ^{193}Pb has a halflife of 9 ns which is just long enough for the measurement of quadrupole moment. The Q_s for this state has been measured by the TDPAD method [37] in an attempt to determine the deformation of the state. The value obtained is $|Q_s| = 2.84\ (26)$ eb. This value is much larger than that for the $\nu(i_{13/2}{}^{-2})\ 12^+$ isomers in the neighbouring even–even Pb isotopes. The spectroscopic quadrupole moments, Q_s, for the 12^+ states in ^{192}Pb, ^{194}Pb and ^{196}Pb have been measured [21, 38, 39], the values for which are given below:

Nucleus	Q_s [12^+ state] (eb)	Reference
^{192}Pb	0.32 (4)	[21]
^{194}Pb	0.48 (3)	[38]
^{196}Pb	0.65 (5)	[39]

These Q_s values indicate small deformation for the 12+ states. It, therefore, appears that the deformation of the bandhead state of band 1 in ^{193}Pb, for which the nucleon configuration is

$$\left[\pi\left(\mathrm{h}_{9/2}\ \mathrm{i}_{13/2}\right)11^- \otimes \nu\mathrm{i}_{13/2}{}^{-1}\right],$$

is dominated by the deformation of the $\left[\pi\left(\mathrm{h}_{9/2}\,\mathrm{i}_{13/2}\right)11^-\right]$ proton particle state. The spectroscopic quadrupole moments were measured for the 11^- isomeric states [21, 22] in the neighbouring even–even Pb isotopes. The values obtained are as follows:

Nucleus	Q_s [11^- state] (eb)	Reference
^{192}Pb	2.9 (3)	[21]
^{194}Pb	3.6 (4)	[21]
^{196}Pb	3.41 (66)	[22]

The intrinsic quadrupole moment, Q_0, can be estimated from Q_s experimental using the strong coupling formalism, assuming here $K = I$ and using the relation

$$Q_s = Q_0 \frac{3K^2 - I(I+1)}{(2I+3)\,(I+1)}.$$

The quadrupole deformation parameter β_2 can be derived from Q_0 using the relation

$$Q_0 = \frac{3ZR^2\beta_2}{\sqrt{5\pi}},$$

where $R = r_o\, A^{1/3}$ and $r_o = 1.2$ fm. Assuming oblate shape, the average quadrupole deformation obtained for the 11^- states is $\beta_2 = -0.146$ (14) [21]. The Q_s value obtained for the 29/2 state in ^{193}Pb is similar to the values obtained for the 11^- isomers in the above even–even Pb isotopes. Therefore, the quadrupole deformation of the 29/2 bandhead state in ^{193}Pb can be taken as $\beta_2 \sim -0.14$. It may be mentioned here that the deformation of the 29/2 state cannot be directly determined from the measured Q_s as this state is not a high K isomer—K is not a good quantum number and so the strong coupling model cannot be applied to determine β_2.

2.2.2.4 Bandcrossings in $\Delta I = 1$ Bands

Shorthand notations for band configurations, which are the standard cranked shell model band classifications, as introduced in [30], will be used below for a discussion on bandcrossings in the $\Delta I = 1$ bands in the Pb isotopes. Since in the Pb region, the Fermi level is located well below the shell gap $N = 126$, neutron pairing plays an important role. Therefore, the lowest energy positive parity neutron configurations of $\mathrm{i}_{13/2}$ origin are labelled by the letters A, B, C, D,… for quasi-neutrons and by E,

F for natural parity (negative parity) quasi-neutrons of predominantly $f_{5/2}$ and $p_{3/2}$ origin. The proton pairing is neglected as the two proton particles involved in the $\Delta I = 1$ band configurations are the 2p–2h excitations across the $Z = 82$ closed shell gap. The proton configuration is, therefore, labelled by the spin quantum number. For example, the negative parity proton configuration $\pi(h_{9/2}\, i_{13/2})K^{\pi} = I^{\pi} = 11^{-}$ is abbreviated as 11. Bandhead configurations for the low-lying strongest $\Delta I = 1$ bands in this notation are as follows:

Nucleus and band	Configuration	Shorthand notation
Odd Pb isotopes		
Negative parity bands 1	$[\nu(i_{13/2}{}^{-1}) \otimes \pi(h_{9/2}\, i_{13/2})11^{-}]$	A11
Positive parity bands 2	$[\nu(i_{13/2}{}^{-2}\, f_{5/2}{}^{-1}) \otimes \pi(h_{9/2}\, i_{13/2})11^{-}]$	ABE11
Even Pb isotopes		
Negative parity bands	$[\nu(i_{13/2}{}^{-2}) \otimes \pi(h_{9/2}\, i_{13/2})11^{-}]$	AB11
Positive parity bands	$[\nu(i_{13/2}{}^{-1}\, f_{5/2}{}^{-1}) \otimes \pi(h_{9/2}\, i_{13/2})11^{-}]$	AE11

In the left panel of Fig. 2.12 [26] is given a plot of angular momentum as a function of rotational frequency which is taken as $\hbar\omega = E_{\gamma}$ for the dipole transitions, for the strongest negative parity $\Delta I = 1$ bands 1 in odd-mass Pb isotopes. These bands have configuration A11 at low spins and show a bandcrossing (except in the case of ^{201}Pb) at a rotational frequency, $\hbar\omega \sim 0.3$ MeV with a gain in alignment of $\sim 8\hbar$. This has been interpreted [26 and references therein] as the decoupling and rotational alignment of the BC neutron pair. Therefore, the configuration of band 1

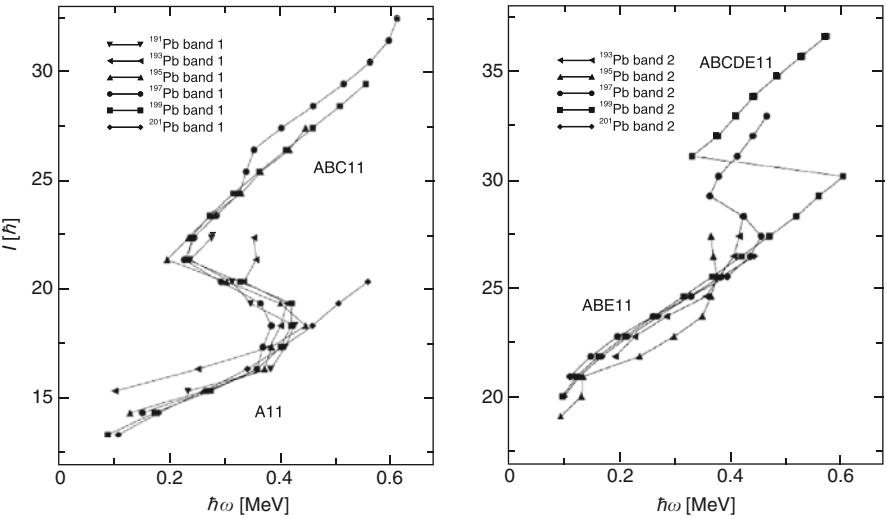

Fig. 2.12 Plots of spin versus rotational frequency for the strongest negative parity (*left panel*) and strongest positive parity (*right panel*) $\Delta I = 1$ bands in odd-mass Pb isotopes. (Figure taken with permission from [26])

is A11 before bandcrossing and ABC11 after the bandcrossing. An irregularity is seen only in the case of band 1 of ^{197}Pb, at $\hbar\omega \sim 0.35$ MeV with an alignment gain of ~2$\hbar$. This has been attributed [26 and references therein] to the alignment of the natural parity neutrons EF. In the same band, another irregularity is observed at $\hbar\omega \sim 0.6$ MeV indicating a configuration change in the neighbourhood of this rotational frequency. Data to such high rotational frequencies do not exist for band 1 in the other odd-mass Pb isotopes.

The right panel of Fig. 2.12 shows a similar plot as in the left panel for the strongest positive parity bands (bands 2) in the odd-mass Pb isotopes. At low spins, the configuration of the bands is ABE11. At a rotational frequency of $\hbar\omega \sim 0.45$ MeV, this band in ^{199}Pb is crossed by a new structure which involves the decoupling and rotational alignment of the CD ($i_{13/2}$) neutron pair with a large alignment gain. Similar bandcrossing with less alignment gain also occurs for band 2 in ^{197}Pb. The configuration of bands 2 above this bandcrossing is ABCDE11 [26 and references therein].

Let us now consider the bandcrossing phenomenon for the $\Delta I = 1$ bands in the even-mass Pb isotopes. Plots of angular momentum as a function of rotational frequency for the strongest negative parity bands (left panel) and the strongest positive parity bands (right panel) in the even-mass Pb isotopes are shown in Fig. 2.13. The configuration of the negative parity bands is AB11 below and ABCD11 above the bandcrossing respectively [26 and references therein] due to the rotational alignment of the CD neutron pair at $\hbar\omega \sim 0.42$ MeV. No bandcrossing is observed in ^{200}Pb. For the positive parity bands, the configuration is AE11 below and ABCE11 above the bandcrossing [26 and references therein]. This bandcrossing is due to

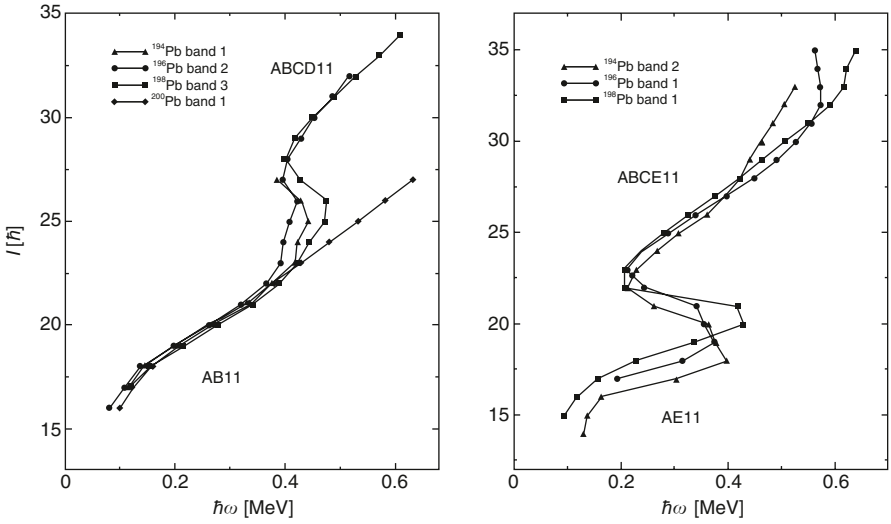

Fig. 2.13 Plot of angular momentum, I, as a function of rotational frequency, $\hbar\omega$, for the strongest negative parity bands (*left panel*) and the strongest positive parity bands (*right panel*) in the even-mass Pb isotopes. (Figure taken with permission from [26])

the occurrence of the alignment of the BC neutron pair at a rotational frequency of $\hbar\omega \sim 0.3$ MeV with an alignment gain of ~8$\hbar$.

2.2.2.5 Electromagnetic Properties of $\Delta I = 1$ Bands

Electromagnetic properties of the $\Delta I = 1$ bands, which play an important role in the understanding of nuclear structure of these bands, can be obtained from the absolute values of the reduced M1 and E2 transition probabilities, B(M1) and B(E2), respectively. These reduced transition probabilities can be deduced from lifetime measurements of excited states of the band from where the branching into M1 and E2 transitions occur. In most of the cases in $\Delta I = 1$ bands, the M1 transitions are strong whereas the cross-over E2 transitions are either weak or cannot be detected because of very weak gamma-ray intensities. The B(M1) values are sensitive to the details of nucleon configuration of the coupled multi-quasi particle high-j state, coupling scheme of nucleon angular momentum vectors and their contribution to the component of magnetic dipole moments perpendicular to the total angular momentum vector. The larger is this component, the larger is the M1 strength (actually, B(M1) $\propto$ the square of the magnitude of this component). The B(E2) values provide information about the deformation of the system. It is always not possible to measure lifetimes of nuclear states and deduce the absolute B(M1) and B(E2) values. In such a situation, the B(M1)/B(E2) ratios are very useful to get an insight into the details of nuclear structure. It may be mentioned here that bulk of such information has been obtained through these ratios in a large number of deformed rotational bands in nuclei.

Although accurate lifetime measurements are now available for excited states in many of the $\Delta I = 1$ bands in the Pb region, we will still talk about the B(M1)/B(E2) ratios which can be deduced from experiments using the expression [40]

$$B(\mathrm{M1})/B(\mathrm{E2}) = \frac{0.6968 E\gamma_2^5}{\lambda\ E\gamma_1^3\left(1+\delta^2\right)}(\mu_\mathrm{N}/\mathrm{eb})^2,$$

where $E\gamma_1$, $E\gamma_2$ are the gamma-ray energies in MeV for the M1($I \rightarrow I-1$) and E2($I \rightarrow I-2$) transitions, respectively, from a state I, and λ is the measured gamma-ray intensity ratio [$I(\gamma_2)/I(\gamma_1)$]. The mixing ratio δ^2 can be neglected since the in-band transitions are predominantly M1 (e.g. see Fig. 2.11) and strong compared to the E2($I \rightarrow I-2$) transitions.

In Fig. 2.14 are shown the B(M1)/B(E2) ratios as a function of angular momentum for the 'case study' $\Delta I = 1$ band, band 1 in ^{197}Pb [26]. Considering also the other $\Delta I = 1$ bands in ^{197}Pb and ^{198}Pb [26], the average value of the B(M1)/B(E2) ratio lies around 30 $(\mu_\mathrm{N}/e\mathrm{b})^2$. This is much larger than the ones in rotational bands in deformed nuclei, e.g. it is ~0.5–5 $(\mu_\mathrm{N}/e\mathrm{b})^2$ in ^{157}Ho [41]. The uncertainties in the ratios shown in the figure are large because of weak gamma-ray intensities of the E2 cross-over transitions. Note an abrupt increase in the B(M1)/B(E2) ratio at the bandcrossing at $I \sim 20\hbar$.

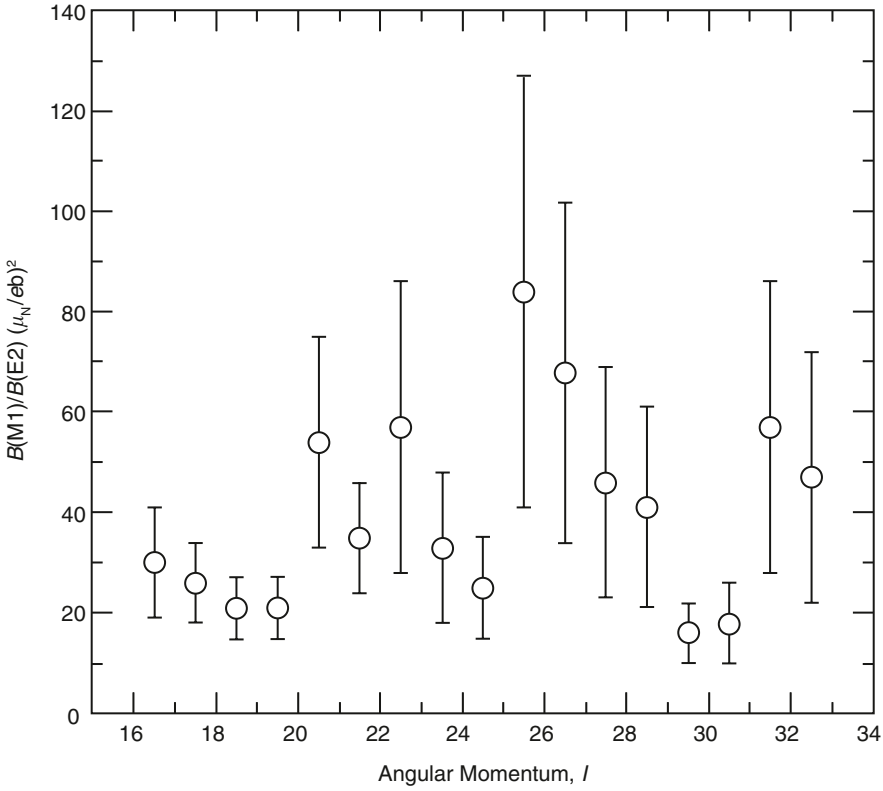

Fig. 2.14 Plot of B(M1)/B(E2) ratios as a function of angular momentum for the $\Delta I = 1$ band 1 in ^{197}Pb [26]

Accurate mean lifetimes in the pico- to sub-picosecond region have been measured for excited states in several $\Delta I = 1$ bands in the Pb isotopes using the Doppler shift methods and high photopeak detection efficiency arrays GAMMASPHERE and the EUROBALL. The Recoil Distance Method (RDM) has been used for low spin members in some of these bands while for the high spin states, the Doppler Shift Attenuation Method (DSAM) was employed. From the measured lifetimes, absolute experimental values of reduced transition probability B(M1), assuming the $\Delta I = 1$ in-band transition of pure M1 character, is obtained from the expression [40]

$$B(\mathrm{M1}) = \frac{0.05697 B\gamma_1}{E\gamma_1^3 \tau [1 + \alpha_t(\mathrm{M1})]} (\mu_N)^2,$$

where $E\gamma_1$ is the gamma-ray energy in MeV of the M1 transition, τ is the level lifetime in ps, α_t(M1) is the total theoretical M1 internal conversion coefficient and the branching ratio $B\gamma_1 = I\gamma(\mathrm{M1}) \big/ \left[I\gamma(\mathrm{M1}) + I\gamma(\mathrm{E2}) \right]$ is obtained from the measured gamma-ray intensities of the M1 and the cross-over E2 transitions. In

some cases the cross-over E2 transitions are very weak and not observed. In such cases the M1 branching ratio is unity.

The experimental B(E2) reduced transition probability is also deduced from the measured lifetime τ, using the expression [40]

$$B(\mathrm{E2}) = \frac{0.08156 B \gamma_2}{E \gamma_2^5 \tau [1 + \alpha_t (\mathrm{E2})]} \quad (\mathrm{eb})^2.$$

The total internal conversion coefficient α_t(E2) is small and can be neglected as the energy of the cross-over E2 transition is large (~0.5–1.2 MeV).

Figure 2.15 shows plots of experimental values of reduced M1 transition probability B(M1), for intraband transitions in the $\Delta I = 1$ bands in $^{193–199}$Pb, deduced from lifetime measurements [42–47], as a function of spin of the initial state. The values are from DSAM measurements except shown by diamonds which are the RDM determinations. This figure is taken from [48]. The curves are the results of tilted axis cranking (TAC) calculations [48]. This will be discussed in the section on interpretation of $\Delta I = 1$ bands (Sect. 2.2.3). In all the above-mentioned Pb isotopes, for the mentioned band configurations, the experimental B(M1) values show a characteristic decrease with spin—a result of immense significance for the

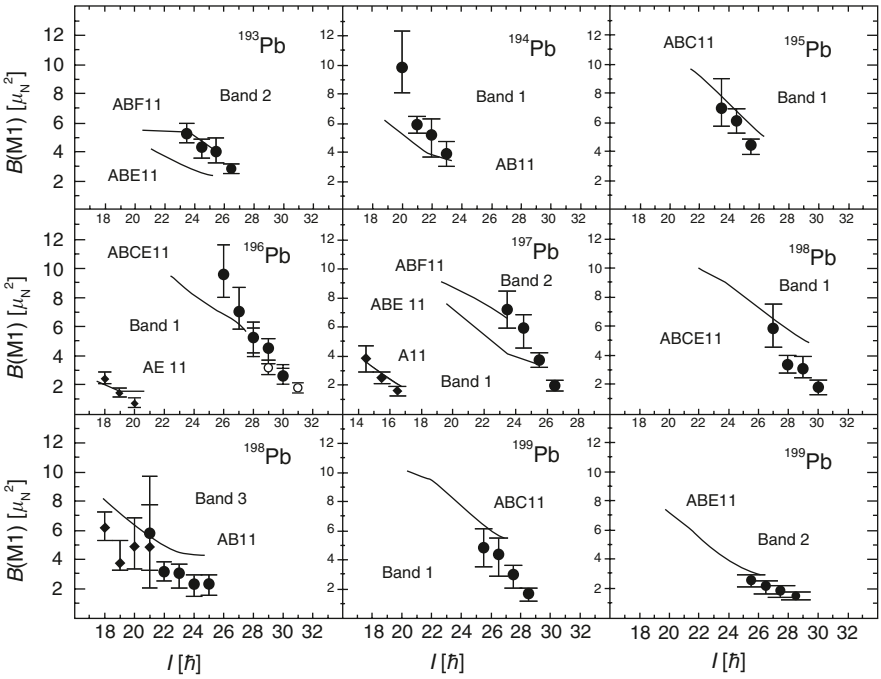

Fig. 2.15 Plots of experimental reduced transition probabilities, B(M1), as a function of spin of the initial state for in-band M1 transitions in $\Delta I = 1$ bands in $^{193–199}$Pb. See text for details. (Figure taken with permission from [48])

phenomenon of generation of angular momentum in these $\Delta I = 1$ bands. It can also be seen from this figure that the B(M1) values differ for different configurations (given in shorthand notation in the figure) of the bands and are drastically different for band configurations with a different number of aligned neutrons. For band 1 in ^{196}Pb, the band configuration is AE11 before and ABCE11 after the band crossing (see Fig. 2.13). In this band, below the bandcrossing, the B(M1) values decrease from 2.4 to 0.7 μ_N^2. Above the bandcrossing, the B(M1) value jumps to ≈9 μ_N^2 and drops to 1.8 μ_N^2 with increasing spin. As will be explained later (see Sect. 2.2.4), this big jump in the B(M1) values is due to the shears opening as a result of the rotational alignment of an $i_{13/2}$ BC neutron pair. In ^{197}Pb, band 1 and band 2, before bandcrossing, the configurations are A11 and ABE11, respectively (see Fig. 2.12). Note the different B(M1) values for these configurations in the figure (Fig. 2.15).

Figure 2.16 depicts the reduced B(E2) transition probabilities, deduced from lifetime measurements [42–47], for intraband transitions in $\Delta I = 1$ bands in $^{193-199}$Pb, as a function of spin of the initial state. The symbols have the same meaning as in Fig. 2.15. The curves are the results of TAC calculations [48]. As the B(E2) values have large errors because of the cross-over transitions being weak, it is not possible to know whether the B(E2) values are constant as a function of spin. In band 1 in ^{197}Pb, at low spins, where the B(E2) values have relatively smaller errors, these are seemingly constant. In general, the B(E2) values are small which indicates a small

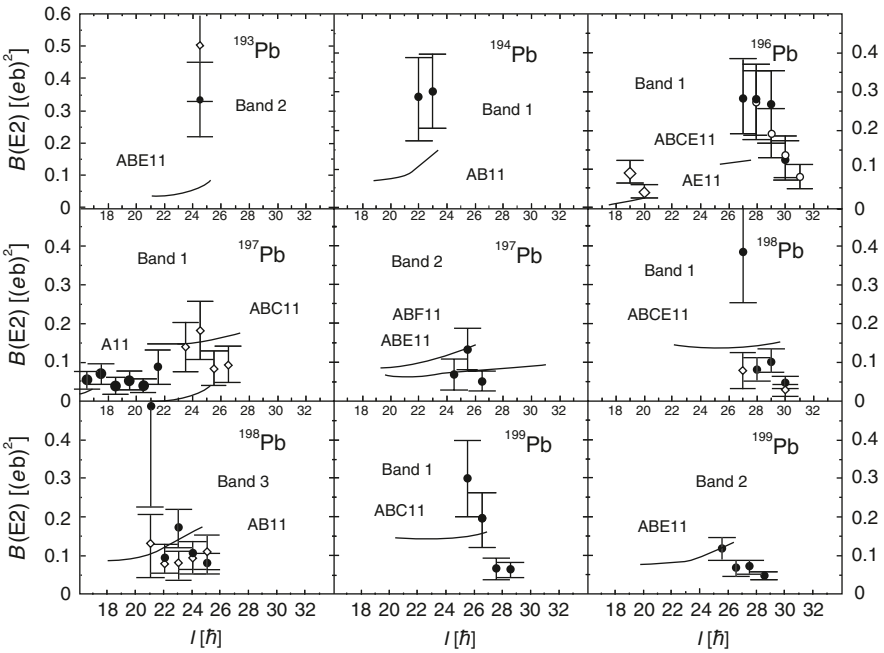

Fig. 2.16 Same as in Fig. 2.15 but for the reduced transition probabilities, B(E2). See text for details. (Figure taken with permission from [48])

deformation of the nucleus. However, this point will be discussed further in the section on the interpretation of these $\Delta I = 1$ bands.

2.2.2.6 $\Delta I = 1$ Bands in Lighter Mass Regions

Several $\Delta I = 1$ bands have been observed in the nearly spherical nuclei in mass regions $A \sim 80$, 100–110 and 140 [14 and references therein]. All these $\Delta I = 1$ bands in the lighter mass regions have properties similar to those observed for the $\Delta I = 1$ bands in Pb isotopes which have been discussed at length in the previous sections. The nucleon configurations for the $\Delta I = 1$ bands in the mass regions are as follows:

Mass region	Bandhead configuration
80	$\pi(g_{9/2}{}^{n}) \otimes \nu(g_{9/2}{}^{-n})$
100–110	$\pi(g_{9/2}{}^{-n}) \otimes \nu(h_{11/2}{}^{n})$
140	$\pi(h_{11/2}{}^{n}) \otimes \nu(h_{11/2}{}^{-n})$

Very recently, four $\Delta I = 1$ bands have been found in ^{60}Ni [49] which possibly have nucleon configurations involving one $1f_{7/2}$ proton hole and $1g_{9/2}$ neutron particle(s).

2.2.3 *Theoretical Interpretation of the $\Delta I = 1$ Bands*

One of the important experimental observations in $\Delta I = 1$ bands in the Pb region and in the lighter mass regions, as mentioned in the earlier sections, is that these bands are always built upon bandhead states which are excitations of high spin particles coupled to high spin hole states and never upon only the high spin particle or the high spin hole states alone. A g-factor measurement [35] of the band head state of band 1 in ^{193}Pb established the nucleon configuration of this state to be $\left[\pi\left(h_{9/2}i_{13/2}\right)11^{-} \otimes \nu(i_{13/2}{}^{-1})\right]$. This experiment also confirmed an approximately perpendicular coupling of the proton particle and neutron-hole spins.

The observed $\Delta I = 1$ bands are rotational-like bands.

The bands have strong in-band M1 transitions and the cross-over E2 transitions are either weak and, in some cases, not even observed. The bandhead states are weakly oblate deformed ($\beta_2 \approx -0.14$) as indicated by the spectroscopic quadrupole moment measurement [37] of the bandhead state in band 1 in ^{193}Pb and those for the proton particle 11^{-} states in the even Pb isotopes [21, 22].

Another significant observation has come from the accurate lifetime measurements of excited states in the $\Delta I = 1$ bands in the Pb isotopes. The experimentally deduced reduced transition probabilities B(M1) are large (up to several $\mu_N{}^2$) and decrease characteristically with increasing spin (see Fig. 2.15). The obtained B(E2) values are small (~0.1 e^2b^2) in many cases (see Fig. 2.16) indicating small deformation.

The above-mentioned experimental findings greatly helped in the theoretical understanding of these $\Delta I = 1$ bands.

Amongst the various theoretical approaches which provide insight into the phenomenon of $\Delta I = 1$ bands and their properties in near spherical light Pb isotopes and in the lighter mass regions is the pioneering work of Frauendorf [8] within the framework of the TAC calculations. Frauendorf et al. [50] also did spherical shell model calculations in a reasonable configuration space to interpret the observed $\Delta I = 1$ bands. Later, Macchiavelli et al. [51–53] presented a semi-classical analysis of the process of generation of angular momentum in these bands, predictions of reduced transition probabilities B(M1) and B(E2), and an effective interaction between the neutron and proton forming each 'blade' of the system to provide an answer to the rotation-like behaviour of these $\Delta I = 1$ bands. An integrated view of these ideas is contained in a review article by Clark and Macchiavelli [15].

Still another approach has been the calculations using the particle rotor model. In [54], competition between the process generating angular momentum in the $\Delta I = 1$ bands and the core rotation was investigated through the particles-plus-rotor model. The phenomena of signature splitting and signature inversion in some of the $\Delta I = 1$ bands in the Pb isotopes were studied in [55]. In the many particle plus rotor model description [56] of the $\Delta I = 1$ bands in the Pb isotopes, the reduced transition probabilities B(M1) and B(E2) have been calculated as a function of initial spin and the results are compared with experimental data on band 1 in ^{199}Pb. This theory also considers the question of band termination in these bands.

In this section, we will consider the TAC approach.

2.2.3.1 Angular Momentum Coupling Scheme

Let us consider the coupling of the high-Ω proton particles and low-Ω neutron hole orbitals in the tilted axis representation. The density distribution of the $h_{9/2}$ and $i_{13/2}$ protons is torus-like and that of the $i_{13/2}$ neutron holes dumb-bell like. The proton particle spin, $\boldsymbol{j}_\pi$, prefers deformation alignment, i.e. it is parallel to the symmetry axis (3-axis) of the nucleus which is weakly oblate deformed. The neutron-hole spin, $\boldsymbol{j}_\nu$, prefers alignment perpendicular to $\boldsymbol{j}_\pi$ (rotation aligned). This type of coupling results in maximum overlap of the density distributions of the proton particles and the neutron holes and minimum system energy (bandhead energy). This situation is shown in the schematic drawing of the coupling scheme in Fig. 2.17a. The total angular momentum, $\boldsymbol{I}$, then lies along a tilted axis at an angle θ (tilt angle) with respect to the symmetry axis. The angular momentum is restricted to lie in the principal plane formed by the 3- and the 1-axis. The angular momentum and energy in the $\Delta I = 1$ band are increased by a step-by-step alignment of $\boldsymbol{j}_\pi$ and $\boldsymbol{j}_\nu$ towards the total angular momentum vector, $\boldsymbol{I}$. The angle between the $\boldsymbol{j}_\pi$ and $\boldsymbol{j}_\nu$ vectors decreases but as will be shown later, the tilt angle, θ, remains nearly constant. This is shown in Fig. 2.17b. Finally (see Fig. 2.17c), the particle and hole spins fully align parallel to the total angular momentum, $\boldsymbol{I}$. This corresponds to the maximum spin state of the band of the assigned nucleon configuration. The band then termi-

nates at this maximum spin. This whole process of closing of proton and neutron vectors (blades), j_π and j_ν, is similar to the closing of sheep shears and, therefore, this process of angular momentum generation in $\Delta I = 1$ bands has been called the 'shears mechanism' and the bands the 'shears bands' [30].

The magnetic dipole moment of the high-j protons is large and positive, i.e. in the direction of j_π, whereas that of high-j neutrons is small, as a result of no orbital contribution, and negative. The magnetic dipole moment components of the protons and neutrons are also shown schematically in the coupling scheme diagrams. The addition of components, $\mu_\pi^\perp$ and $\mu_\nu^\perp$, perpendicular to the total angular momentum, I, gives a large value of $\mu_{\text{tot}}^\perp$ which breaks the rotational symmetry of the quantal system (similar to what the charge distribution does in deformed nuclei).

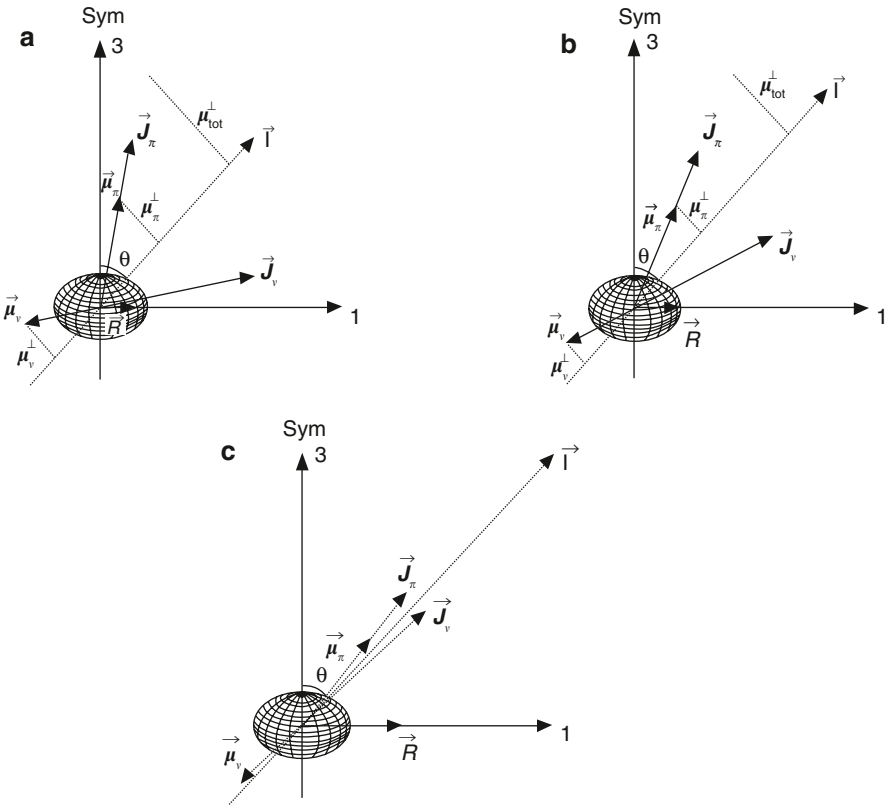

Fig. 2.17 Angular momentum coupling scheme of shears mechanism in a $\Delta I = 1$ band in a weakly oblate deformed nucleus in the Pb region **a** at low rotational frequency (at bandhead), **b** at intermediate rotational frequency and **c** at maximum rotational frequency. The perpendicular magnetic dipole moments are also shown schematically. See the text for details. (Figure taken with permission mainly from [14]; figure **c** courtesy Professor A. K. Jain)

Since in the TAC approach, uniform rotation of the nucleus is considered around an axis parallel to $\boldsymbol{I}$, the total perpendicular component of the magnetic dipole moment $\boldsymbol{\mu}_{\mathrm{tot}}^{\perp}$, rotates around $\boldsymbol{I}$. In analogy with the rotation of deformed nucleus where the electric quadrupole moment rotates around the total angular momentum, the new excitation mode is called 'magnetic rotation' and the $\Delta I = 1$ bands the 'magnetic rotational bands'.

As shown in Fig. 2.17a–c, the perpendicular component of the total magnetic dipole moment $\boldsymbol{\mu}_{\mathrm{tot}}^{\perp}$ decreases in a characteristic manner with increase in spin and excitation energy in the $\Delta I = 1$ band, due to the closing of the shears (alignment of $\boldsymbol{j}_{\pi}$ and $\boldsymbol{j}_{\nu}$ towards $\boldsymbol{I}$). The perpendicular component $\boldsymbol{\mu}_{\mathrm{tot}}^{\perp}$ finally vanishes for the situation when $\boldsymbol{j}_{\pi}$ and $\boldsymbol{j}_{\nu}$ align along $\boldsymbol{I}$ (see Fig. 2.17c). Since B(M1) is proportional to $\left|\boldsymbol{\mu}_{\mathrm{tot}}^{\perp}\right|^2$, the B(M1) values should also decrease characteristically with increasing spin in the band. This is what is observed experimentally through accurate measurement of lifetimes of excited states in the $\Delta I = 1$ bands in neutron-deficient Pb isotopes (see Fig. 2.15). These measurements, therefore, provide a strong experimental evidence for the existence of the shears mechanism of the generation of angular momentum in such bands. The B(M1) values obtained in the TAC model will be discussed later.

2.2.3.2 Recent Results from TAC Calculations

Recently, Chmel et al. [48] made detailed calculations of tilt angles, deformation parameters, angular momenta and reduced magnetic dipole and electric quadrupole transition probabilities, B(M1) and B(E2), respectively, within the framework of the TAC model for the shears/magnetic rotational bands ($\Delta I = 1$ bands) in the neutron-deficient Pb isotopes ^{193}Pb to ^{202}Pb. In this work [48], the pairing-plus-quadrupole-quadrupole version of the tilted axis cranking (PQTAC) model [8, 57, 58] was applied for the above-mentioned calculations. Details of the various parameters used in the calculations are also discussed in [48].

In the following, the results of the PQTAC model calculations will be discussed. Fig. 2.18 gives a plot of the tilt angles θ as a function of rotational frequency, $\hbar\omega$, for the A11 (see Fig. 2.12) and the AB11 (see Fig. 2.13) configurations of the $\Delta I = 1$ bands in the Pb isotopes. It is observed that the tilt angle varies little with rotational frequency for a given isotope and for a particular configuration. This suggests that the shears mechanism plays a dominant role in the generation of angular momentum in these bands. The tilt angle varies with neutron number of the different isotopes. This is due to the changes of neutron Fermi level. The tilt angle is different for the A11 $\left[\nu(\mathrm{i}_{13/2}{}^{-1}) \otimes \pi\left(\mathrm{h}_{9/2}\,\mathrm{i}_{13/2}\right)11^{-}\right]$ and the AB11 $\left[\nu(\mathrm{i}_{13/2}{}^{-2}) \otimes \pi\left(\mathrm{h}_{9/2}\,\mathrm{i}_{13/2}\right)11^{-}\right]$ configurations. It becomes larger when an $\mathrm{i}_{13/2}$ neutron hole is added which gives an extra spin component perpendicular to the 3-axis. In band 1 in ^{197}Pb (see Fig. 2.3 for level scheme), before bandcrossing, the configuration is A11 and after bandcross-

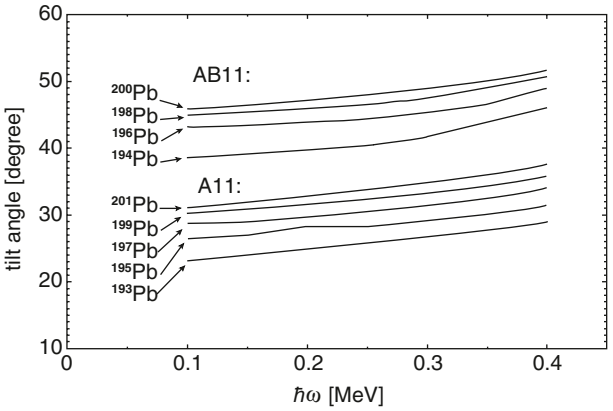

Fig. 2.18 Calculated [48] tilt angles θ (see Fig. 2.17a) as a function of rotational frequency for $\Delta I = 1$ bands of A11 and AB11 nucleon configurations in $^{193-201}$Pb. (Figure taken with permission from [48])

ing, it is ABC11 with the rotation alignment of a BC $i_{13/2}$ neutron pair. The tilt angle nearly doubles in magnitude after bandcrossing (see Table 1 in [48]).

The deformation parameters ε_2 (=0.95 β_2 for small deformations) and γ have also been calculated in the PQTAC model [48]. These values for A11 and AB11 configurations are shown as a function of rotational frequency, $\hbar\omega$, in Fig. 2.19. The quadrupole deformations are small, typically $\varepsilon_2 \sim -0.10$ and it remains constant within the bands. This value is somewhat smaller than a value of $\beta_2 \sim -0.14$ adopted in Sect. 2.2.2.3 for the bandhead state of band 1 in ^{193}Pb. The triaxiality is found to be small in all the cases considered. There is less than about 10% variation from the value for axial symmetry ($\gamma = -120°$ with ε_2 negative).

In Fig. 2.15, plots of experimentally deduced B(M1) values as a function of initial state spin, for the $\Delta I = 1$ in $^{193-199}$Pb, are shown. It is observed that the B(M1) values characteristically decrease with increasing spin (see also Sect. 2.2.2.5). The

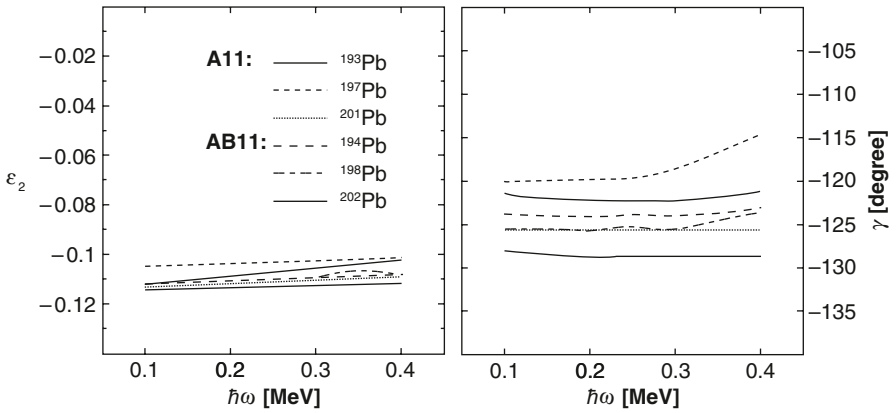

Fig. 2.19 Calculated [48] deformation parameters, ε_2 (*left panel*) and γ (*right panel*) for the A11 and AB11 nucleon configurations as a function of rotational frequency for some $\Delta I = 1$ bands in Pb isotopes. (Figure taken with permission from [48])

calculated B(M1) values from the PQTAC model [48] are shown as curves in the figure. The calculations reproduce the decrease in B(M1) values with increasing spin reasonably well. This is a convincing evidence of the existence of the shears mechanism of generation of angular momentum in the $\Delta I = 1$ bands.

The calculated B(E2) values for the Pb isotopes using the PQTAC model [48], as a function of initial state spin, are shown as curves in Fig. 2.16. These are compared with the experimentally deduced values from lifetime measurements (see also Sect. 2.2.2.5). For band 1 in ^{197}Pb, at low spins (below bandcrossing), where the experimental B(E2) values have relatively small errors, the calculated values are in good agreement with the experimental data. Both the values show a constant trend with increasing spin. This is an indication that the calculated almost constant quadrupole deformation of $\varepsilon_2 \approx -0.1$ could be accepted at least for the $\Delta I = 1$ magnetic rotational band—band 1 in ^{197}Pb. The question whether the quadrupole deformation is constant for all magnetic rotational bands, away from the bandcrossing regions, can be decided when accurate values of B(E2) are available from experiments.

2.2.4 Band Termination

Maximum spin state for a given configuration in a shears band is reached when the proton particle and the neutron-hole spins align parallel to the total angular momentum vector, $\boldsymbol{I}$ (i.e. when the shears close). This is schematically shown in Fig. 2.17c. The shears band then terminates. Let us take the example of band 2 in ^{199}Pb (see level scheme in Fig. 2.4). For this positive parity shears or magnetic rotational band, angular momentum, $\boldsymbol{I}$, is plotted as a function of transition energy, E_γ of the in-band M1 gamma-ray transitions, in Fig. 2.20. As mentioned in Sect. 2.2.2.4, the nucleon configuration of the band below bandcrossing is $\left[\nu(i_{13/2}{}^{-2} f_{5/2}{}^{-1}) \otimes \pi\left(h_{9/2} i_{13/2}\right) 11^-\right]$ and after the rotational alignment of a CD $\nu i_{13/2}{}^{-2}$ neutron hole pair, it is $\left[\nu(i_{13/2}{}^{-4} f_{5/2}{}^{-1}) \otimes \pi\left(h_{9/2} i_{13/2}\right) 11^-\right]$. To start with, the bandhead spin is 35/2, which is obtained by a near 90° coupling of proton spin of 11 and neutron spin of 29/2. The maximum spin as a result of closing of the shears is 51/2. However, as observed experimentally, the band terminates at spin 57/2. The difference of spin is contributed by weakly deformed core rotation through many nucleons with small spins, as $\boldsymbol{I} = \boldsymbol{I}_{\text{shears}} + \boldsymbol{R}_{\text{core}}$. As seen in the level scheme (Fig. 2.4), an irregularity occurs near band termination. Two closely spaced 57/2 states and three 59/2 levels are populated. With the rotational alignment of two $\nu i_{13/2}{}^{-2}$ neutrons, the shears open up to ~90° coupling and a new shears band with $\left[\nu(i_{13/2}{}^{-4} f_{5/2}{}^{-1}) \otimes \pi\left(h_{9/2}\, i_{13/2}\right) 11^-\right]$ starts to build-up. This band again exhausts its spin content at maximum spin of 67/2 by shears closing. The actual maximum spin state observed is at 71/2 due to the core contribution. The core contributions are shown as horizontal arrows at maximum spins in the figure.

The band termination phenomenon in deformed rotational nuclei is in some sense different from that discussed above. For a detailed discussion of the former type of band termination, see ref. 2 under Band Termination on p. 114.

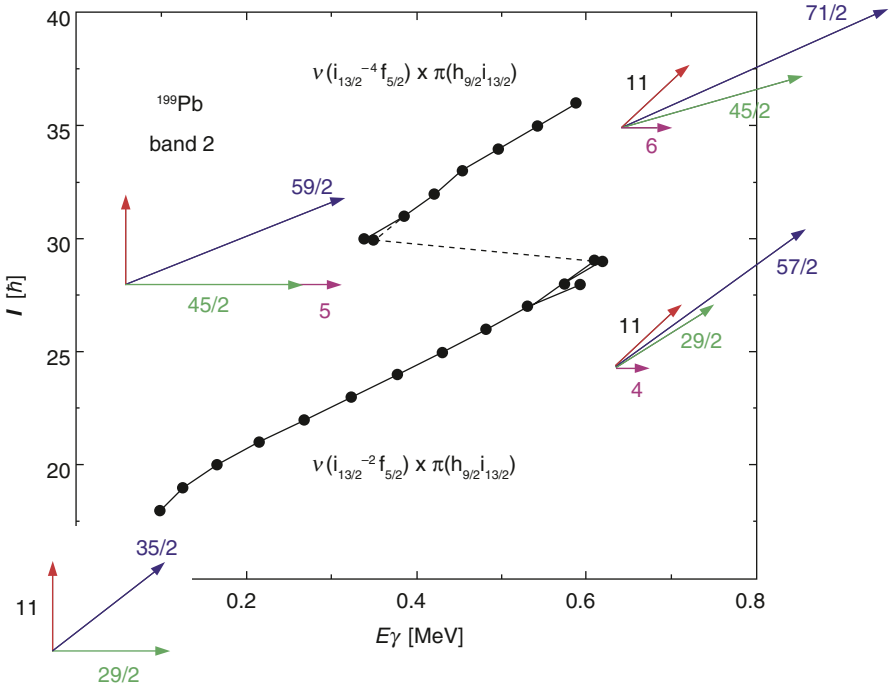

Fig. 2.20 Angular momentum, ***I***, as a function of E_γ for band 2 in ^{199}Pb (see Fig. 2.4 for level scheme). (Figure taken with permission from [11])

2.3 Antimagnetic Rotation

Another type of shears mechanism than the one discussed above was proposed by Frauendorf [59] which he called 'Antimagnetic rotation' (AMR). In this mechanism, two shears—like systems—are formed. Best examples of this are predicted in the light Cd isotopes, although AMR is expected to occur in the same mass regions and under similar conditions as magnetic rotation [57]. Here, two $h_{11/2}$ neutron particles align their spin along the symmetry axis and the two $g_{9/2}$ proton holes are aligned perpendicular to the symmetry axis, but their spins are anti-parallel. Each of the proton holes combines with a neutron particle, thus forming a pair of back to back shears. In contrast to the shears mechanism in magnetic rotation where there is a large component of magnetic dipole moment ($\mu_\perp$) perpendicular to the total angular momentum vector, in these two pair of shears, the perpendicular component of magnetic dipole moment from each pair is equal and opposite, and thus they cancel each other, i.e. $\mu_\perp = 0$. Therefore, the B(M1) values vanish and so no M1 transitions are observed. The magnetic dipole moments of one of the shears specify the orientation. The angular momentum in an antimagnetic rotational band is generated through the simultaneous step-by-step closing of the two shears. Since the

two shears system is symmetric with respect to rotation by π about the total angular momentum axis, the rotational band should consist of sequences of energy levels with $\Delta I = 2\hbar$. The levels in the band should decay by weak E2 gamma-ray transitions as the core has small deformation. The phenomenon of antimagnetic rotation is characterised by a rapid decrease of the B(E2) values with increasing spin.

Experimental investigations on antimagnetic rotation have been done in ^{100}Pd [60] and in $^{106, 108, 109, 110}$Cd [61–65]. In ^{106}Cd [66], lifetimes were measured [61, 62] by the DSAM for excited states between spins 18–26 in the collective band based on 10^+ bandhead state which is a two-quasi-neutron rotation aligned $\nu(h_{11/2})^2$ structure. The partial level scheme of ^{106}Cd [66] is shown in Fig. 2.21 [67]. A further alignment of a pair of $g_{7/2}$ neutrons was observed in this band at a rotational frequency $\hbar\omega \sim 0.45$ MeV. The neutron configuration $\nu[(h_{11/2})^2{}_{10}\ (g_{7/2})^2{}_6]$ was, therefore, assigned to this band above spin of 16. The Cd isotopes with

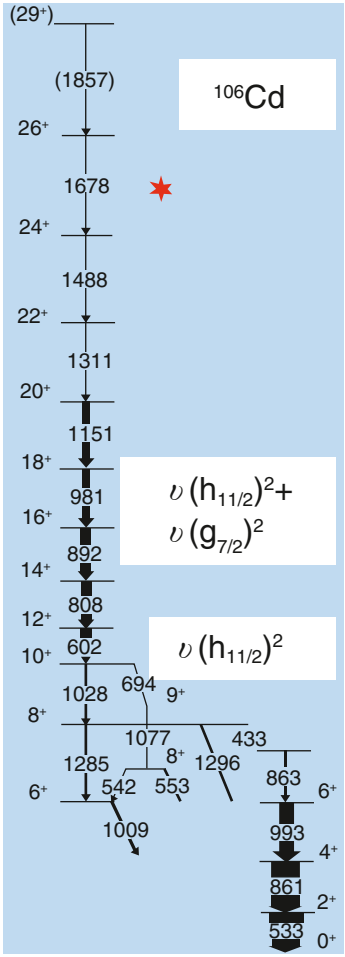

Fig. 2.21 Partial level scheme of ^{106}Cd [66]. (Figure taken with permission from R. Wadsworth NS06 [67])

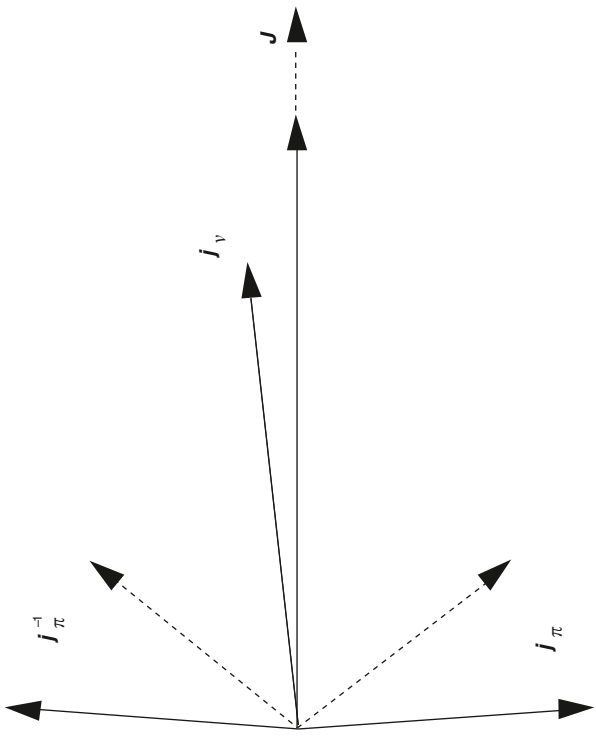

Fig. 2.22 Schematic representation of the shears mechanism and the coupling scheme for antimagnetic rotation. See text for details. (The basic figure taken from [57])

$Z = 48$ have two proton holes in the $g_{9/2}$ orbital. The aligned four quasi-particle neutron configuration is coupled to the two $g_{9/2}$ proton holes. The coupling scheme is represented in Fig. 2.22 [65]. The four aligned quasi-neutrons are denoted by the vector $\boldsymbol{j_\nu}$ and each of the two $g_{9/2}$ proton holes $\pi(g_{9/2})^{-1}$ by $\boldsymbol{j_\pi}^{-1}$. The proton hole angular momentum vectors are antiparallel and nearly perpendicular to the neutron angular momentum vector at spin 16. This system has total $\mu_\perp = 0$ and no M1 transitions are observed. The angular momentum generation above spin 16 in the band is by the shears mechanism. The solid line (dashed line) arrows show the coupling at low (high) rotational frequency. The spin in the band increases from 16 to 26 on complete alignment of the proton–hole spin vectors. Actually, the aligned spin contribution of the pair of proton–holes is $(9/2 + 7/2)\hbar = 8\hbar$, which will make the spin $16\hbar + 8\hbar = 24\hbar$ at band termination. The deformed core contributes an extra $\sim 2\hbar$. The TAC calculations [62] yield $\beta_2 \approx 0.16$ at spin $I \sim 17$ and there is a rapid decrease in β_2 with increase in spin. The β_2 value becomes ~0 around spin 26. The experimental values of B(E2) deduced from the lifetime measurements [62] are plotted in Fig. 2.23 [67] as a function of spin. The B(E2) values decrease rapidly with spin as predicted by theory. This provides evidence for the shears mechanism and thus for the antimagnetic rotation phenomenon. The experimental results are in good agreement with the cranked Nilsson–Strutinsky (CNS), TAC and the semiclassical (SCM) calculations. The arrows in the figure show the rela-

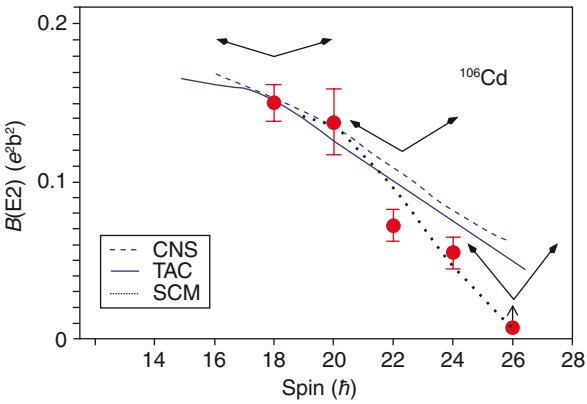

Fig. 2.23 Plot of experimental values of B(E2) as a function of spin [61, 62]. See text for details. (Figure taken with permission in part from R. Wadsworth NS06 [67])

tive orientation of angular momentum of the $g_{9/2}$ proton holes as predicted by the TAC calculations.

The number of investigations in antimagnetic rotation is not very large, and so there is a need to investigate and find more evidence for this new type of shears coupling through the measurement of lifetimes in particular, in this and the other mass regions.

References

1. H. Hübel, Wetherill Symp. (Philadelphia, PA, 1991)
2. H. Hübel et al., *Proc. International School on Nuclear Physics, Erice (1991),* Prog. Part. Nucl. Phys. 28, 427 (1992)
3. G. Baldsiefen et al., Phys. Lett. B 275, 252 (1992)
4. B. Fant et al., J. Phys. G 17, 319 (1991)
5. R. M. Clark et al., Daresbury Rept. 1991/1992
6. R. M. Clark et al., Phys. Lett. B 275, 247 (1992)
7. A. Kuhnert et al., Phys. Rev. C 46, 133 (1992)
8. S. Frauendorf, Nucl. Phys. A 557, 259c (1993)
9. P. Kemnitz et al., Nucl. Phys. A 456, 89 (1986)
10. Sham S., Malik et al., Nucl. Phys. A 732, 13 (2004)
11. H. Hübel, Prog. Part. Nucl. Phys. 54, 1 (2005) and references therein
12. J. Duprat et al., Z. Phys. A 347, 289 (1994)
13. W. Pohler et al., Eur. Phys. J. A 5, 257 (1999)
14. Amita, Ashok Kumar Jain and Balraj Singh, At. Data Nucl. Data Tables, 74, 283 (2000), updated version is available online at http://www.ideallibrary.com
15. R. M. Clark and A. O. Macchiavelli, Ann. Rev. Nucl. Part. Sci. 50, 1 (2000)
16. P. Van Druppen et al., Phys. Rev. Lett. 52, 1974 (1984)
17. P. Van Druppen et al., Phys. Lett. B 154, 354 (1985)
18. J. Penninga et al., Nucl. Phys. A 471, 535 (1987)
19. G. D. Dracoulis et al., Phys. Rev. C 63, 061302(R) (2001)
20. G. D. Dracoulis et al., Phys. Rev. C 72, 064319 (2005)
21. M. Ionescu – Bujor et al., Phys. Lett. B 650, 141 (2007)
22. K. Vyvey et al., Phys. Rev. Lett. 88, 102502 (2002)

23. L. Ducroux et al., Z. Phys. A 356, 241 (1996)
24. G. Baldsiefen et al., Phys. Rev. C 54, 1106 (1996)
25. K. Vyvey et al., Phys. Rev. C 69, 064318 (2004)
26. A. Görgen et al., Nucl. Phys. A 683, 108 (2001)
27. M. Kaci et al., Nucl. Phys. A 697, 3 (2002)
28. A. K. Singh et al., Nucl. Phys. A 707, 3 (2002)
29. M. Kaci et al., Z. Phys. A 354, 267 (1996)
30. G. Baldsiefen et al., Nucl. Phys. A 574, 521 (1994)
31. G. Duchene et al., Nucl. Instrum. Methods. Phys. Res. A 432, 90 (1999)
32. O. Klein, Y. Nishina, Z. Phys. 52, 853 (1929)
33. D. Rossbach et al., Phys. Lett. B 513, 9 (2001)
34. Hager-Seltzer *Internal Conversion Coefficients,* http://www.nndc.bnl.gov
35. S. Chmel et al., Phys. Rev. Lett. 79, 2002 (1997)
36. H. Hübel, Fortschr. Phys. 25, 327 (1977)
37. D. L. Balabanski et al., Eur. Phys. J. A 20, 191 (2004)
38. M. Ionescu – Bujor et al., Phys. Rev. C 70, 034305 (2004)
39. S. Zywietz et al., Hyperfine Intr. 9, 109 (1981)
40. H. Ejiri and M. J. A. de Voigt, *Gamma Ray and Electron Spectroscopy in Nuclear Physics* (Oxford Univ. Press, Oxford 1987) p.504
41. G. B. Hagemann et al., Nucl. Phys. A 424, 365 (1984)
42. R. M. Clark et al., Phys. Rev. Lett. 78, 1868 (1997)
43. R. M. Clark et al., Phys. Lett. B 440, 251 (1998)
44. R. Krücken et al., Phys. Rev. C 58, R 1876 (1998)
45. G. Kemper et al., Eur. Phys. J. A 11, 121 (2001)
46. J. R. Cooper et al., Phys. Rev. Lett. 87, 132503 (2001)
47. A. K. Singh et al., Phys. Rev. C 66, 064314 (2002)
48. S. Chmel et al., Phys. Rev. C 75, 044309 (2007)
49. D. A. Torres et al., Phys. Rev. C 78, 054318 (2008)
50. S. Frauendorf et al., Nucl. Phys. A 601, 41 (1996)
51. A. O. Macchiavelli et al., Phys. Rev. C 57, R1073 (1998)
52. A. O. Macchiavelli et al., Phys. Rev. C 58, R621 (1998)
53. A. O. Macchiavelli et al., Phys. Rev. C 58, 3746 (1998)
54. A. O. Macchiavelli et al., Phys. Lett. B 450, 1 (1999)
55. Amita et al., PRAMANA, 53, 463 (1999)
56. B. G. Carlsson and I. Ragnarsson, Phys. Rev. C 74, 044310 (2006)
57. S. Frauendorf, Rev. Mod. Phys. 73, 463 (2001)
58. S. Frauendorf, Nucl. Phys. A 677, 115 (2000)
59. S. Frauendorf in *Proceedings of the Workshop on Gammasphere Physics, Berkeley* (World Scientific, Singapore 1995) p. 272
60. S. Zhu et al., Phys. Rev. C 64, 041302 (R)(2001)
61. A. J. Simons et al., Phys. Rev. Lett. 91, 162501 (2003)
62. A. J. Simons et al., Phys. Rev. C 72, 024318 (2005)
63. P. Datta et al., Phys. Rev. C 71, 041305 (R) (2005)
64. C. J. Chiara et al., Phys. Rev. C 61, 034318 (2000)
65. R. Wadsworth and R. M. Clark, priv comm. (1998)
66. P. H. Regan et al., Nucl. Phys. A 586, 351 (1995)
67. R. Wadsworth in *Nuclear Structure 06, ORNL*

Chapter 3
Triaxial Strong Deformation and Wobbling Motion

3.1 Introduction

In this chapter, we will consider the rotational motion in triaxial quadrupole deformed nuclei. The quest to establish stable triaxial shapes in nuclei is being pursued with keen interest during the last about half-a-century. In the initial phases for it, the structures of energy levels at relatively low angular momenta were considered. Generally, the deviations from axially symmetric shape are expected at high spins [1] since the rotational effects are strong for high-j orbitals. The loss of axial symmetry affects a number of observables. For a nucleus having a stable triaxial shape, different moments of inertia are associated with each of the principal axes and the rotational motion is possible about all the three axes. Therefore, the rotational spectra are expected to be richer for stable triaxial nuclei as compared to that for axially symmetric deformed nuclei. Experimentally, it is difficult to find a unique evidence for the stable triaxial shapes. However, triaxial shape has been invoked to explain a number of observed phenomena in the mass $A \sim 160$ region, like, signature dependence of $B(E2; I \rightarrow I-1)$ values in odd-A nuclei, anomalous signature splittings and signature inversions in odd–odd nuclei [2]. Wobbling motion [1] and Chirality [3] are the phenomena which are uniquely associated with stable triaxial shapes in nuclei. The former is discussed in this chapter and the latter in the next (Chap. 4).

A number of excellent review articles on triaxiality and wobbling motion in nuclei exist in the literature, see, e.g. [4–6].

3.2 Triaxial Strong Deformation

Potential energy surface calculations [7, 8] for nuclei with $Z \sim 71$ and $N \sim 92$–97 predict that these nuclei constitute a new region of exotic nuclear shapes. Systematic total energy surface calculations [9] using the Ultimate Cranker (UC) code [10–12] based on a cranked modified harmonic oscillator potential revealed triaxial strongly deformed (TSD) minima with $(\varepsilon_2, \gamma) \sim (0.40, \pm 20°)$ at high spins for the above-mentioned nuclei, coexisting with axially symmetric normal deformed

S. C. Pancholi, *Exotic Nuclear Excitations,* Springer Tracts in Modern Physics 242,
DOI 10.1007/978-1-4419-8038-0_3, © Springer Science+Business Media, LLC 2011

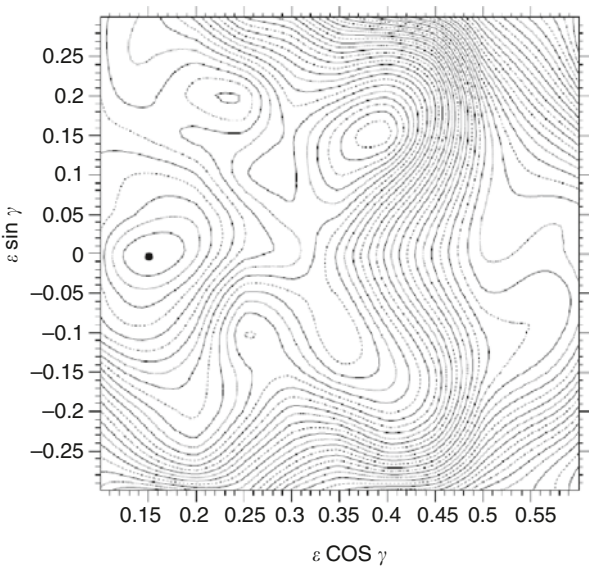

Fig. 3.1 Total energy surface for ^{161}Lu calculated [13] using the UC code for parity and signature $(\pi, \alpha)=(+, +1/2)$ at spin $I=61/2\hbar$. Besides the normal minimum $(\varepsilon_2, \gamma)=(\sim 0.15, 0°)$, local TSD minima with $(\varepsilon_2, \gamma)\sim(0.4, 20°)$ is predicted in the calculations. The energy difference between contour lines is 0.2 MeV. (Figure taken with permission from [13])

(ND) prolate nuclear structures with $(\varepsilon_2, \gamma)\sim(0.23, 0°)$. Here, γ is the triaxiality parameter. These calculations also show that these TSD minima are expected for all four combinations of parity π and signature α. As examples, Figs. 3.1, 3.2, 3.3 and 3.4 [13–16] show the results of the total energy surfaces at high spins calculated with the UC code for ^{161}Lu, ^{163}Lu, ^{165}Lu and ^{167}Lu respectively. In all these four figures, minima at normal deformation with $(\varepsilon_2, \gamma)\sim(\sim 0.2, 0°)$ are clearly seen.

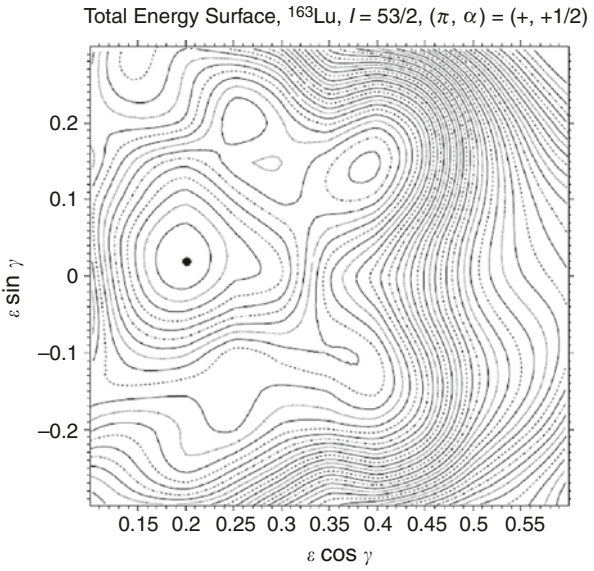

Fig. 3.2 Total energy surface for ^{163}Lu with $(\pi, \alpha)=(+, +1/2)$ at spin $I=53/2\hbar$ calculated [14] using the UC code. The normal deformed (ND) minimum at $(\varepsilon_2, \gamma)=(\sim 0.2, 0°)$ with local minimum at $(\varepsilon_2, \gamma)\sim(0.4, +20°)$ are clearly seen in the figure. At spin $I=53/2\hbar$ the other local minimum $(\varepsilon_2, \gamma)\sim(0.4, -20°)$ is poorly developed. (Figure reproduced with permission from [14])

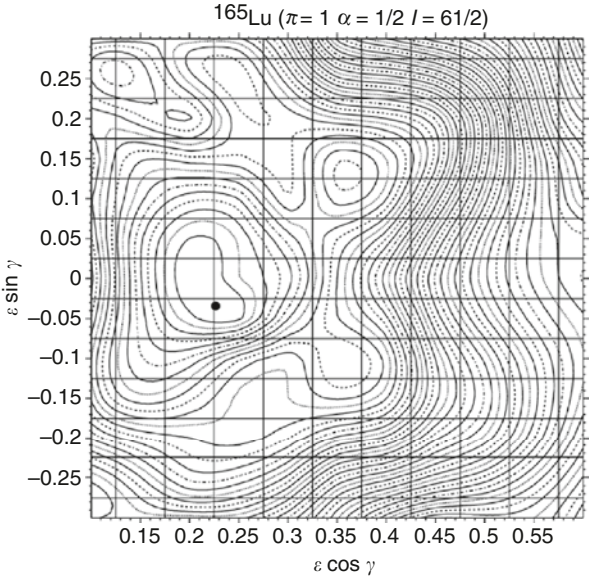

Fig. 3.3 Total energy surface for ^{165}Lu at spin $I=61/2\hbar$ calculated [15] with the UC code. The ND minimum at $(\varepsilon_2, \gamma)=(\sim 0.23, 0°)$ and two local minima at $(\varepsilon_2, \gamma)\sim(0.38, \pm 20°)$ are seen in the figure. The local minimum with $\gamma\sim+20°$ is deeper than the one with $\gamma\sim-20°$. (Figure reproduced with permission from [15])

Of particular interest and importance is the prediction of local minima at triaxial deformation with $(\varepsilon_2, \gamma)\sim(0.4, \pm 20°)$. At high spins in these Lu nuclei, the TSD energy minima with $\gamma>0°$ are always energetically favoured as compared to those with $\gamma<0°$. It should be mentioned here that TSD minima appear in the total energy surface calculations from spin $I=10\hbar$ in some nuclei to all the way up to spin $I=50\hbar$ and higher.

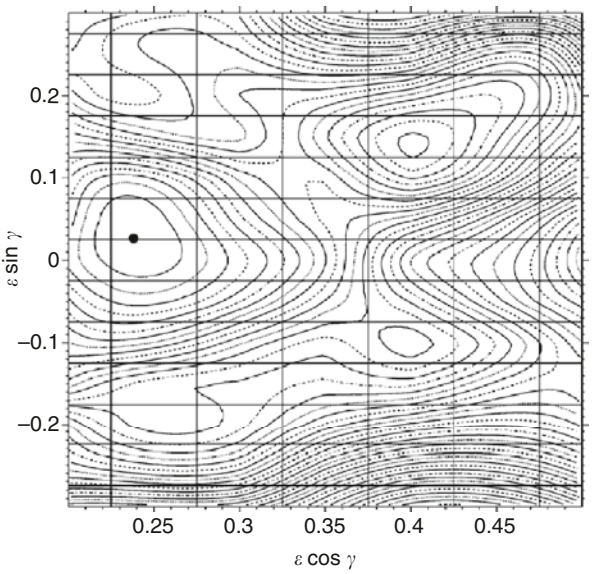

Fig. 3.4 The total energy surface for ^{167}Lu at spin $I=97/2\hbar$ for $(\pi, \alpha)=(+, +1/2)$ calculated [16] with the UC code. The ND minimum $(\varepsilon_2, \gamma)=(\sim 0.25, 0°)$ and two local minima at $(\varepsilon_2, \gamma)\sim(0.43, \pm 20°)$ are clearly seen in the figure. (Figure reproduced with permission from [16])

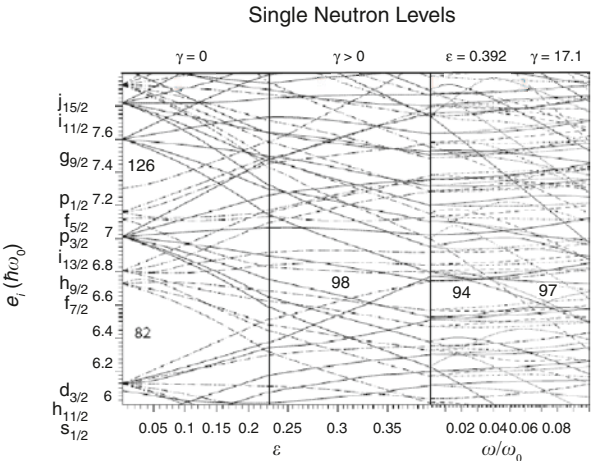

Fig. 3.5 Calculated [17] single particle energy levels for neutrons in the ^{163}Lu and ^{165}Lu region. See text for details. (Figure reproduced with permission from [17])

The TSD minima, mentioned above, are caused by the large single particle shell gaps associated with proton number $Z \sim 71$ and particularly neutron numbers $N=94$ and 97 at large deformation with substantial triaxiality at high spins. The single particle energy level diagrams for neutrons and protons in the ^{163}Lu and ^{165}Lu have been calculated in [17] and shown in Fig. 3.5 (for neutrons) and Fig. 3.6 (for protons). For a detailed description of these diagrams, see [17]. Figure 3.5 consists of three sections: (1) the left section shows the single particle levels at axially symmetric prolate shape ($\gamma=0°$) and from $\varepsilon=0$ (spherical) to $\varepsilon=0.232$ (ND), (2) the middle section shows the single particle levels along the path through the (ε, γ) plane from (0.23, 0°) to (0.392, 17.1°) for $\gamma>0$ and (3) the right section shows the single particle levels at (ε, γ)=(0.392, 17.1°) with an increase of rotational frequency. The Y-axis energy scale and the rotational frequency are given in units of oscillator

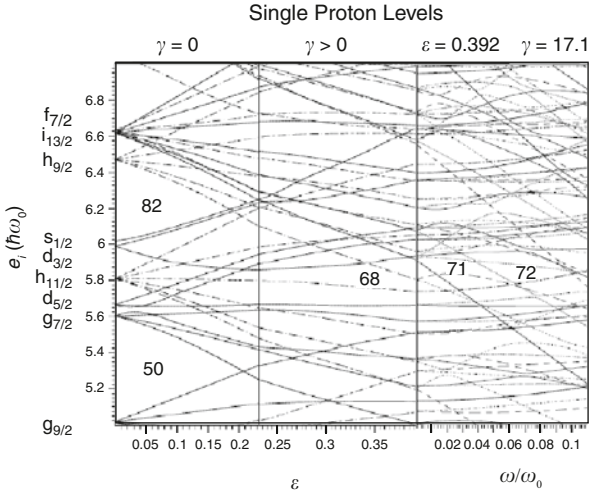

Fig. 3.6 Calculated [17] single particle energy level diagrams for protons for the ^{163}Lu and ^{165}Lu region. The three sections in the figure are analogous to that in Fig. 3.5 and explained in the text. (Figure reproduced with permission from [17])

frequency, $\hbar\omega_0$. At triaxial deformed shapes (third section on the right in the figure), a large shell gap appears at neutron number 94. This is ~35% of the spherical shell gap at $N=82$ at rotational frequencies of up to $\sim\omega/\omega_0=0.03$ ($\hbar\omega\approx0.24$ MeV). This sizable gap at $N=94$ should certainly be responsible for the appearance of TSD states. In the rotational frequency region $\omega/\omega_0\sim0.04$, this shell gap is penetrated by highly alignable intruder levels from above (like one $j_{15/2}$ level, $i_{13/2}$ components etc.). At $\omega/\omega_0\approx0.065$ ($\omega\approx0.52$ MeV), this gap at $N=94$ is completely closed. It should be mentioned here that the positions of the intruder levels are not known very well. Therefore, the closing of the gap at a certain angular momentum cannot be precisely predicted. At higher rotational frequencies a moderately sized shell gap opens up at neutron number $N=97$.

Figure 3.6 shows the calculated [17] single proton level diagrams for the ^{163}Lu and ^{165}Lu region. The three sections in the figure are analogous to that in Fig. 3.5. At the TSD shapes (section three right side), at first sight it appears that there is no major shell gap at $Z=71$ or 72. However, a closer look reveals that in this Z-region, the level density in the rotational, single proton spectrum is relatively low. Also, the calculations [17] predict that shape driving two intruder levels from the $i_{13/2}$ sub-shell will fall inside the gap region. But the exact positions of the intruder levels are not known. Therefore, a most favourable proton number cannot be predicted precisely.

3.3 Triaxiality and Wobbling Motion

Nuclei in general possess shapes which are axially symmetric, where, considering the three principal axes, collective rotations about any of the two axes are equivalent since the moments of inertia about these axes are equal. Rotation about the third axis (symmetry axis) is not allowed quantum mechanically. If a nucleus has a stable triaxial shape, collective rotations of such a nucleus are possible about all the three axes involving three associated unequal moments of inertia ($\Im_x>\Im_y\neq\Im_z$). Although, the triaxial nucleus favours rotation about the axis with the largest moment of inertia on energy considerations, contributions from rotations about the other two axes can disturb this rotational motion and force the rotational angular momentum vector (**R**) off the principal axis. This results in precession and wobbling motion. The classical analogue of wobbling motion is the rotation of an asymmetric top. Wobbling motion, therefore, is uniquely related to the stable triaxial shape.

The wobbling motion of a triaxial even–even nucleus was first predicted by Bohr and Mottelson [1] using the macroscopic rotor model. This motion gives rise to a sequence of wobbling bands. In the high-spin limit ($I>>1\hbar$), and neglecting the intrinsic structure, the energy of the wobbling bands can be separated into rotation about the principal axis and the wobbling motion

$$E_R(I,n_W)=\frac{I(I+1)\hbar^2}{2\Im_x}+\hbar\omega_W\left(n_W+\frac{1}{2}\right) \tag{3.1}$$

where it is assumed that $\Im_x$ is the largest moment of inertia and that the main rotation occurs around the x-axis. n_w is the wobbling phonon number, $\hbar\omega_w$ and $\hbar\omega_{\rm rot}$ are the wobbling and rotational frequencies, respectively. These are given by the following expressions:

$$\hbar\omega_w = \hbar\omega_{\rm rot}\sqrt{\frac{(\Im_x - \Im_y)(\Im_x - \Im_z)}{\Im_y \Im_z}} \tag{3.2}$$

and

$$\hbar\omega_{\rm rot} = \frac{I\hbar^2}{\Im_x}. \tag{3.3}$$

Each of the wobbling bands is characterised by the integers n_w=0, 1, 2,…. These bands are based on the same intrinsic nuclear structure. The band with n_w=0 is the Yrast band. The excitation energy of the wobbling bands increases with increasing phonon number n_w.

In [18], the wobbling motion was investigated from the microscopic view point.

It was realised later that in odd-A nuclei, the presence of high-j aligned particles can play a crucial role in wobbling motion. These aligned particles will favour a specific (triaxial) shape depending on the degree of shell filling in the high-j subshell and states with high-j aligned particles may appear close to the Yrast line because of the relatively small rotational energy needed to build up a certain total angular momentum in the nucleus. A number of authors [19–22] developed the theory of wobbling motion pointing out the role of the rotation aligned high-j ($i_{13/2}$) quasi-proton, in terms of the particle-rotor model and the cranked shell model plus random phase approximation approach. Another theoretical attempt based on an algebraic description of the TSD bands in odd-A nuclei has been made in [23].

Following [6, 21], for the case of an aligned high-j particle which is coupled to a triaxial rotor, the energy equation Eq. 3.1 can be re-written as

$$E_R(I, n_w, j) = \frac{I(I+1)\hbar^2}{2\Im_x} + \hbar\omega_W\left(n_W + \frac{1}{2}\right) + \frac{\hbar^2}{2\Im_x}\left(-2I_x j_x + j_x^2\right). \tag{3.4}$$

The energy difference between wobbling bands with Δn_w=1,

$$\Delta E(I, j) = \hbar\omega_W + 2j_x\frac{\hbar^2}{2\Im_x} \tag{3.5}$$

is larger than in the case of no-aligned angular momentum.

According to the particle-rotor model calculations [19], a characteristic fingerprint of the wobbling motion in such nuclei is the occurrence of ΔI=±1$\hbar$ interband transitions, (n_w=i)→(n_w=i−1) with i 1, 2 possessing large values of $B(E2)_{\rm out}$, in competition with $B(E2)_{\rm in}$ of the in-band ΔI=2$\hbar$ transitions. The quantal phonon

rule for transition probability implies that $B(E2, n_w=2 \rightarrow n_w=1) \sim 2$. $B(E2, n_w=1 \rightarrow n_w=0)$ and the values of $B(E2, n_w=2 \rightarrow n_w=0)$ for transitions $n_w=2 \rightarrow n_w=0$ are small and only non-zero due to anharmonicity in the quanta phonon description.

3.4 Experimental Results—Even-N Lu Isotopes

A number of experimental investigations [13–16, 20, 24–41] of high-spin states in even-N $^{161, 163, 165, 167}$Lu nuclei have been done recently using mainly the EUROBALL, GAMMASPHERE and the GaSp arrays. Out of these nuclei, the best studied is ^{163}Lu [14, 20, 26–36]. A high-spin decoupled rotational band observed in this nucleus was assigned to be built on the strongly deformation driving $\pi i_{13/2}$ $[660]1/2^+$ intruder orbital [26, 27]. The OSIRIS gamma-detector array consisting of 12 Compton suppressed Ge detectors with an inner ball of 48 BGO detectors was used in the above investigations. Subsequent studies in ^{163}Lu revealed the existence of four high-spin rotational bands including that observed in [26], up to $J=97/2$ [36 and references therein]. In Fig. 3.7, the partial level scheme of ^{163}Lu [36] shows these bands designated as TSD1, TSD2, TSD3 and TSD4 together with the interconnecting gamma-ray transitions to the ND band structures $[523]7/2-$ and $[411]1/2^+$ to which the TSD bands decay. The population intensities of TSD1, TSD2, TSD3 and TSD4 are ~10%, 3%, 1.2% and 0.9% [36], respectively of the reaction channel. Ten interconnecting $\Delta I=1$ gamma-ray transitions ranging in energy from 564 to 716 keV were found between TSD2 to TSD1. Four $\Delta I=1$ gamma-ray transitions (377–476 keV) connect TSD3 to TSD2 and eight high energy (963–1297 keV) $\Delta I=2$ gamma-ray transitions are observed from TSD3 to TSD1. The TSD4 band decays to TSD1 by four weakly populated high-energy gamma-ray transitions and has been assigned as a three-quasiparticle band [36].

The spins and parities of TSD1 were determined on the basis of multipolarity assignments from the DCO ratios of the interconnecting decay out gamma-ray transitions from TSD1 to ND states and the bandhead spin and parity of TSD1 to be $J^\pi=13/2^+$ as expected for a band based on $\pi i_{13/2}$ $[660]1/2^+$ configuration [29]. The spins and parities of the other TSD bands, TSD2 and TSD3 were assigned [20, 30, 33] from the determination of multipolarity and multipole character of the interconnecting gamma-ray transitions from TSD2 and TSD3 to TSD1 and from TSD3 to TSD2, from the analysis of the DCO ratios, angular distribution ratios as well as linear polarization measurements for the strong transitions. The data are consistent with mixed $M1/E2$ multipolarity for the TSD2 to TSD1 transitions. The mixing ratios δ determined for these transitions showed no-spin dependence within errors. The δ values for the different interconnecting transitions were therefore combined and averaged. The result so obtained is $\delta=-3.10^{+0.36}_{-0.44}$ or $-0.22^{+0.05}_{-0.03}$ [20]. The linear polarisation measurements for these gamma-ray transitions show their electric character, with the same sign and magnitude as the stretched $E2$ TSD in-band transitions, thus excluding the latter solution $\delta=-0.22^{+0.05}_{-0.03}$. The final result

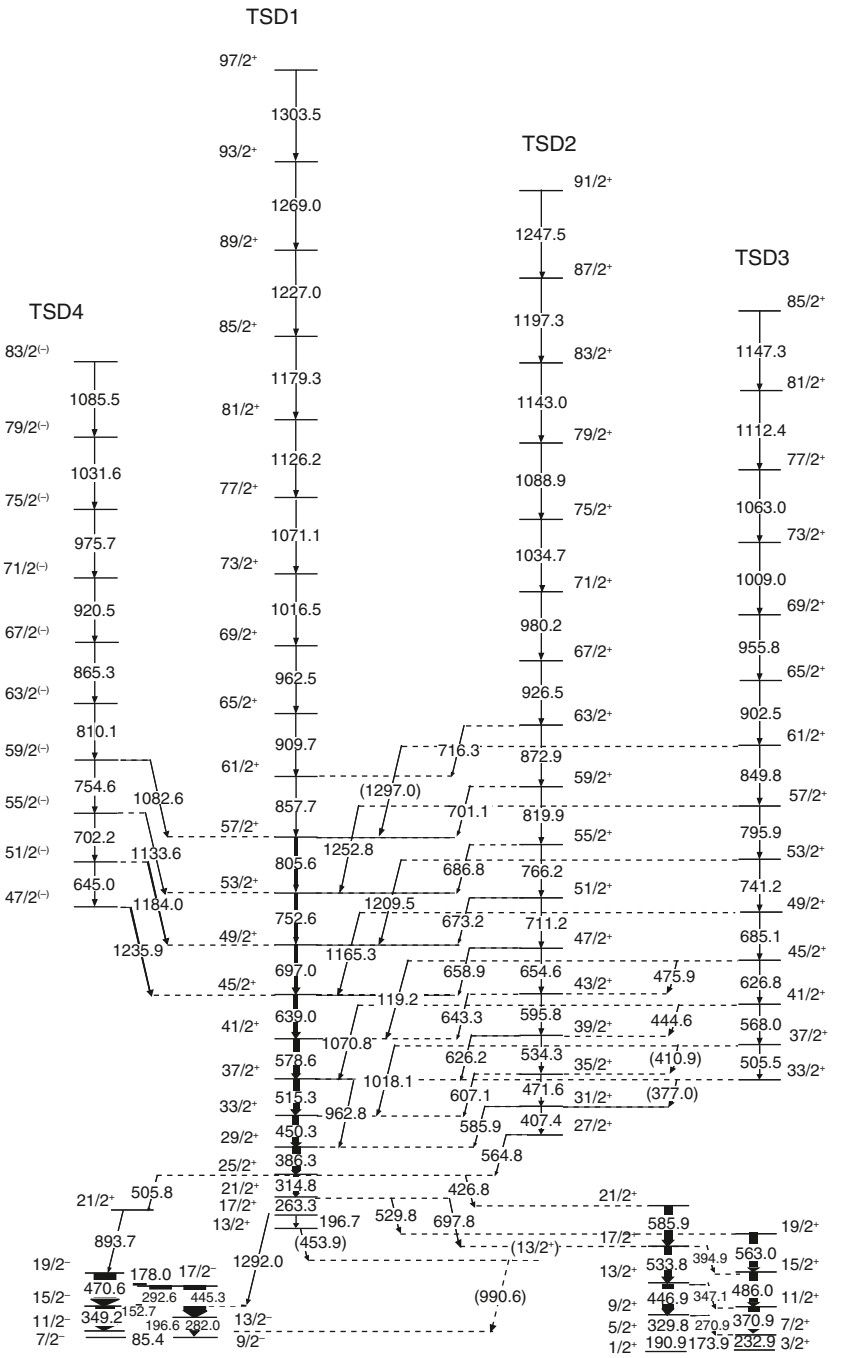

Fig. 3.7 Partial level scheme of ^{163}Lu [36]. (Figure reproduced with permission from [36])

with $\delta = -3.10^{+0.36}_{-0.44}$ corresponds to (90.6 ± 1.3)% $E2$ and (9.4 ± 1.3)% $M1$ in these transitions [20]. For the interconnecting gamma-ray transitions between TSD3 to TSD2, the angular distribution and the DCO ratios could only be measured for the stronger 476 keV transition. The mixing ratio obtained for this transition is $\delta = -3.60^{+0.97}_{-1.93}$ or $-0.19^{+0.08}_{-0.12}$ [33]. No linear polarisation analysis was possible for this gamma-ray transition due to low statistics [33]. Although the former mixing ratio value is in agreement with the value obtained for TSD2 to TSD1 interconnecting transitions, the selection of one of the above two experimental δ values, therefore, could not be made on experimental basis.

Since, as will be shown later, bands TSD1 and TSD2 have similar intrinsic structure, most likely mixing ratio value for the 476 keV TSD2 to TSD1 interconnecting transition is $\delta = -3.60^{+0.97}_{-1.93}$. This corresponds to $\left(92.8^{+4.0}_{-5.5}\right)\%$ $E2$ and $\left(7.2^{+5.5}_{-4.0}\right)\%$ $M1$ in this transition [33]. The stretched $E2$ character has been assigned to the high-energy $\Delta I = 2$ gamma-ray transitions from TSD3 to TSD1 from the analysis of angular distribution and DCO ratio measurements [20]. Although the linear polarisation measurements have quite large errors, the results agree with the stretched $E2$ assignment for these transitions [20].

The experimental reduced transition probability $B(E2)_{\text{out}}$, i.e. for the $E2$ + ($M1$) interconnecting gamma-ray transition from a level in TSD2 to TSD1, can be determined relative to in-band TSD2 $B(E2)_{\text{in}}$ for the $E2$ gamma-ray transition de-exciting the same TSD2 level from the branching ratio $\lambda = T_{\gamma,\text{out}}[E2 + (M1)]/T_{\gamma,\text{in}}(E2)$, the adopted mixing ratio of $\delta = -3.10^{+0.36}_{-0.44}$ for the TSD2 to TSD1 gamma-ray transition and the gamma-ray energies $E_\gamma(I \rightarrow I-2)_{\text{in}}$ and $E_\gamma(I \rightarrow I-1)_{\text{out}}$ using the following relation:

$$\frac{B(E2, I \rightarrow I-1)_{\text{out}}}{B(E2 \rightarrow I-2)_{\text{in}}} = \frac{\lambda\delta^2}{1+\delta^2} \cdot \frac{E_\gamma^5(I \rightarrow I-2)_{\text{in}}}{E_\gamma^5(I \rightarrow I-1)_{\text{out}}}. \tag{3.6}$$

The values for $B(E2)_{\text{out}}/B(E2)_{\text{in}}$ for these transitions in ^{163}Lu are shown in Table 3.1 [14].

Table 3.1 $B(E2)_{\text{out}}/B(E2)_{\text{in}}$ values for gamma-ray transitions from TSD2 to TSD1 in ^{163}Lu [14]

TSD2 Level I ($\hbar$)	$E_\gamma(I \rightarrow I-1)_{\text{out}}$ (keV)	$E_\gamma(I \rightarrow I-2)_{\text{in}}$ (keV)	$B(E2)_{\text{out}}/B(E2)_{\text{in}}$
35/2	607.1	471.6	0.21 ± 0.02
39/2	626.2	534.3	0.20 ± 0.02
43/2	643.3	595.8	0.22 ± 0.02
47/2	658.9	654.6	0.21 ± 0.02
51/2	673.2	711.2	0.30 ± 0.10

Table 3.2 The $B(E2)_{out}/B(E2)_{in}$ values for gamma-ray transitions from TSD3 to TSD1 in ^{163}Lu [33]

TSD3 Level I ($\hbar$)	$E_\gamma(I \to I-2)_{out}$ (keV)	$E_\gamma(I \to I-2)_{in}$ (keV)	$B(E2)_{out}/B(E2)_{in}$
37/2	1018.1	505.5	0.021 ± 0.004
41/2	1070.8	568.0	0.022 ± 0.003
45/2	1119.2	626.8	0.018 ± 0.003
49/2	1165.3	685.1	0.017 ± 0.004
53/2	1209.5	741.2	0.022 ± 0.005
57/2	1252.8	795.9	0.020 ± 0.005

Similarly, the $B(E2)_{out}/B(E2)_{in}$ value for the 476 keV $[E2+(M1)]$ gamma-ray transition from the 45/2 level of TSD3 to 43/2 level in TSD2 was obtained from the measured branching ratio and the adopted mixing ratio $\delta = -3.60^{+0.97}_{-1.93}$, as $B(E2)_{out}/B(E2)_{in} = 0.51 \pm 0.13$ [33].

The $B(E2)_{out}/B(E2)_{in}$ values for gamma-ray transitions from TSD3 to TSD1 in ^{163}Lu,as obtained in [33] are given in Table 3.2.

In the experimental spectroscopic investigations of the high-spin structure in ^{165}Lu [15, 28, 37], a number of TSD bands have been found. The partial level scheme of ^{165}Lu [37] is shown in Fig. 3.8. Comparing the level scheme of ^{165}Lu (Fig. 3.8) with that of ^{163}Lu (Fig. 3.7), one finds that the TSD bands, Yrast TSD1, TSD2 and TSD3 are similar in these two nuclei with close-lying $E2$ in-band transition energies except that TSD1 in ^{165}Lu is observed only down up to $J=25/2$, TSD2 to 35/2 and TSD3 to 41/2. The interconnecting gamma-ray transitions between TSD2 to TSD1 in ^{165}Lu are from $J=35/2$ to 55/2 and those in ^{163}Lu from $J=27/2$ to 63/2 and the corresponding gamma-ray energies are in the similar energy range. The TSD bands TSD1, TSD2 and TSD3 in ^{165}Lu are much weaker than in ^{163}Lu, having intensities of ~1.3%, 0.4% and 0.1% [15], respectively of the total $4n$ reaction channel. The multipolarity of the in-band transitions of TSD bands in ^{165}Lu have been assigned as $E2$ from the measured DCO ratios [37]. Angular correlation analysis of two of the six interconnecting transitions from TSD2 to TSD1 in ^{165}Lu, the 668 and 682 keV transitions were determined in [15] which are compatible with mixed $\Delta I = 1$ transitions, gave the multipole mixing percentages for the $E2$ and $M1$ multipoles as $92.3^{+5.3}_{-11.2}$ % $E2$ and $7.7^{+11.2}_{-5.3}$ % $M1$ [15]. The other two solutions which give almost reverse percentages of $E2$ and $M1$ multipoles in the transitions have been excluded in analogy with that in ^{163}Lu. The $B(E2)_{out}/B(E2)_{in}$ ratios obtained from the measured branching ratios and the adopted multipole mixing ratios for some of the interconnecting gamma-ray transitions from TSD2 to TSD1 in ^{165}Lu [15] are given below in Table 3.3 [15].

These $B(E2)_{out}/B(E2)_{in}$ values in ^{165}Lu are similar to those found in ^{163}Lu (see Table 3.1) and are large.

The spins, parities and the excitation energy of the TSD band TSD1 were determined form the multipolarity obtained from the DCO measurement of the 591 keV

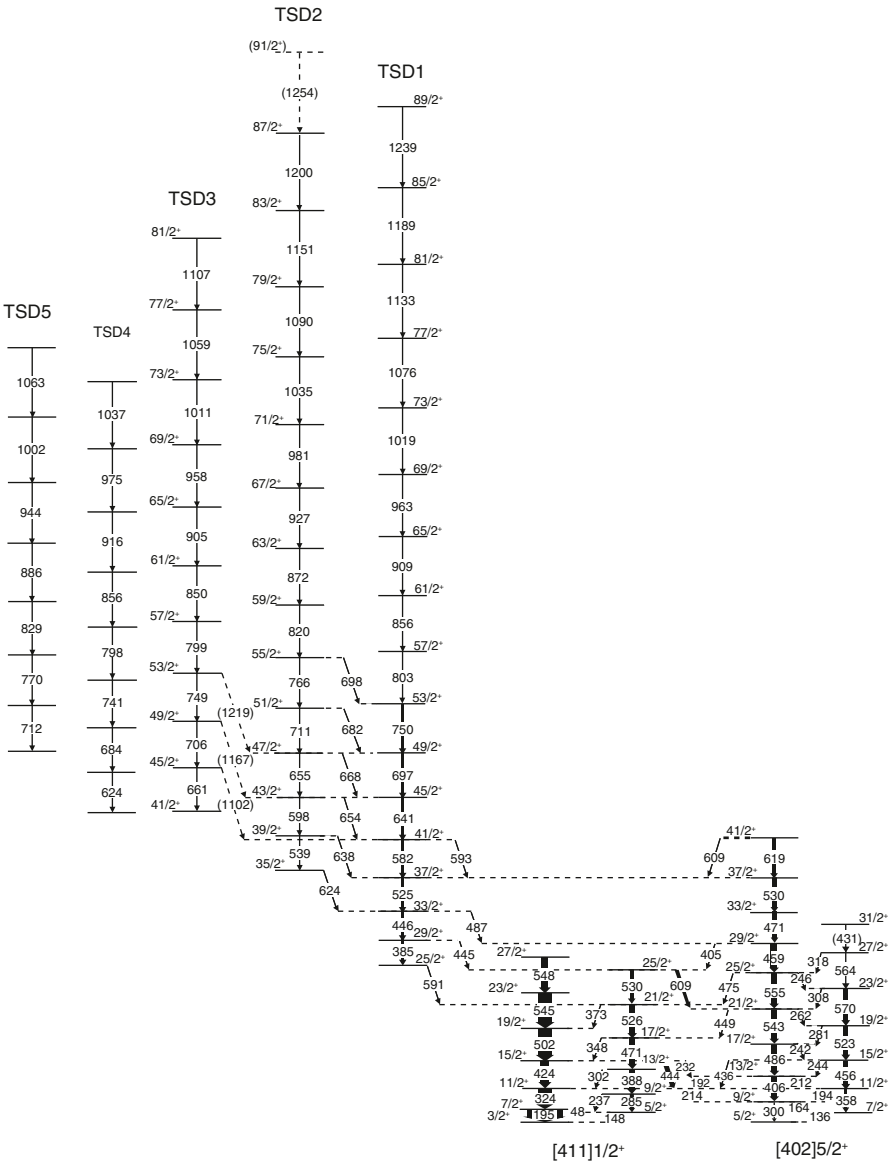

Fig. 3.8 Partial level scheme of ^{165}Lu [37]. (Figure reproduced with permission from [37])

gamma-ray transition [15] linking this band to the [411]1/2+ ND band. The other TSD1 to ND linking transitions are of 445, 487 and 593 keV.

A number of TSD bands were also found in the high-spin spectroscopic investigations of ^{167}Lu [16, 38–41]. A partial level scheme of ^{167}Lu [40] is shown in Fig. 3.9. The population intensities of the bands TSD1, TSD2 and TSD3 relative

Table 3.3 $B(E2)_{out}/B(E2)_{in}$ values for gamma-ray transitions from TSD2 to TSD1 in ^{165}Lu [15]

TSD2 Level I ($\hbar$)	$E_\gamma(I \to I-1)_{out}$ (keV)	$E_\gamma(I \to I-2)_{in}$ (keV)	$B(E2)_{out}/B(E2)_{in}$
39/2	638	539	0.17 ± 0.05
43/2	654	598	0.16 ± 0.03
47/2	668	655	0.22 ± 0.08

Table 3.4 The reduced transition probability ratios $B(E2)_{out}/B(E2)_{in}$ and mixing ratios δ for the gamma-ray transitions interconnecting TSD2 to TSD1 in ^{167}Lu [16]

TSD2 Level I ($\hbar$)	$E_\gamma(I \to I-1)_{out}$ (keV)	δ of $E_\gamma(I \to I-1)_{out}$	$E_\gamma(I \to I-2)_{in}$ (keV)	$B(E2)_{out}/B(E2)_{in}$
39/2	706.1	$-3.1^{+1.1}_{-3.4}$	547	$0.23^{+0.02}_{-0.05}$
43/2	704.2	–	605	–
47/2	707.7	$\left(-5.1^{+1.6}_{-2.5}\right)^{a}$	658	$0.26^{+0.03}_{-0.04}$
51/2	716.9	$-3.9^{+2.7}_{-8.4}$	711	$0.27^{+0.07}_{-0.10}$
55/2	730.3	–	765	–

[a] Average value from DCO analysis and angular distribution ratio [16]

to Yrast are ~8%, ~2% and ~4%, respectively [16, 40]. Six interconnecting $\Delta I = 1$ gamma-ray transitions of $E_\gamma \sim 700$ keV decay from level spin region 35/2 to 55/2 of TSD2 to TSD1. The spins, parities and the excitation energies of TSD1 and TSD2 were determined from multipolarities of the several decay out gamma-ray transitions from TSD1 to ND structures and of the interconnecting $\Delta I = 1$ gamma-ray transitions from TSD2 to TSD1 [16, 40]. In addition to the multipolarity determinations from DCO ratios and angular correlation ratios, K-shell internal conversion coefficients (α_K) were determined [41] for several of the in band gamma-ray transitions in the TSD1 band using the normalised gamma-ray and conversion electron intensity measurement method. The GAMMASPHERE was used for the measurement of gamma-ray intensities and the internal conversion electron intensities were measured using the Internal Conversion Electron Spectrometer (ICE Ball) consisting of six mini-orange electron spectrometers [42]. Comparison of the experimental α_K values with the corresponding theoretical values for pure multipole transitions yield that these in-band gamma-ray transitions in TSD1 are of $E2$ character [41].

The reduced transition probability ratios $B(E2)_{out}/B(E2)_{in}$ for the gamma-ray transitions interconnecting TSD2 to TSD1 in ^{167}Lu were determined from the experimental branching ratios and the mixing ratios obtained from the angular correlation analysis [16] and are given in Table 3.4 [16].

As can be inferred from Table 3.4, the $B(E2)_{out}/B(E2)_{in}$ ratios for the TSD2 to TSD1 interconnecting gamma-ray transitions in ^{167}Lu are also similar in magnitude to those obtained for the interconnecting transitions from TSD2 to TSD1 in ^{163}Lu and ^{165}Lu (see Tables 3.1 and 3.3).

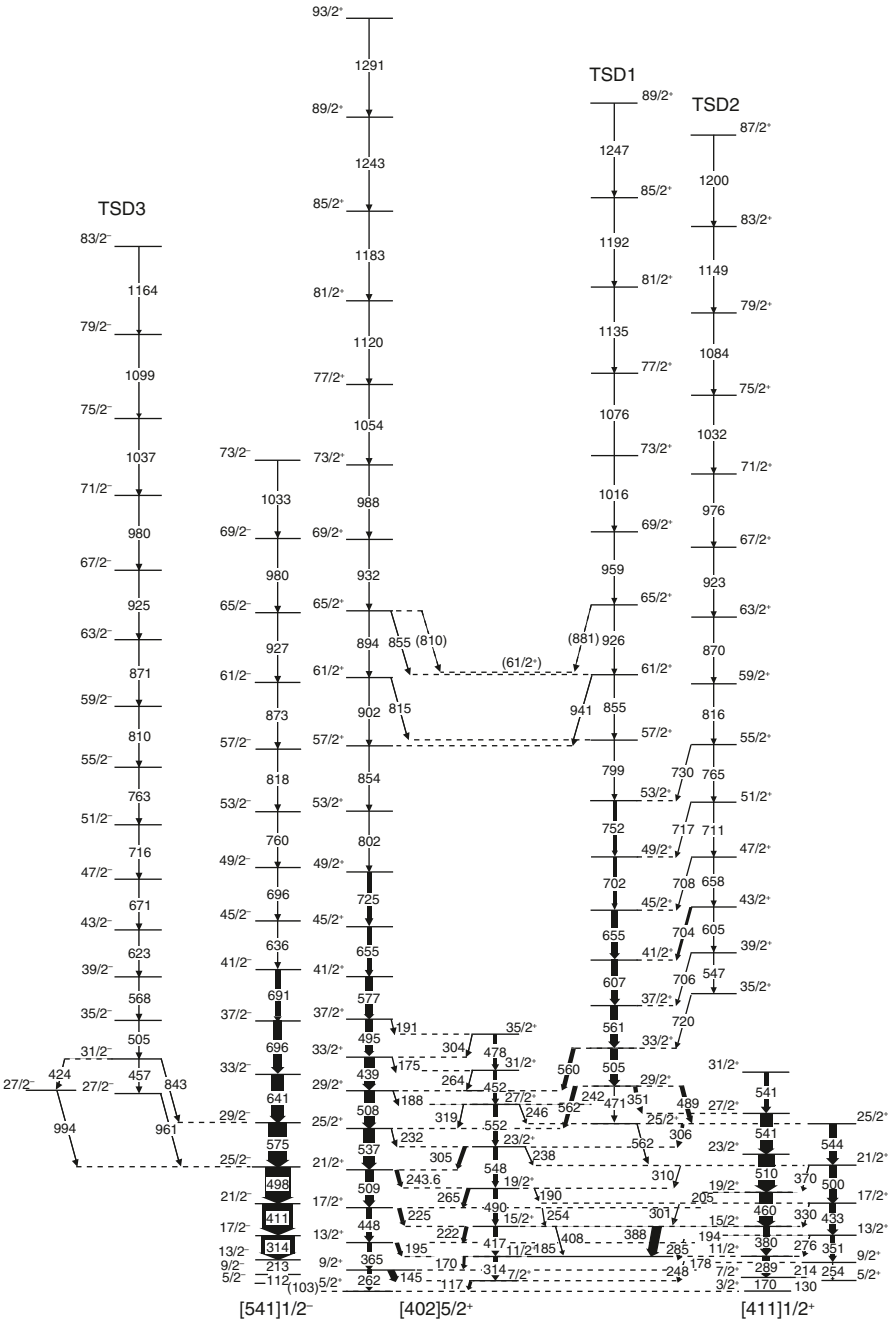

Fig. 3.9 Partial level scheme of ^{167}Lu [40]. (Figure reproduced with permission from [40])

Two TSD bands, TSD1 and TSD2 have been found in high-spin investigations of ^{161}Lu [13, 24, 25]. A partial level scheme of ^{161}Lu [25] depicting these bands is shown in Fig. 3.10. The population intensities of TSD1 and TSD2 have been estimated to be ~1.4% and 0.6% [25], respectively, of the ^{161}Lu reaction channel. The excitation energies of these TSD bands could not be determined as the gamma-ray transitions linking TSD1 band to the ND structures are not established [25]. The spin and parity assignments given in Fig. 3.10 for these TSD bands is based on close similarity of gamma-ray transition energies of TSD1 with those found for the TSD1 bands in ^{163}Lu (Fig. 3.7) and ^{165}Lu (Fig. 3.8). Three (possibly five) gamma-ray transitions of energies similar to those found for TSD2 to TSD1 inter-band gamma-ray transitions in ^{163}Lu and ^{165}Lu connect TSD2 to TSD1 bands in ^{161}Lu [25].

Lifetimes of excited states of TSD bands in ^{163}Lu, ^{165}Lu and ^{167}Lu have been measured [27, 32, 34, 35, 39]. In [35], accurate lifetimes, τ, were measured and transition quadrupole moments, Q_t, deduced for several states in TSD1 and TSD2 bands in ^{163}Lu (For the level scheme of ^{163}Lu, see Fig. 3.7) using the Doppler-shift attenuation method and the Gammasphere spectrometer. The results obtained are given in Table 3.5 reproduced from [35]. Since for the TSD1 band, there are no level decay branches in the spin range 41/2 to 69/2, the lifetimes can be directly converted into the $B(E2)$ strengths. For the band TSD2, in the level spin range 47/2 to 63/2, in addition to the in-band transitions, each of the levels has a decay branch to a level in TSD1 band as shown in Fig. 3.7. The branching ratios obtained in [20]

Table 3.5 Lifetimes, τ, deduced $B(E2)$ values and the transition quadrupole moments, Q_t, for the in-band transitions in the TSD bands TSD1 (upper part) and TSD2 (lower part) in ^{163}Lu [35]

I_i^π	$E\gamma$ (keV)	τ (ps)	$B(E2)$ (e^2b^2)	Q_t (b)
$41/2^+$	578.6	$0.364^{+0.073}_{-0.085}$	$3.45^{+0.80}_{-0.69}$	$9.93^{+1.14}_{-0.99}$
$45/2^+$	639.0	$0.250^{+0.035}_{-0.039}$	$3.07^{+0.48}_{-0.43}$	$9.34^{+0.72}_{-0.65}$
$49/2^+$	697.0	$0.202^{+0.021}_{-0.023}$	$2.45^{+0.28}_{-0.25}$	$8.32^{+0.47}_{-0.42}$
$53/2^+$	752.6	$0.119^{+0.009}_{-0.010}$	$2.84^{+0.24}_{-0.22}$	$8.93^{+0.38}_{-0.35}$
$57/2^+$	805.6	$0.096^{+0.011}_{-0.012}$	$2.50^{+0.32}_{-0.29}$	$8.37^{+0.54}_{-0.49}$
$61/2^+$	857.7	$0.088^{+0.010}_{-0.011}$	$1.99^{+0.26}_{-0.23}$	$7.45^{+0.49}_{-0.43}$
$65/2^+$	909.7	$0.067^{+0.010}_{-0.015}$	$1.95^{+0.44}_{-0.30}$	$7.37^{+0.82}_{-0.57}$
$69/2^+$	962.5	$0.047^{+0.017}_{-0.011}$	$2.10^{+0.80}_{-0.48}$	$7.63^{+1.46}_{-0.88}$
$47/2^+$	654.6	$0.215^{+0.037}_{-0.048}$	$2.56^{+0.57}_{-0.44}$	$8.51^{+0.95}_{-0.73}$
$51/2^+$	711.2	$0.144^{+0.017}_{-0.022}$	$2.67^{+0.41}_{-0.33}$	$8.67^{+0.66}_{-0.53}$
$55/2^+$	766.2	$0.095^{+0.013}_{-0.018}$	$2.81^{+0.53}_{-0.41}$	$8.88^{+0.83}_{-0.64}$
$59/2^+$	819.9	$0.087^{+0.026}_{-0.037}$	$2.19^{+0.94}_{-0.65}$	$7.82^{+1.66}_{-1.15}$
$63/2^+$	872.9	$0.064^{+0.013}_{-0.021}$	$2.25^{+0.75}_{-0.48}$	$7.91^{+1.32}_{-0.84}$
$67/2^+$	926.5	$0.075^{+0.017}_{-0.025}$	$1.60^{+0.52}_{-0.37}$	$6.66^{+1.09}_{-0.76}$
$71/2^+$	980.2	$0.056^{+0.017}_{-0.029}$	$1.61^{+0.82}_{-0.49}$	$6.68^{+1.70}_{-1.02}$

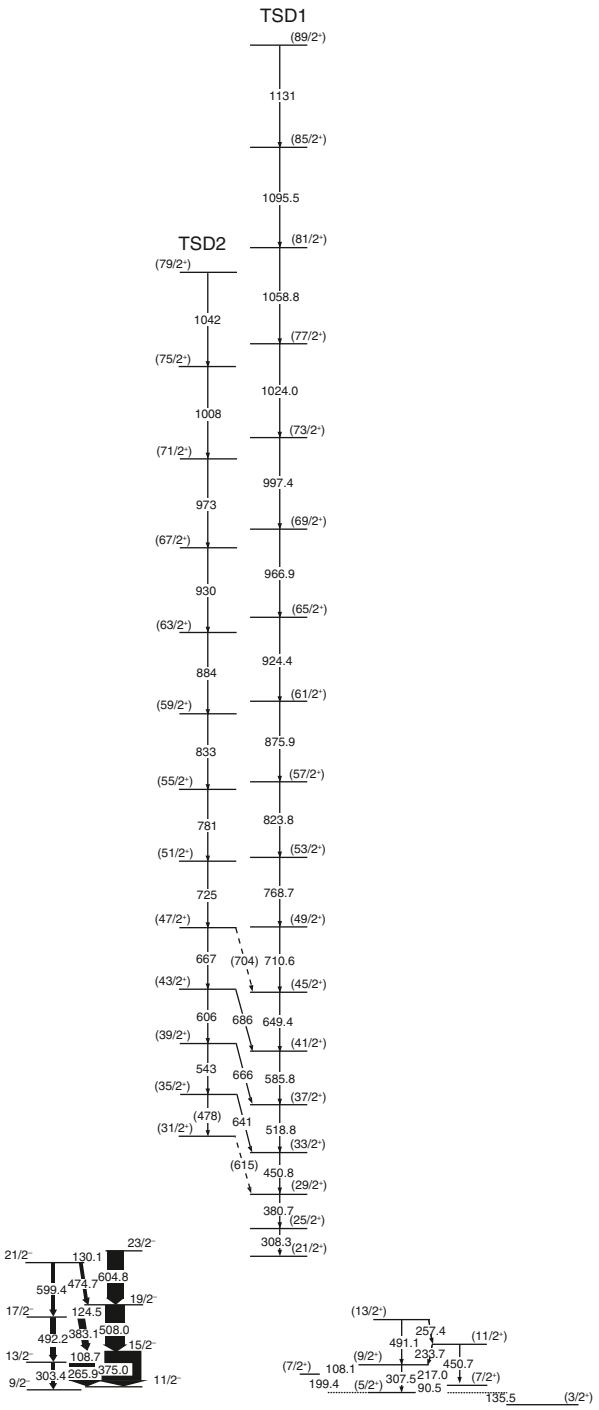

Fig. 3.10 Partial level scheme of ^{161}Lu [25]. (Figure reproduced with permission from [25])

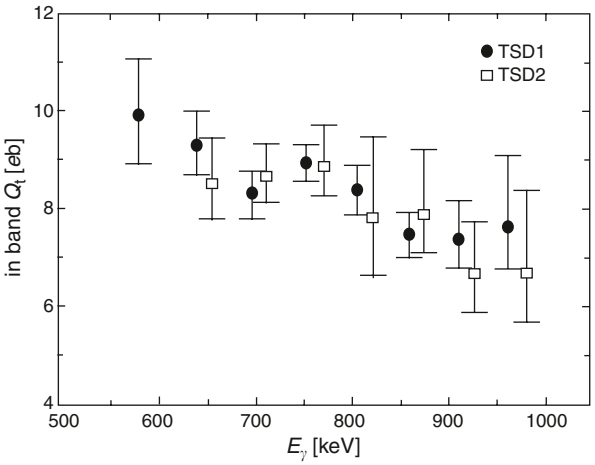

Fig. 3.11 Transition quadrupole moments, Q_t, in TSD bands *TSD1* and *TSD2* in ^{163}Lu as a function of in-band gamma-ray transition energy, E_γ [35]. (Figure reproduced with permission from [35])

have been used in this work to deduce the $B(E2)$ strengths. The $B(E2)$ values thus obtained in [35] are given in column 4 in Table 3.5.

The transition quadrupole moments, Q_t, for bands TSD1 and TSD2 in ^{163}Lu were extracted in [35] from the $B(E2)$ values using a distribution of different K-values since for a triaxial nucleus, K is not a good quantum number. For the details of calculations see [35]. The obtained Q_t values are given in column 5 of Table 3.5. In Fig. 3.11 the Q_t values are plotted as a function of gamma-ray transition energy [35]. This is a very interesting result. The Q_t values for both the bands (TSD1 and TSD2) decrease as a function of increase in E_γ (or increase in level spin). This may be due to the increase in triaxiality with the increase in spin. The Q_t values for the two TSD bands are very similar. These results indicate that the bands TSD1 and TSD2 are built on the same intrinsic structure.

The transition quadrupole moments for spins 41/2 and 47/2 are $Q_t = 9.93^{+1.14}_{-0.99}$ b, and $Q_t = 8.51^{+0.95}_{-0.79}$ b, in the bands TSD1 and TSD2 respectively in ^{163}Lu (see Table 3.5). These values are much larger than the transition quadrupole moment of the ND Yrast band in ^{163}Yb, $Q_t = 4.9^{+1.3}_{-0.4}$ b [34]. These experimental results along with the $Q_t = 6.0^{+1.2}_{-0.2}$ b and $Q_t = 6.4^{+1.9}_{-0.3}$ b [32] for the TSD1 band in ^{165}Lu are indicative of the fact that these TSD bands in ^{163}Lu and ^{165}Lu are strongly deformed. (See also [39] for Q_t for TSD1 in ^{167}Lu).

3.5 Discussion

Based on the results of the large number of experiments described in Sect. 3.4, the available evidence for wobbling motion in the even-N Lu isotopes will be given. The experimental results will also be compared with the theoretical predictions.

This comparison establishes the one-phonon and the two-phonon wobbling motion in these nuclei.

3.5.1 Experimental Evidence for Wobbling Motion

3.5.1.1 Structure of the TSD Bands

According the particle-rotor model calculations with a high-j quasiparticle coupled to a triaxial core, the family of wobbling bands, the zero-phonon ($n_w=0$) Yrast band, one-phonon ($n_w=1$) and the two-phonon ($n_w=2$) band, should be based on a very similar intrinsic structure [19]. To examine this possibility, in this section, we will consider the following rotational properties of the bands, excitation energy, aligned angular momentum, dynamic moment of inertia and the transition quadrupole moments, of the TSD bands in the even-*N* Lu isotopes.

In Fig. 3.12 are plotted the excitation energies of the TSD bands in $^{161, 163, 165, 167}$Lu nuclei along with those of the ND bands in these nuclei relative to a rigid rotor reference. Data are taken from [15, 16, 25, 30, 33]. The gamma decay from the excited TSD bands to TSD1 are marked by arrows in the figure. In the case of ^{163}Lu**,** the gamma decay from TSD3 to TSD2 are also shown. The gamma decay pattern between the TSD bands and the excitation energy behaviour as a function of spin are similar for these TSD bands. The energy separation between TSD1 and TSD2 are similar in these Lu nuclei whereas it is much smaller between TSD3 and TSD2 bands. This latter effect may be due to anharmonicity of the wobbling spectrum. One also notices from this figure that the excitation energy separation between TSD2 and TSD1 bands decreases with the increase in spin. This may suggest a gradual change in the individual moments of inertia. The energy separation between TSD3 to TSD2 remains almost independent of spin.

In Figs. 3.13 and 3.14 are shown the values of aligned angular momentum, i_x, and the dynamic moment of inertia, $\mathcal{I}^{(2)}$ as a function of the rotational frequency, $\hbar\omega$, for the TSD bands 1 to 3 in ^{163}Lu and ^{165}Lu respectively. The similarity of these values between the different TSD bands in each of the nuclei indicates that these bands are based on the same intrinsic structure. The TSD4 band in ^{163}Lu has been assigned as a three-quasiparticle band [36] and, therefore, not discussed here.

In Fig. 3.11 of Sect. 3.4, the transition quadrupole moments, Q_t, in the TSD bands 1 and 2 in ^{163}Lu are plotted as a function of E_γ (or it could be spin). The similarity of the values of Q_t and its behaviour with E_γ/spin for the two TSD bands further supports that these two bands are built on the same intrinsic structure.

It can, therefore, be concluded from the above experimental data that these TSD bands form a family of bands with very similar/identical rotational properties in each of the even-*N* Lu isotopes. This is in agreement with the wobbling phonon excitation formalism of the particle-rotor model in which one high-j ($i_{13/2}$) quasiparticle is coupled to a triaxial core [19] (see Sect. 3.3).

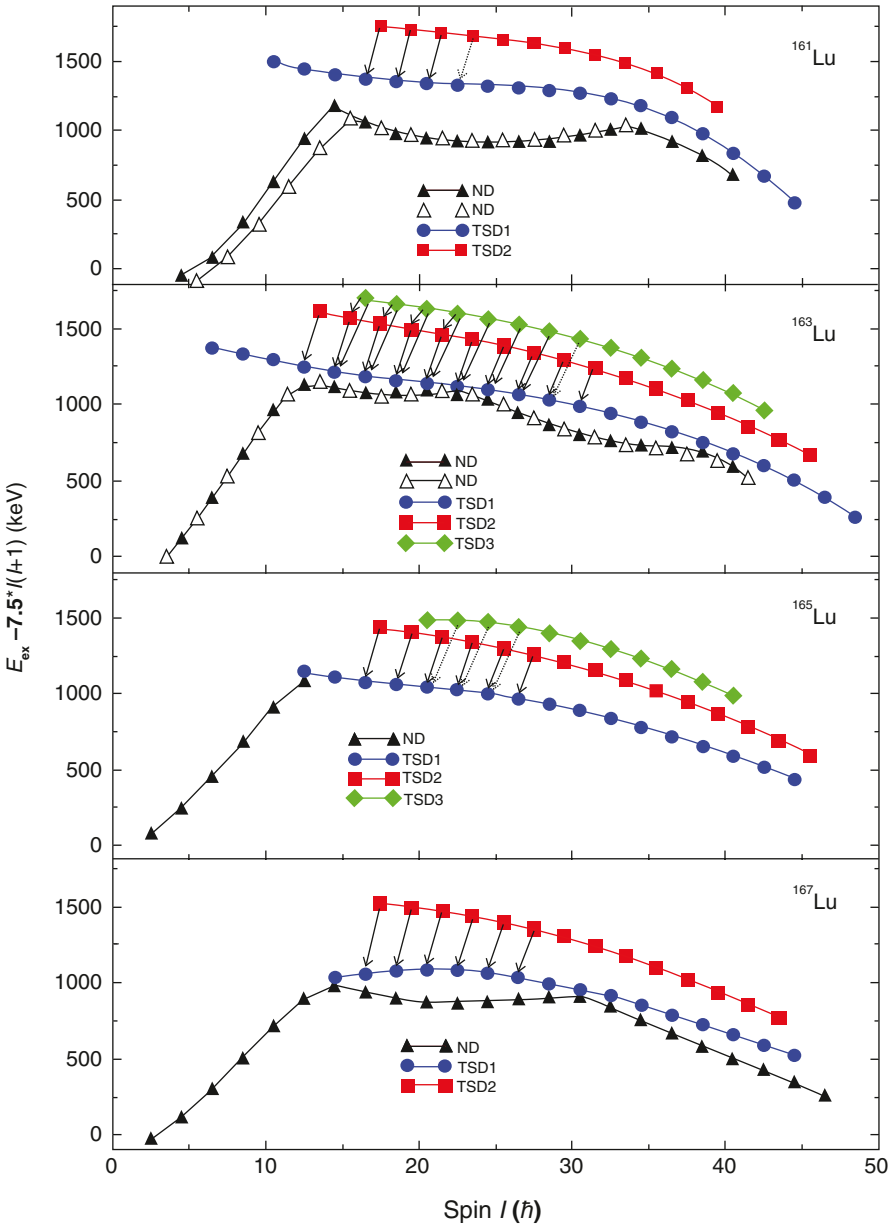

Fig. 3.12 Excitation energies relative to a rigid rotor reference for the TSD bands in $^{161, 163, 165, 167}$Lu. Also plotted are the relative excitation energies for the *ND* bands in these nuclei. Data are taken from [15, 16, 25, 30, 33]. Gamma decay from the excited TSD bands to *TSD1* are shown by *arrows*. In ^{163}Lu, the gamma decays from the bands *TSD3* to *TSD2* are also shown. (Figure reproduced with permission from [6])

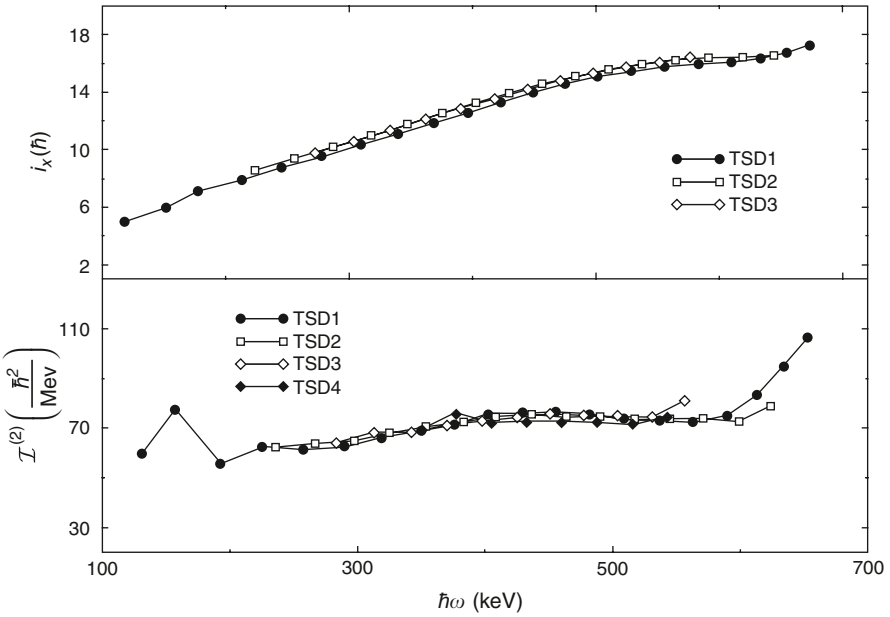

Fig. 3.13 Aligned angular momentum, i_x, (*top*) relative to a reference $I_{ref} = \mathcal{I}_0\omega + \mathcal{I}_1\omega^3$ with $\mathcal{I}_0 = 30\hbar^2$ MeV^{-1} and $\mathcal{I}_1 = 40\hbar^4$ MeV^{-3} and dynamic moment of inertia, $\mathcal{I}^{(2)}$, as a function of rotational frequency, $\hbar\omega$, for the *TSD bands 1–3* in ^{163}Lu [20]. (Figure reproduced with permission from [20])

3.5.1.2 Electromagnetic Properties of Gamma Decay Between the TSD Bands

Let us consider the size of the electromagnetic transition matrix elements. In particular, the $B(E2)_{\text{out}}/B(E2)_{\text{in}}$ ratios obtained from experimental measurements (see Sect. 3.4) for interconnecting $n_w{=}1 \rightarrow n_w = 0$, $n_w{=}2 \rightarrow n_w{=}1$ and $n_w{=}2 \rightarrow n_w{=}0$ transitions to the corresponding $\Delta n_w{=}0$ transitions for the TSD bands in even-N Lu isotopes. According to the wobbling phonon formalism [19, 21], in the high-spin limit, the $B(E2)_{\text{out}}/B(E2)_{\text{in}}$ ratio is given by the following expression [6]:

$$B(E2)_{\text{out}}/B(E2)_{\text{in}} \propto (n_w/I) \cdot [\sin^2(\gamma + 30°)/\cos^2(\gamma + 30°)]. \qquad (3.7)$$

These ratios are for large triaxiality with $\gamma{>}15°$ found to be independent of deformation, ε but for given γ and n_w values, these have a $(1/I)$ dependence. It may be mentioned here that for $\Delta I{=}1$ transitions observed in high-spin data at ND, the $B(E2)$ ratios have a $(1/I^2)$ dependence ('cranking regime'). In Fig. 3.15 are plotted the experimental values of the $B(E2)_{\text{out}}/B(E2)_{\text{in}}$ ratios which are listed in Tables 3.1 and 3.2, as a function of spin, for the TSD bands in ^{163}Lu. For the lowest and two highest experimental data points with $n_w{=}1 \rightarrow n_w{=}0$, the mixing

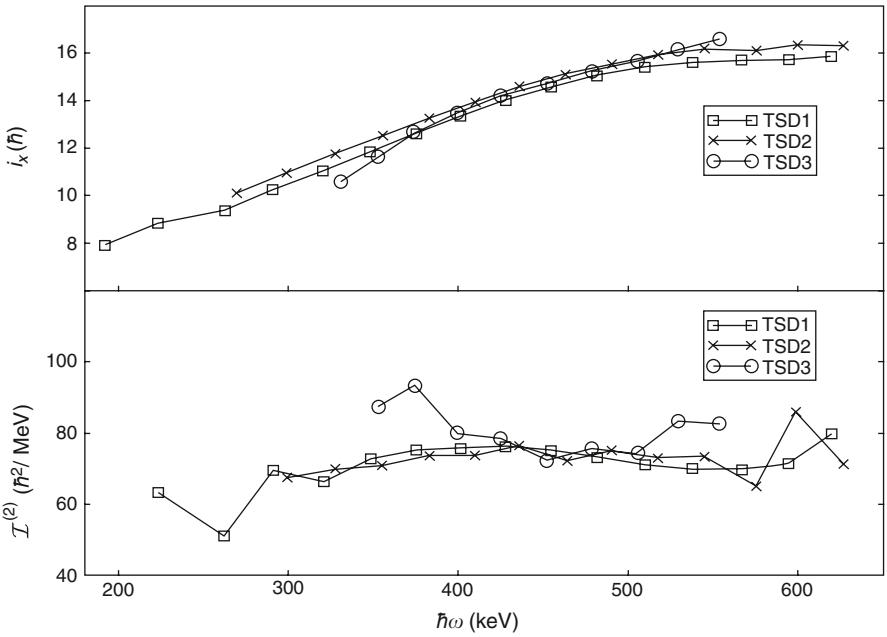

Fig. 3.14 Alignment, i_x (*top*) and dynamic moment of inertia, $\mathcal{I}^{(2)}$ (*bottom*), for the bands *TSD1*, *TSD2* and *TSD3* in ^{165}Lu as a function of rotational frequency, $\hbar\omega$. The alignment is relative to a reference $I_{ref} = \mathcal{I}_0\omega + \mathcal{I}_1\omega^3$ with $\mathcal{I}_0 = 30\hbar^2$ MeV^{-1} and $\mathcal{I}_1 = 40\hbar^4$ MeV^{-3} [15]. (Figure reproduced with permission from [15])

ratios are not measured but assumed to be the average value measured for J=35/2 to 51/2. The $B(E2)_{\text{out}}/B(E2)_{\text{in}}$ ratio values for these transitions are not given in Table 3.1 of Sect. 3.4. Also, the ratio for spin 51/2 given in the plot is a revised value [6]. The experimental ratios have a lack of (1/I) dependence. This may be indicative of a slight increase of γ-values with I in the observed spin region which

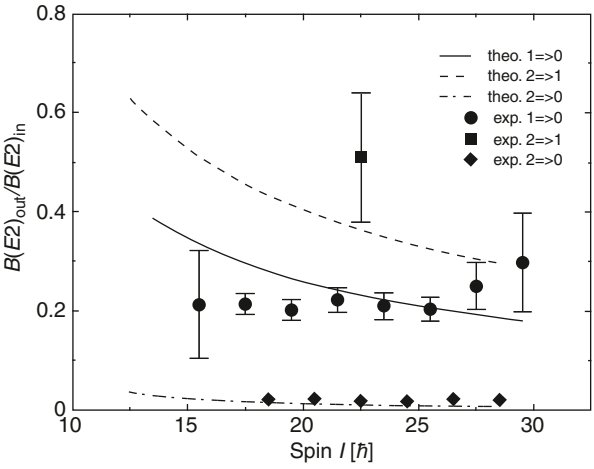

Fig. 3.15 Experimental $B(E2)_{\text{out}}/B(E2)_{\text{in}}$ ratios for the interconnecting n_w=1 → n_w=0, n_w=2 → n_w=1 and n_w=2 → n_w=0 transitions to the corresponding Δn_w=0 transitions respectively in ^{163}Lu [6 and references therein]. These values are compared with the theoretical calculations [21]. (Figure reproduced with permission from [6])

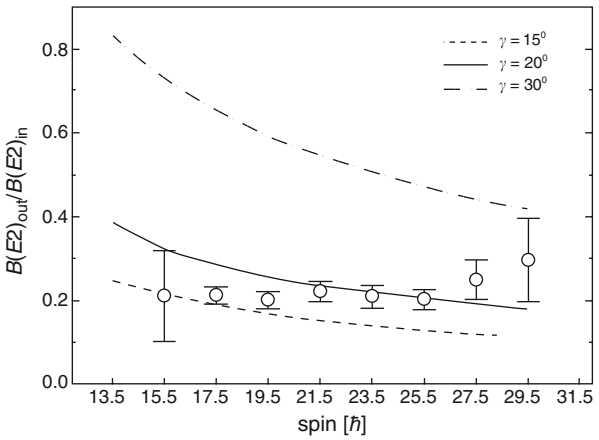

Fig. 3.16 Experimental $B(E2)_{out}/B(E2)_{in}$ ratios versus spin for interconnecting $\Delta I=1$ transitions from TSD2 to TSD1 to the corresponding in-band $\Delta I=2$ transitions in the TSD2 band (same as in Fig. 3.15) in ^{163}Lu [6 and references therein]. These are compared with the theoretical ratios for different values of γ, $\gamma=15°$, $\gamma=20°$ and $\gamma=30°$ [21]. (Figure reproduced with permission from [35])

is in qualitative agreement with the gradual decrease of the transition quadrupole transition moments with increase in spin/energy for both the $n_w=0$ (TSD1) and $n_w=1$(TSD2) wobbling bands in ^{163}Lu (see Fig. 3.11). Only one experimental value of $B(E2)_{out}/B(E2)_{in}$ ratio for the 476 keV interconnecting transition from the 45/2 level of TSD3 to TSD2 is available, $B(E2)_{out}/B(E2)_{in}=0.51\pm0.13$ [33]. This value

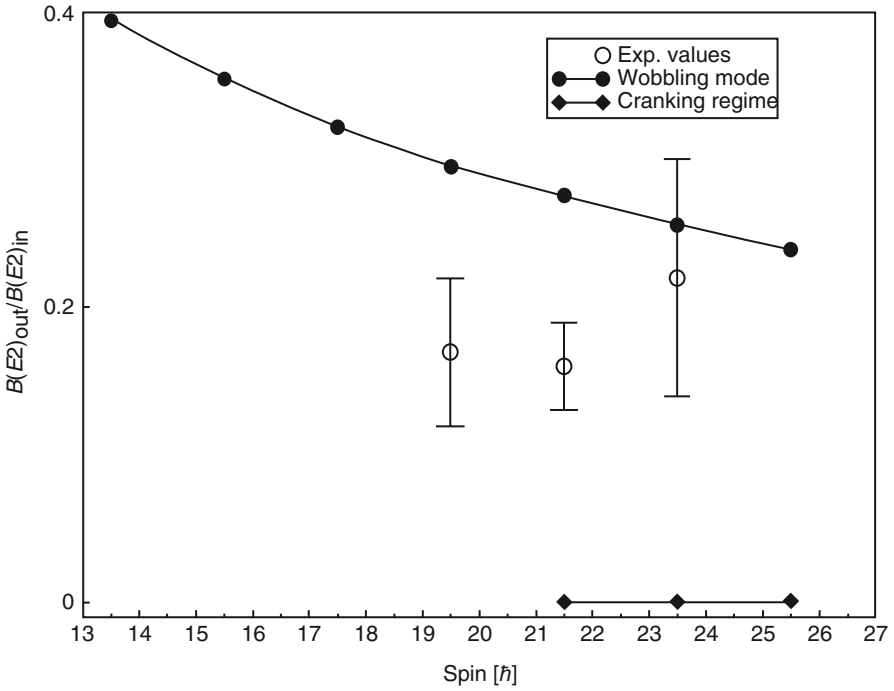

Fig. 3.17 Experimental $B(E2)_{out}/B(E2)_{in}$ ratios given in Table 3.3 in Sect. 3.4 versus spin, for interconnecting $\Delta I=1$ transitions from TSD2 to TSD1 to the corresponding in-band $\Delta I=2$ transitions in TSD2 band in ^{165}Lu. These values are compared with those from the particle-rotor model calculations [21]. (Figure reproduced with permission from [15])

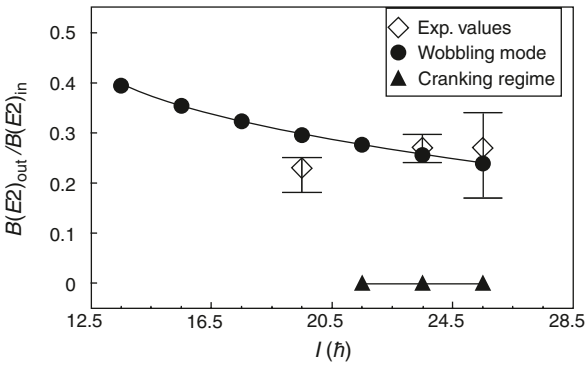

Fig. 3.18 Same as in Fig. 3.17, but for the TSD bands in ^{167}Lu. Data from Table 3.4, Sect. 3.4. Theoretical values are from [21]. (Figure reproduced with permission from [16])

has a comparatively large error. The value is also shown in the figure. The experimental $B(E2)_{out}/B(E2)_{in}$ ratios for TSD3 to TSD1 bands are listed in Table 3.2 in Sect. 3.4. These values which are about an order of magnitude smaller than the $B(E2)_{out}/B(E2)_{in}$ ratios for the $n_w=1 \rightarrow n_w=0$ transitions are also plotted in the figure. These experimental $B(E2)_{out}/B(E2)_{in}$ ratios are compared in Fig. 3.15 with the wobbling mode formalism calculations within the framework of the particle-rotor model [21]. The experimental ratios are in good to fair agreement with the theoretical predictions for the one-phonon and the two-phonon wobbling excitation modes in ^{163}Lu.

In Fig. 3.16 are plotted the experimental values of the $B(E2)_{out}/B(E2)_{in}$ ratios for the $n_w=1 \rightarrow n_w=0$ (i.e. from TSD2 to TSD1) interconnecting transitions to the relevant in-band gamma-ray transitions (same as in Fig. 3.15) as a function of spin, for the TSD bands in ^{163}Lu. These are compared with the theoretical values for three different γ values, $\gamma=15°$, $\gamma=20°$ and $\gamma=30°$ [21]. It can be concluded from this figure that the TSD bands in ^{163}Lu in the region of spin shown in the figure have $\gamma \sim 20°$.

The experimental values of $B(E2)_{out}/B(E2)_{in}$ ratios have also been determined for TSD2 to TSD1 $\Delta I=1$ interconnecting transitions to the in-band TSD2 transitions (see Tables 3.3 and 3.4 of Sect. 3.4) in ^{165}Lu and ^{167}Lu. These values are plotted as a function of spin in Figs. 3.17 and 3.18 and are compared with the theoretical values obtained from particle-rotor model calculations [21]. Although, in the case of ^{165}Lu, the experimental values have large errors, in both the nuclei, ^{165}Lu and ^{167}Lu, the agreement is fair for the one-phonon excitation mode.

3.6 Conclusion, Status and Outlook

In Sect. 3.5.1.1, based on the experimental findings, it was concluded that the family of TSD bands observed in the even-N Lu isotopes are based on the same intrinsic structure. In the subsequent Sect. 3.5.1.2, the electromagnetic properties of gamma decay between the TSD bands were considered. The experimental $B(E2)_{out}/B(E2)_{in}$

ratios obtained for TSD2 → TSD1 and TSD3 → TSD2 were found to be in agreement with the particle-rotor model calculations for one-phonon and the two-phonon wobbling excitations, respectively. This provides evidence for the presence of wobbling mode excitations and thereby uniquely establishes the existence of stable triaxiality in strongly deformed nuclei at high spins in even-*N* Lu nuclei.

It is still a challenge to establish wobbling mode excitations in odd–odd and even–even nuclei. Although, presumably TSD bands have been observed in odd–odd ^{162}Lu [24] and ^{164}Lu [43, 44] nuclei but no wobbling excitations have been found.

During the last some years, a large number of extensive and pain-staking experimental investigations have been done to search for triaxiality at high spins in the Tm–Yb–Hf–Ta–W nuclear region [45–60]. Early searches were made in ^{166}Hf [49] without any success in finding TSD bands. Searches for these bands were later made in several other neighbouring heavier mass Hf isotopes, like ^{168}Hf [50, 51], ^{170}Hf [52, 53], $^{171, 172}$Hf [54] and in $^{173, 174, 175}$Hf [55–58]. Based on rotational properties, according to [51], the strongly deformed bands observed in $^{170–175}$Hf can be suggested to fall into two groups, enhanced deformed (ED) bands with likely π ($i_{13/2}$, $h_{9/2}$) configuration and prolate shape with $\varepsilon_2 \sim 0.3$ and strongly deformed (SD) bands with the involvement of $\pi i_{13/2}$ and $\nu j_{15/2}$ orbitals. In ^{168}Hf, for one of the bands, some arguments have been put forward to make it qualify as a TSD band. But for none of these bands in the Hf isotopes enough evidence exists to support triaxiality in these nuclei. It may be that the wobbling bands may exist in these nuclei but these may be lying high in energy and, therefore, very low in intensities to be detected with the presently available even large gamma detector arrays. There is also a competition between the wobbling mode and the particle–hole excitations in these nuclei, in terms excitation energy placements of these bands at high spins. Bands based on particle–hole excitations have been found in ^{163}Lu [36] and ^{163}Tm [46].

Recently, evidence for wobbling mode has been found in ^{167}Ta [61] in an experiment using the Gammasphere array. Two TSD bands TSD1 and TSD2, with similar alignments and dynamic moment of inertia as a function of rotational frequency, as in ^{165}Lu, were found. In analogy with TSD1 band in ^{165}Lu, the new TSD1 band in ^{167}Ta is likely to be based on proton $\pi i_{13/2}$ configuration. The excitation energies of these new TSD bands also show similarities with the already observed TSD bands in ^{165}Lu. In addition, the significant observation is the identification of four (may be five) interconnecting gamma-ray transitions from TSD2 to TSD1 in ^{167}Ta. This decay pattern is characteristic of inter-band transitions found in the even-*N* Lu isotopes where the wobbling mode has been confirmed. The observed properties of these new TSD bands in ^{167}Ta strongly suggest that the rotational wobbling mode has been observed first time in a nucleus other than the even-*N* Lu isotopes. However, for a firm confirmation of this mode in ^{167}Ta nucleus, experimentally deduced values of $B(E2)_{out}/B(E2)_{in}$ ratios for the one-phonon excitations is required. For this purpose, mixing ratios of the interconnecting gamma-ray transitions need to be determined. But the relevant measurements for such determinations are difficult to undertake since the interconnecting gamma-ray transitions are of low intensities. Future lifetime measurements of excited states of the TSD bands in ^{167}Ta, when

possible, would provide the decisive evidence for the similarity of intrinsic structure of the bands.

In investigations of nuclear structure at ultra-high spins (I=45–65$\hbar$) using the Gammasphere array, extremely weak band structures have been established in a number of N~90 Er, Tm and Yb nuclei [62 and references therein]. Comparison of these structures having high dynamic moments of inertia with total Routhian surface calculations suggest that these bands beyond band terminating states may be the triaxial strongly deformed (TSD) bands. However, additional measurements like, e.g. lifetime measurements are required to establish their high deformation. Actually, a family of wobbling bands are needed to be discovered to find fingerprints for stable triaxial shapes at very high spins in these nuclei.

Finally, it may be mentioned that the development and the availability in future of large gamma-detector arrays with photopeak detection efficiencies, may be an order of magnitude higher than presently possible, would greatly enhance research, amongst other phenomena, in wobbling motion and the associated stable triaxiality at high spins in nuclei, also in other nuclear mass regions to establish wobbling as a general rotational phenomena in triaxial nuclei.

References

1. A. Bohr and B.R. Mottelson, *Nuclear Structure,* Vol. 2 (Benjamin, New York, 1975).
2. I. Hamamoto, Nucl. Phys. A 520, 297c (1990).
3. S. Frauendorf, Rev. Mod. Phys. 73, 463 (2001).
4. G.B. Hagemann and I. Hamamoto, *Nuclear Physics News,* 13, 20 (2003)
5. G.B. Hagemann, Eur. Phys. J. A 20, 183 (2004).
6. G.B. Hagemann, Acta Phys. Pol. B 36, 1043 (2005).
7. I. Ragnarsson, Phys. Rev. Lett. 62, 2084 (1989).
8. S. Åberg, Nucl. Phys. A 520, 35c (1990).
9. R. Bengtsson, http://www.matfys.lth.se/~ragnar/TSD - defsyst.html.
10. T. Bengtsson, Nucl. Phys. A 496, 56 (1989).
11. T. Bengtsson, Nucl. Phys. A 512, 124 (1990).
12. R. Bengtsson et al., Nucl. Phys. A 569, 469 (1994).
13. P. Bringel et al., Phys. Rev. C 73, 054314 (2006).
14. I. Hamamoto et al., Acta Phys. Pol. B 32, 2545 (2001).
15. G. Schönwasser et al., Phys. Lett. B 552, 9 (2003).
16. H. Amro et al., Phys. Lett. B 553, 197 (2003).
17. R. Bengtsson and H. Ryde, Eur. Phys. J. A 22, 355 (2004).
18. Y.R. Shimizu and M. Matsuzaki, Nucl. Phys. A 588, 559 (1995).
19. I. Hamamoto, Phys. Rev. C 65, 044305 (2002).
20. D.R. Jensen et al., Nucl. Phys. A 703, 3 (2002).
21. I. Hamamoto and G.B. Hagemann, Phys. Rev. C 67, 014319 (2003).
22. M. Matsuzaki et al., Phys. Rev. C 69, 034325 (2004).
23. K. Tanabe and K. Sugawara – Tanabe, Phys. Rev. C 73, 034305 (2006).
24. P. Bringel et al., Eur. Phys. J. A 16, 155 (2003).
25. P. Bringel et al., Eur. Phys. J. A 24, 167 (2005).
26. W. Schmitz et al., Nucl. Phys. A 539, 112 (1992).
27. W. Schmitz et al., Phys. Lett. B 303, 230 (1993).

28. H. Schnack – Petersen et al., Nucl. Phys. A 594, 175 (1995).
29. J. Domscheit et al., Nucl. Phys. A 660, 381 (1999).
30. S.W. Odegård et al., Phys. Rev. Lett. 86, 5866 (2001).
31. S.W. Odegård et al., Nucl. Phys. A 682, 427c (2001).
32. G. Schönwasser et al., Eur. Phys. J. A 15, 435 (2002).
33. D.R. Jensen et al., Phys. Rev. Lett. 89, 142503 (2002).
34. G. Schönwasser et al., Eur. Phys. J. A 13, 291 (2002).
35. A. Görgen et al., Phys. Rev. C 69, 031301(R) (2004).
36. D.R. Jensen et al., Eur. Phys. J. A 19, 173 (2004).
37. G. Schönwasser et al., Nucl. Phys. A 735, 393 (2004).
38. C.X. Yang et al., Eur. Phys. J. A 1, 237 (1998).
39. G. Gürdal et al., J. Phys. G : Nucl. Part. Phys. 31, S 1873 (2005).
40. H. Amro et al., Phys. Rev. C 71, 011302 (2005).
41. G. Gürdal et al., Phys. Rev. C 77, 024314 (2008).
42. M. Metlay et al., Nucl. Instru. Meth, A 336, 162 (1993).
43. S. Törmänen et al., Phys. Lett. B 454, 8 (1999).
44. P. Bringel et al., Phys. Rev. C 75, 044306 (2007).
45. C. Teal et al., Phys. Rev. C 78, 017305 (2008).
46. N.S. Pattabiraman et al., Phys. Lett. B 647, 243 (2007).
47. X. Wang et al., Phys. Rev. C 75, 064315 (2007).
48. A. Aguilar et al., Phys. Rev. C 77, 021302 (R) (2008).
49. D.R. Jensen et al., Eur. Phys. J. A 8, 165 (2000).
50. H. Amro et al., Phys. Lett. B 506, 39 (2001).
51. R.B.Yadav et al., Phys. Rev. C 78, 044316 (2008).
52. A. Neusser et al., Eur. Phys. J. A 15, 439 (2002).
53. A. Neusser – Neffgen et al., Phys. Rev. C 73, 034309 (2006).
54. Y.C. Zhang et al., Phys. Rev. C 76, 064321 (2007).
55. D.J. Hartley et al., Phys. Lett. B 608, 31 (2005).
56. M.K. Djongolov et al., Phys. Lett. B 560, 24 (2003).
57. M.A. Riley et al., Phys. Scr. T 125, 123 (2006).
58. D.T. Scholes et al., Phys. Rev. C 70, 054314 (2004).
59. D.J. Hartley et al., Phys. Rev. C 72, 064325 (2005).
60. S.K. Tandel et al., Phys. Rev. C 77, 024313 (2008).
61. D.J. Hartley et al., Phys. Rev. C 80, 041304 (R) (2009).
62. M.A. Riley et al., Acta Phys. Pol. B 40, 513 (2009).

Chapter 4
Chirality in Nuclei

4.1 Introduction

In recent years, one of the most interesting and challenging aspects in high-spin nuclear structure physics has been to prove experimentally the existence of static nuclear chirality. The occurrence of chirality will provide a unique test for the existence of stable triaxial nuclear shapes at moderate spins. A large number of experimental investigations have, therefore, been undertaken during the last about a decade, in a number of nuclei in the mass regions, $A \sim 100$, $A \sim 130$ and in some nuclei in $A \sim 190$. Many theoretical attempts have been made to explain and understand the phenomenon of chirality in nuclei. In the present chapter, details of this phenomenon and experimental results on the candidate chiral doublet bands in nuclei are discussed.

A number of review articles on the topic exist in the literature [1–4].

It may be mentioned here that the phenomena of triaxial strong deformation and wobbling motion provided the first evidence of the existence of stable triaxial shapes in nuclei at high spins. This topic is discussed in Chap. 3.

4.2 The Nuclear Chiral[1] Phenomenon

The occurrence of chirality in nuclei was first predicted in the year 1997 by Frauendorf and Meng [5]. This effect is expected to occur in rotational motion at moderately high spins in triaxially deformed nuclei and in which there are a few high-j valence particles and a few high-j valence holes.

In [5], a system involving an $h_{11/2}$ proton particle and $h_{11/2}$ neutron hole coupled to a triaxially deformed core was studied. In the mass $A \sim 130$ region, the proton Fermi level is located in the lower part of valence proton high-j (particlelike) $h_{11/2}$ subshell and in the upper part of the valence neutron high-j (holelike) $h_{11/2}$ subshell. For a triaxial nucleus, having three mutually perpendicular principal axes, short (s),

[1] Chiral (adj.) —origin from Greek **kheir** ‘hand’.

S. C. Pancholi, *Exotic Nuclear Excitations,* Springer Tracts in Modern Physics 242,
DOI 10.1007/978-1-4419-8038-0_4, © Springer Science+Business Media, LLC 2011

intermediate (i) and long (l), the angular momentum vector of the high-j valence proton particle, $\mathbf{j}_\pi$, is aligned along the short (s) axis because its torus-like density distribution which is perpendicular to $\mathbf{j}_\pi$, in the l–i plane, gives a maximum overlap with the triaxial core. The high-j neutron hole tends to align its angular momentum $\mathbf{j}_\upsilon$, along the long l-axis because its dumbbell-shaped density distribution (sphere minus torus) has maximum overlap with the core if its (that of the distribution) symmetry axis is parallel to the l-axis. Such a coupling of both the valence particle and the hole with the triaxial core minimizes the interaction energy with the core. The collective (core rotational) angular momentum vector, **R**, tends to align along the intermediate (i) axis as this axis possesses the largest (irrotational flow) moment of inertia for $\gamma = -30°$ [6], thus minimizing the rotational energy. This situation where $\mathbf{j}_\pi$, $\mathbf{j}_\upsilon$ and **R** are mutually perpendicular is illustrated in Fig 4.1. These three mutually perpendicular angular momenta, that, for the proton particle, $\mathbf{j}_\pi$, for the neutron hole $\mathbf{j}_\upsilon$, and for the core rotation, **R**, can be arranged in the body-fixed frame to form two systems of opposite handedness, namely, a left-handed or a right-handed depending upon the direction of core rotational angular momentum vector. The total angular momentum **J** then does not lie in any of the three principal planes (aplaner solution). The total angular momentum, **J**, chooses one of the two systems (left-handed or the right-handed), thus introducing chirality. The two systems are transformed into each other by the chiral operator, which is a combination of the time reversal and rotation by 180°, $\chi = TR\ (\pi)$. When the chiral symmetry is thus broken in the body fixed frame, the restoration of the symmetry in the laboratory frame is manifest as degenerate doublet $\Delta I = 1$ bands (chiral doublet bands) of the same parity from the doubling of states. According to [5, 8], the degeneracy persists over a limited spin range. Chiral geometry formation is a dynamical process as a function of spin. Near the bandhead where the rotational angular momentum contribution, **R** is small, the total angular momentum vector, **J**, lies close to the principal plane formed by $\mathbf{j}_\pi$ and $\mathbf{j}_\upsilon$, i.e. the s-l plane and the chiral geometry cannot be defined. At intermediate spins, when **R** becomes comparable to $\mathbf{j}_\pi$ and $\mathbf{j}_\upsilon$, **J** becomes aplaner, i.e. it is no longer close to the s-l principal plane but tilts towards the

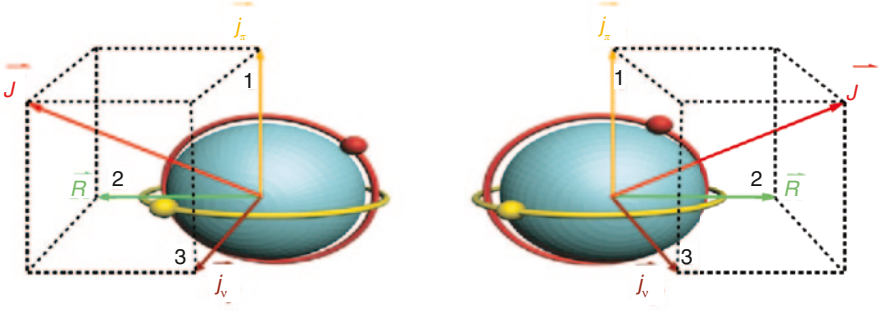

Fig. 4.1 Schematic representation of orientation of the coupling of particle and hole angular momenta with that of a triaxial even–even deformed core, forming left-handed or a right-handed coordinate system. Note the orientations of ***R*** and ***J*** in the two systems. (Figure reproduced with permission from [3]; see also [7])

intermediate axis. The chiral geometry is then formed and the chiral twin states (degenerate states) should appear. At higher spins, the total angular momentum vector **J** slowly aligns with the rotation axis and the degeneracy vanishes. It can, therefore, be conjectured that chirality is a combined effect of dynamics (the angular momentum) and geometry (the triaxial nuclear core).

The first experimental evidence of candidate chiral doublet bands, as pointed out in [5], was already available in the literature in the odd–odd nucleus ^{134}Pr [9] where a Yrast band based on $\pi h_{11/2} \otimes \upsilon h_{11/2}^{-1}$ configuration and its partner band were observed but without any reference to chiral interpretation in [9] since the chiral phenomenon was not known then. Since its prediction in 1997, chirality in triaxial nuclei, which is an important topic of current interest because it could provide direct evidence for stable triaxial nuclear shapes, has been intensively investigated both theoretically and experimentally.

4.3 Fingerprints of Nuclear Chirality

Based upon one particle and one hole coupled to triaxial deformed even–even core model calculations, a number of fingerprints for experimental observables have been suggested which may serve as signatures for identifying and qualifying candidate doublet bands as chiral partners in nuclei [5, 10–14].

1. Existence of near degenerate doublet levels of the same spin and parity in the $\Delta I = 1$ bands based on the same single-particle configuration. There is a gradual increase in the energy separation between the doublet bands as the spin decreases because of the increasing admixture of planer solutions into the aplaner solutions. At higher spins, both the bands due to achieving aplaner scenario yield near chiral degeneracy around a certain region of high spin.
   The closeness of excitation energy between the doublet bands is not a very strong argument to claim these bands as chiral partner bands. Fingerprint 3.(c) is essential to be satisfied for the purpose.
2. Both the members of the doublet structure should show a smooth variation, i.e. there should be no staggering of the quantity $S(I)$ defined as $S(I) = [E(I) - E(I-1)]/2I$ as a function of spin I above a specific spin. In other words, $S(I)$ should be independent of spin in the chiral region. This situation for chiral geometry can be understood based on the following argument. The changes (staggering) in the quantity $S(I)$ for odd–odd and also for odd nuclei occur due to the Coriolis interactions between the particle and hole angular momenta and the core rotational angular momentum. As has been described earlier, for chiral geometry, the valence nucleon angular momenta and the core rotational angular momentum are mutually perpendicular. In this scenario, the contribution of Coriolis interaction is greatly reduced since these contributions are proportional to the scaler product of the vectors involved. Therefore, for chiral geometry, the quantity $S(I)$ as a function of spin should show almost no staggering. The independence of

$S(I)$ with spin also means that the moment of inertia remains constant as a function of spin as $S(I)^{-1}$ is equal to the moment of inertia.

3. Detailed theoretical investigations of the properties of the inband and interband electromagnetic transitions for the chiral doublet bands predict the following:
   (a) A characteristic staggering of the inband $B(M1)/B(E2)$ ratios as a function of spin I. The chiral symmetry restricts the phase of the staggering such that for odd- (even-) parity bands, the even (odd) spins should have high $B(M1)/B(E2)$ values and odd (even) spins should have low values of this ratio.
   (b) A similar staggering with the same phase should be observed for the inband and out of band $B(M1)_{in}/B(M1)_{out}$ ratios for transitions from levels in the partner band.
   (c) The $B(M1)$ and the $B(E2)$ transition strengths as a function of spin should be very similar for the chiral partner bands in a nucleus. This will imply similar nuclear shapes associated with the two bands. Therefore, the $B(M1)/B(E2)$ ratios as a function of spin should also be very similar for the two bands. Disagreement of the absolute transition strengths and their ratios between the doublet bands would disqualify the observed bands to be interpreted as chiral partner bands.
4. The two degenerate bands should have very similar physical properties, like, quasiparticle (qp) alignments, moments of inertia and electromagnetic properties (see 3.(c) above).

For some additional suggested fingerprints of chirality, see [12, 15].

4.4 Experimental Results

4.4.1 Odd–Odd Nuclei

Strongly coupled $\Delta I = 1$ doublet bands have been found at high spins in $A \sim 100$ mass region in ^{100}Tc [16], ^{102}Rh [17, 18], ^{104}Rh [11, 19], ^{106}Rh [20] and ^{106}Ag [21] odd–odd nuclei. High-spin structures in ^{100}Tc were investigated in [16] using the ^{96}Zr (^{3}Li, 3n) reaction at a beam energy of 27 MeV. The emitted gamma-rays were detected in a gamma-detector array of six Compton-suppressed HPGe detectors. Multipolarities of gamma-rays were determined from the measured values of the directional correlation of oriented nuclei (DCO) ratios. A partial level scheme of ^{100}Tc deduced in the work [16] is shown in Fig. 4.2. The interconnecting gamma-ray transitions from band B to band A are of $M1/E2$ multipolarities. In band A and band B, the $\Delta I = 1$ transitions are predominantly of stretched dipole character. The spins and parity of levels in band A were adopted from a previous work [22] on this nucleus. The configuration $\pi g_{9/2}^{-1} \otimes \nu h_{11/2}$ was assigned to the band. Using this information, assigned multipolarities to the transitions connecting band B to band A and system-

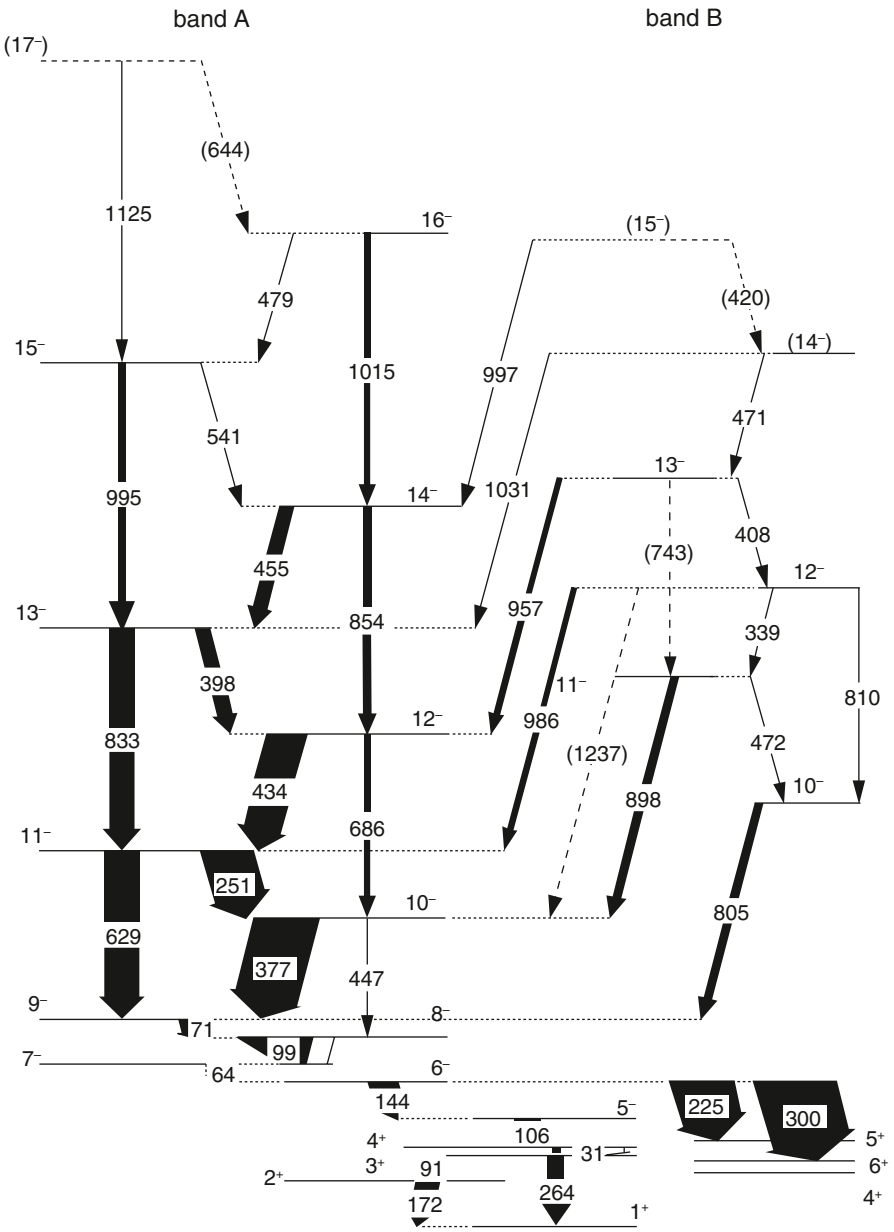

Fig. 4.2 Partial level scheme of ^{100}Tc [16]. (Figure reproduced with permission from [16])

atics of similar level structures observed in $^{102,\,104,\,106}$Rh odd–odd nuclei, the partner band (band B) in ^{100}Tc was also assigned the $\pi g_{9/2}^{-1} \otimes \nu h_{11/2}$ configuration.

The level schemes of ^{102}Rh [17, 18], ^{104}Rh [11] and ^{106}Rh [20] are shown in Fig. 4.3a–c. In ^{102}Rh, the spins and parity of the Yrast band (band A) which is based on the 6^- state (not shown in the level scheme) at 683 keV, were established from the multipolarities determined from the DCO ratios and linear polarisation measurements. The interconnecting gamma-ray transitions from the partner band (band B) to the Yrast band (band A) are of $\Delta I = 1$ and $\Delta I = 2$ types. No other details of the level scheme are available.

High-spin states in ^{104}Rh were populated in the reaction ^{96}Zr (^{11}B, 3n) at ^{11}B beam energy of 40 MeV [11]. The emitted gamma-rays were detected in the Gammasphere array. In the partial level scheme of ^{104}Rh (Fig. 4.3b), a strongly coupled $\Delta I = 1$ Yrast band (band A) and a sister band (band B) which feeds into the Yrast band by a number of gamma-rays of stronger $\Delta I = 1$ and weaker $\Delta I = 2$ transitions were found [11]. The g-factor measurement [11 and references therein] of the $T_{1/2} = 42$ ns isomeric 6^- state on which the Yrast band is based was found to have the $\pi g_{9/2} \otimes \nu h_{11/2}$ configuration. Extensive DCO ratio measurements of the in-band and interband transitions were performed in [11]. Spins and parity for the levels in the side band were established from the DCO ratios of the three strong interconnecting 745, 741 and 734 keV gamma-ray transitions. Linear polarisation measurement of the 741 keV transition agrees with the $\Delta I = 1$ $M1/E2$ assignment for these transitions. Thus, establishing parity for the partner band same as that for the Yrast band. This, along with the assignment of $\pi g_{9/2}^{-1} \otimes \nu h_{11/2}$ configuration for the Yrast band (band A) proves that the partner band (band B) has also the same $\pi g_{9/2}^{-1} \otimes \nu h_{11/2}$ configuration.

Lifetimes of the Yrast band in ^{104}Rh were measured in [19] by the recoil distance Doppler shift method. The results are given in Table 4.1.

Nuclear spectroscopic investigations of high-spin states in ^{106}Rh were reported in [20] by populating these states in the fusion evaporation reaction ^{96}Zr (^{13}C, p2n) at ^{13}C beam energy of 51 MeV. This reaction channel is weak with an estimated cross-section of 2–4 mb [20]. The gamma-rays emitted in the reaction were detected in the EUROBALL IV array consisting only of the Clover and the Cluster Ge detectors. The proton channel was selected using the DIAMANT charged particle array. The partial level scheme of ^{106}Rh obtained in the work is shown in Fig. 4.3c. Two strongly coupled $\Delta I = 1$ bands, band A and band B with cross-over transitions, were observed. A number of $\Delta I = 1$ and $\Delta I = 2$ gamma-ray transitions from band B connect to band A. The configuration $\pi g_{9/2}^{-1} \otimes \nu h_{11/2}$ of the Yrast band A which was inferred from the systematics of neighbouring odd–odd, odd-Z and odd-N nuclei in [23, 24] was adopted. The DCO ratio measurements for the 377 keV and the DCO and linear polarisation measurement for the 471 + 472 keV doublet transition in band B are consistent with an $M1$ assignment. The DCO ratio measurements for the 626, 650 and 770 keV and linear polarisation measurements of two of these interconnecting transitions from band B to band A are consistent with $\Delta I = 1$ $M1/E2$ multipolarity. This establishes that band B has the same negative parity as that for band

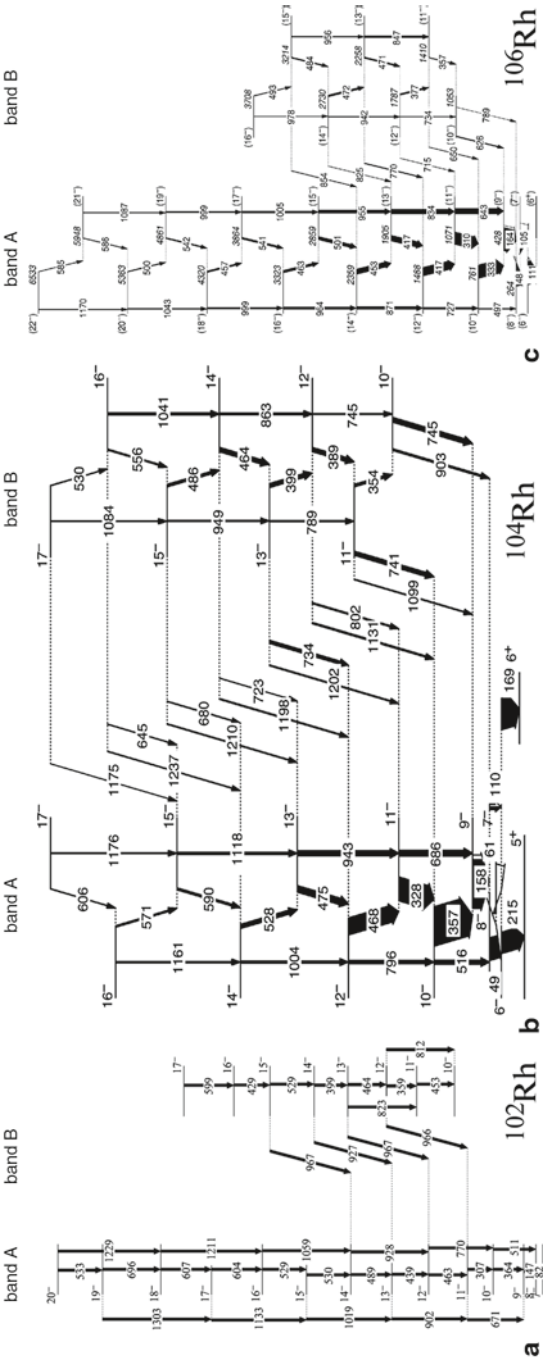

Fig. 4.3 Partial level schemes of **a** ^{102}Rh [18], **b** ^{104}Rh [11] and **c** ^{106}Rh [20]. (Figure reproduced with permission from [11, 18, 20])

Table 4.1 Experimental values of lifetimes and the deduced reduced transition probabilities $B(M1)$ and $B(E2)$ for states in the Yrast band in ^{104}Rh [19]

J^{π} ($\hbar$)	E_{γ} (keV)	τ (ps)	$B(M1)$ $(\mu_N)^2$	$B(E2)$ $(eb)^2$
9^-	158	6.21 ± 0.45	2.3 ± 0.2	–
10^-	357	1.25 ± 0.09	0.95 ± 0.08	0.063 ± 0.017
11^-	328	1.34 ± 0.12	0.91 ± 0.12	0.093 ± 0.020
12^-	468	1.05 ± 0.10	0.44 ± 0.06	0.039 ± 0.010
13^-	475	0.71 ± 0.19	0.42 ± 0.15	0.067 ± 0.025

A. On the basis of the feeding pattern from band B to band A and the same parity of the two bands, the configuration of band B can also be adopted to be $\pi g_{9/2}{}^{-1} \otimes \nu h_{11/2}$.

As in the odd–odd $^{102, 104, 106}$Rh isotopes, a pair of doublet bands were also found in the odd–odd ^{106}Ag nucleus [21]. High-spin states in ^{106}Ag were populated using the ^{100}Mo (^{10}B, 4n) fusion evaporation reaction at a beam energy of 42 MeV. The emitted gamma-rays were detected in the Gammasphere array. The partial level scheme of ^{106}Ag as obtained from the results of the work, is shown in Fig. 4.4. Both bands, band 1, the Yrast band and the partner band, band 2 contain strong $M1$ transitions and cross-over $E2$ transitions of moderate gamma-ray intensities. The decay pattern of the several gamma-ray transitions interconnecting band 2 to band 1 is similar to that observed in the odd–odd $^{102, 104, 106}$Rh nuclei. The multipolarity

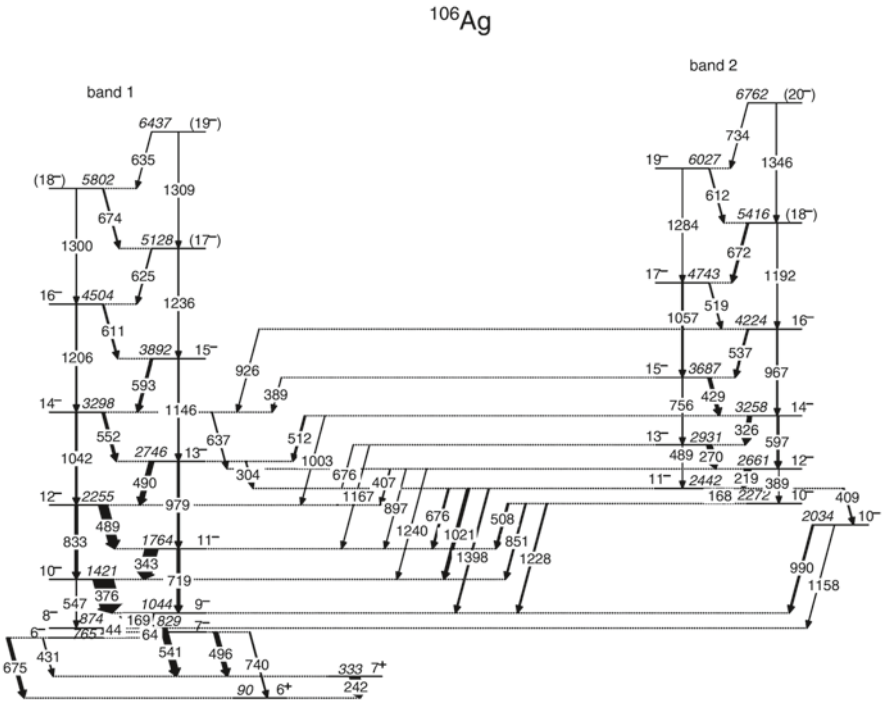

Fig. 4.4 Partial level scheme of ^{106}Ag [21]. (Figure reproduced with permission from [21])

of the strong interconnecting transitions is of mixed $M1/E2$ type and those of the weaker $\Delta I = 2$ transitions is $E2$ [21]. This observation suggests that band 2 has the same negative parity as of band 1. If band 1 has a configuration $\pi g_{9/2}{}^{-1} \otimes \nu h_{11/2}$ from systematics of bands observed in other neighbouring odd–odd Rh and Tc nuclei, then band 2 has the same configuration.

In odd–odd nuclei in mass region $A \sim 130$, energy doublet bands based on the $\pi h_{11/2} \otimes \nu h_{11/2}{}^{-1}$ configuration have been observed in ^{126}Cs [25], ^{128}Cs [10, 26], ^{130}Cs [7, 10, 27], ^{132}Cs [28, 29], ^{130}La [26], ^{132}La [7, 30], ^{134}La [31], ^{132}Pr [26], ^{134}Pr [32], ^{136}Pm [7, 33–36] and ^{138}Eu [34, 35].

Recently, doublet bands have also been found in the mass ~190 region in ^{188}Ir [37] and ^{198}Tl [38].

In addition to the observation of energy doublet bands in the above-mentioned nuclei, lifetimes of excited states in these bands have also been measured in ^{128}Cs [39–41], ^{132}La [39–41] and ^{134}Pr [42, 43].

The fingerprints of nuclear chirality are mentioned in Sect. 4.3. It is apparent from these that the observation of near degenerate doublet bands is not a sufficient condition to establish the observation of static chirality in nuclei. The intrinsic nuclear structure of the partner bands has to be the same or very similar. A stringent test for this is obtained from the electromagnetic properties of the gamma-ray transitions within the bands and between the bands. Lifetime measurements of excited states of these bands provide crucial information about shape similarity between the partner bands. As the doublet bands have been investigated in a number of odd–odd nuclei, instead of discussing the experimental results for all these nuclei, in this section, the details are considered only for a few nuclei, like ^{128}Cs, ^{132}La and ^{134}Pr where the data from lifetime measurements for the band members are available.

In the work reported in [10, 26], high-spin states in the odd–odd nucleus ^{128}Cs were investigated using the fusion evaporation reaction ^{122}Sn (^{10}B, 4n) at a beam energy of 47 MeV. Pulsed ^{10}B beam with a period of 106 ns was used for prompt and delayed timings. The emitted gamma-rays were detected in an array of six Compton-suppressed Ge detectors. The partial level scheme of ^{128}Cs as obtained in the work is shown in Fig. 4.5. Two $\Delta I = 1$ bands—band Y (a Yrast band) and a side band S—were populated. Band S is connected to band Y by a number of gamma-ray transitions. Multipolarities of the inband and the interconnecting gamma-ray transitions between band S and band Y were obtained from the DCO ratio measurements. The $\Delta I = 1$,143, 349, 273, 408, 371 and 464 keV inband transitions in band Y and the 372 keV transition in band S were found to be dipole/quadrupole and, therefore, assumed to be of $M1/E2$ type. The $\Delta I = 2$,779 keV and the 875 keV transitions were accepted to be of $E2$ type. The multipolarities of the 509, 532, 622, 571 and the 639 keV transitions were inferred to be mixed $\Delta I = 1$ $M1/E2$ from the DCO ratio measurements in the work. This observation ensures same positive parity for the partner band S. The absolute spins and parity assignments for the band Y and band S in ^{128}Cs are based on the systematics of doublet bands observed in $Z = 55$ isotopic chain of odd–odd nuclei.

Lifetimes of excited states in the doublet bands in ^{128}Cs were measured using the Doppler shift attenuation method and were reported in [40]. The high-spin states

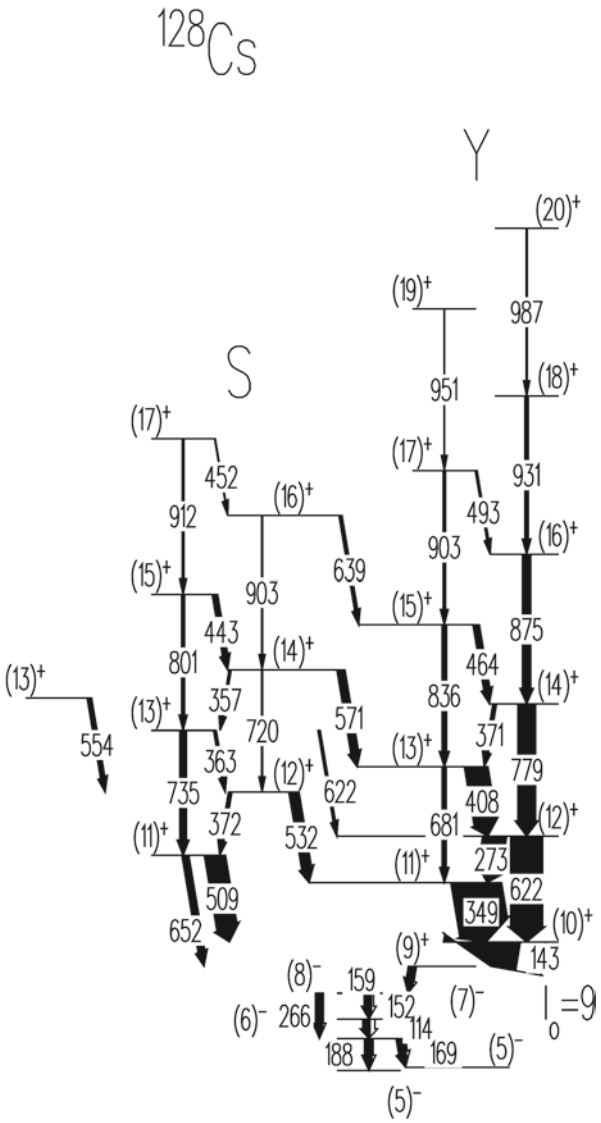

Fig. 4.5 Partial level scheme of ^{128}Cs [10] nucleus. (Figure reproduced with permission from [10])

were populated in the fusion evaporation reaction ^{122}Sn (^{10}B, 4n) at a beam energy of 55 MeV. The emitted gamma-rays were detected in coincidence in the OSIRIS II multidetector array which comprised of ten Compton-suppressed HPGe detectors. The results of lifetime measurements are given in Table 4.2.

The inband $B(M1)$ and $B(E2)$ values in bands Y and S in ^{128}Cs were determined in the work from the measured lifetimes and the branching ratios [40]. The values are shown as a function of spin in Fig. 4.22.

In the experimental results reported in [7, 30], high-spin states in the odd–odd nucleus ^{132}La were populated using the reaction ^{123}Sb (^{13}C, 4n) at a beam energy of

Table 4.2 Lifetimes of excited states in band Y and band S in ^{128}Cs [40]

J^{π}	τ (ps)	J^{π}	τ (ps)
Band Y		Band S	
$(13)^+$	$0.52^{+0.20}_{-0.10}$	$(12)^+$	$0.42^{+0.10}_{-0.08}$
$(14)^+$	$0.88^{+0.16}_{-0.14}$	$(13)^+$	$0.39^{+0.18}_{-0.11}$
$(15)^+$	$0.63^{+0.13}_{-0.11}$	$(14)^+$	$0.53^{+0.12}_{-0.10}$
$(16)^+$	$0.84^{+0.19}_{-0.17}$	$(15)^+$	$0.50^{+0.11}_{-0.09}$
$(17)^+$	$0.60^{+0.17}_{-0.12}$	$(16)^+$	$0.58^{+0.12}_{-0.10}$
$(18)^+$	$0.82^{+0.20}_{-0.14}$	$(17)^+$	$1.02^{+0.24}_{-0.20}$
$(19)^+$	$0.86^{+0.20}_{-0.15}$		
$(20)^+$	$1.06^{+0.23}_{-0.20}$		

64 MeV. The gamma-rays emitted in the decay of ^{132}La were detected in an array of six Compton-suppressed Ge detectors. A 14-element BGO multiplicity filter was also used in the experiment. A partial level scheme of ^{132}La presented in the work is shown in Fig. 4.6 (see also [40]). Two $\Delta I = 1$ rotational bands were found. Band B decays into Yrast band A by several $\Delta I = 1$ gamma-ray transitions. This pattern of decay of the interconnecting transitions is typical of the odd–odd nuclei in $A \sim 130$ mass region wherein the doublet bands are observed. The multipolarities of the inband gamma-ray transitions in the Yrast band A and those for the interconnecting transitions of energy 622, 689, 775 and 786 keV from band B to band A were de-

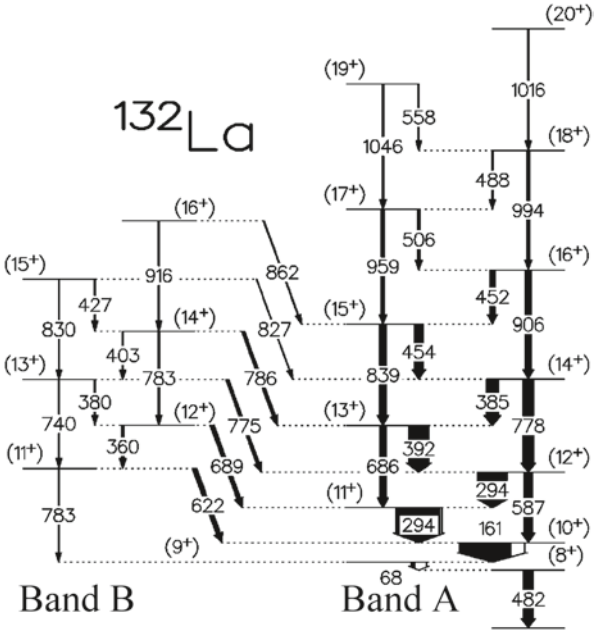

Fig. 4.6 Partial level scheme of ^{132}La [30, 40]. (Figure with permission reproduced mainly from [30])

Table 4.3 Lifetimes of excited states in band A and band B in ^{132}La [40]

J^{π}	τ (ps)	J^{π}	τ (ps)
Band A		Band B	
(12^+)	$0.68^{+0.28}_{-0.18}$	(12^+)	$0.61^{+0.19}_{-0.14}$
(13^+)	$0.53^{+0.12}_{-0.10}$	(13^+)	> 0.8
(14^+)	$0.97^{+0.23}_{-0.19}$	(14^+)	$1.15^{+0.40}_{-0.26}$
(15^+)	$0.60^{+0.16}_{-0.13}$	(15^+)	$1.4^{+0.5}_{-0.4}$
(16^+)	$0.77^{+0.14}_{-0.15}$		
(17^+)	$0.62^{+0.13}_{-0.12}$		
(18^+)	$0.54^{+0.12}_{-0.11}$		
(19^+)	$0.75^{+0.18}_{-0.14}$		
(20^+)	$1.3^{+0.4}_{-0.3}$		

termined from the DCO ratio measurements in the experiment. The interconnecting transitions of the dipole/quadrupole type were assumed to be mixed $\Delta I = 1$ $M1/E2$. Based on this, for band B the same positive parity as for band A was established. This is also a strong indicator that band B is based on the same configuration, namely, $\pi h_{11/2} \otimes \nu h_{11/2}{}^{-1}$, that was adopted for the Yrast band in [44]. The experimental data in [30] only yields relative spin assignments for the bands. Absolute spins and parity of the low energy levels of band A, have been firmly deduced in [45] from the measured angular intensity ratios and linear polarisation measurements of gamma-ray transitions de-exciting the low-spin states (all the low-spin states are not shown in the level scheme). The parity of the $I = 9$ level and levels above it could not be established firmly in the work [45].

Lifetimes of excited states in the doublet bands in ^{132}La were measured by the Doppler shift attenuation method and reported in [40]. In the work, high-spin states in this odd–odd nucleus were populated in the reaction ^{122}Sn (^{14}N, 4n) at a beam energy of 70 MeV. The emitted gamma-rays were detected in the OSIRIS II array. The lifetime values obtained in the work are given in Table 4.3.

The reduced transition probabilities, $B(M1)$ and $B(E2)$, were deduced in the work from the measured lifetimes and the gamma-ray branching ratios [40] and are shown as a function of spin in Fig. 4.22.

High-spin states in ^{134}Pr were investigated in [43 and references therein] using the reaction ^{119}Sn (^{19}F, 4n) at beam energies of 87 and 83 MeV. The gamma-rays emitted in the reaction were detected in EUROBALL IV array. The partial level scheme of ^{134}Pr obtained from the experimental data is shown in Fig. 4.7 (see also [32]). A pair of positive parity bands, band 1 (left) and band 2 (right) were found in this odd–odd nucleus. A number of strong $\Delta = 1$ and a weak $\Delta = 2$ gamma-ray transitions interconnecting band 2 to Yrast band, band 1, typical as in the odd–odd nuclei in $A \sim 130$ region, were also observed in ^{134}Pr. Multipolarities and multipole character of a large number of inband and interconnecting gamma-ray transitions were determined from linear polarisation measurements (for details see [43]). The

interconnecting transitions were found to be of $M1/E2$ type. From this experimental result, the parity of band 2 is firmly established to be the same as that of Yrast band, band 1. The assigned spins and parity of the levels in the bands have been put in parenthesis because of the uncertainty of J^{π} assignments of the low energy levels in the nucleus. The nucleon configuration $\pi h_{11/2} \otimes \nu h_{11/2}^{-1}$ has been adopted for both the partner bands.

Lifetimes of a number of excited levels in band 1 and band 2 were measured in the above-mentioned work [43], see also [42], in ^{134}Pr using the recoil distance Doppler shift and Doppler shift attenuation methods. The experimental values of lifetimes and the reduced transition probabilities, $B(M1)$ and $B(E2)$ obtained from the measured branching ratios and lifetimes are listed in Table 4.4.

4.4.2 Odd-A Nuclei

A number of spectroscopic experiments have been performed during the last couple of years using mostly the large gamma-detector arrays Euroball and the Gammasphere to search for candidate chiral doublet bands at high spins in odd-A nuclei ^{103}Rh [19, 46], ^{105}Rh [47], ^{105}Ag [48] and ^{135}Nd [49, 50].

In ^{103}Rh [46], high-spin states were populated using the fusion evaporation reaction ^{96}Zr (^{11}B, 4n) at ^{11}B beam energy of 40 MeV. The emitted gamma-rays were detected in the Gammasphere array. The level scheme obtained in this work from the experimental observables is shown in Fig. 4.8. Two $\Delta I = 1$ bands, band 3 (high-spin part) and band 4 were found in this work [46].

Table 4.4 Values of measured lifetimes and deduced reduced transition probabilities, $B(M1)$ for $\Delta=1$ and $B(E2)$ for $\Delta=2$ transitions in bands 1 and 2 in ^{134}Pr [42, 43]

J^{π}	τ (ps)	$B(M1)$ (μ_N^2)	$B(E2)$ (e^2b^2)
Band 1			
(10^+)	4.93 (15)	1.788 (57)	
(11^+)	1.614 (326)	1.235 (65)	0.268 (33)
(12^+)	1.425 (130)	0.991 (74)	0.198 (29)
(13^+)	0.904 (50)	0.568 (65)	0.151 (27)
(14^+)	0.882 (147)	0.419 (85)	0.153 (21)
(15^+)	0.608 (68)	0.290 (80)	0.148 (21)
(16^+)	0.562 (47)	0.146 (70)	0.115 (19)
(17^+)	0.422 (30)	0.194 (70)	0.108 (22)
(18^+)	0.249 (10)	0.292 (57)	0.147 (27)
Band 2			
(13^+)	1.443 (50)	0.804 (90)	0.0030 (5)
(14^+)	1.280 (50)	0.678 (100)	0.039 (19)
(15^+)	0.887 (47)	0.472 (90)	0.089 (20)
(16^+)	0.824 (52)	0.333 (75)	0.050 (18)
(17^+)	0.353 (49)	0.545 (67)	0.047 (17)

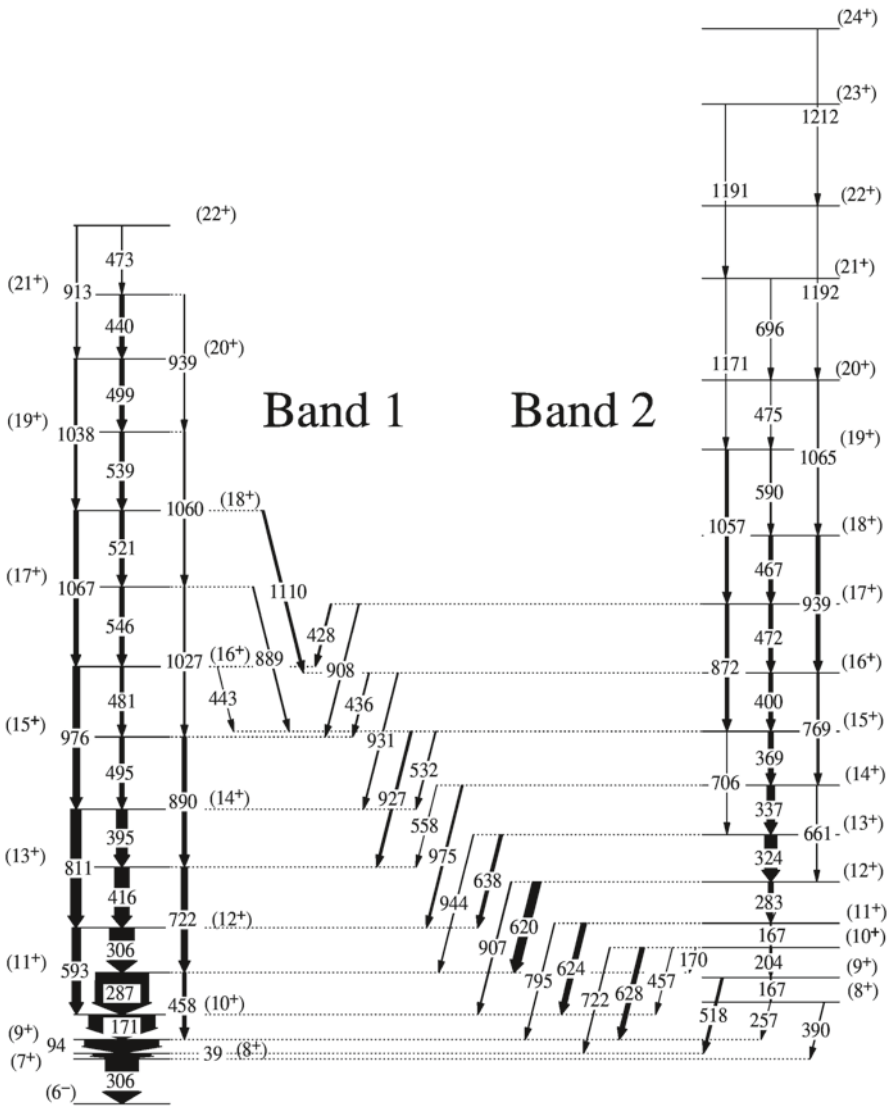

Fig. 4.7 Partial level scheme of ^{134}Pr [43 and references therein]. (Figure reproduced with permission from [43])

To determine multipolarities of gamma-rays in ^{103}Rh, DCO ratios were measured for the gamma-rays of sufficient intensities for the purpose. The 344, 377, 445 and 450 keV gamma-rays in band 4 were found to be of the dipole type and the decay out 962 and 1,088 keV transitions from this band, of quadrupole type.

In an earlier work [51] on high-spin states in ^{103}Rh, band 1 and the lower part of band 3 were only populated and assigned $\pi g_{9/2}$ and $\pi g_{9/2} \otimes \nu(h_{11/2})^2$ nucleon configurations, respectively. The spins and parity of levels in band 3 and band 4 are

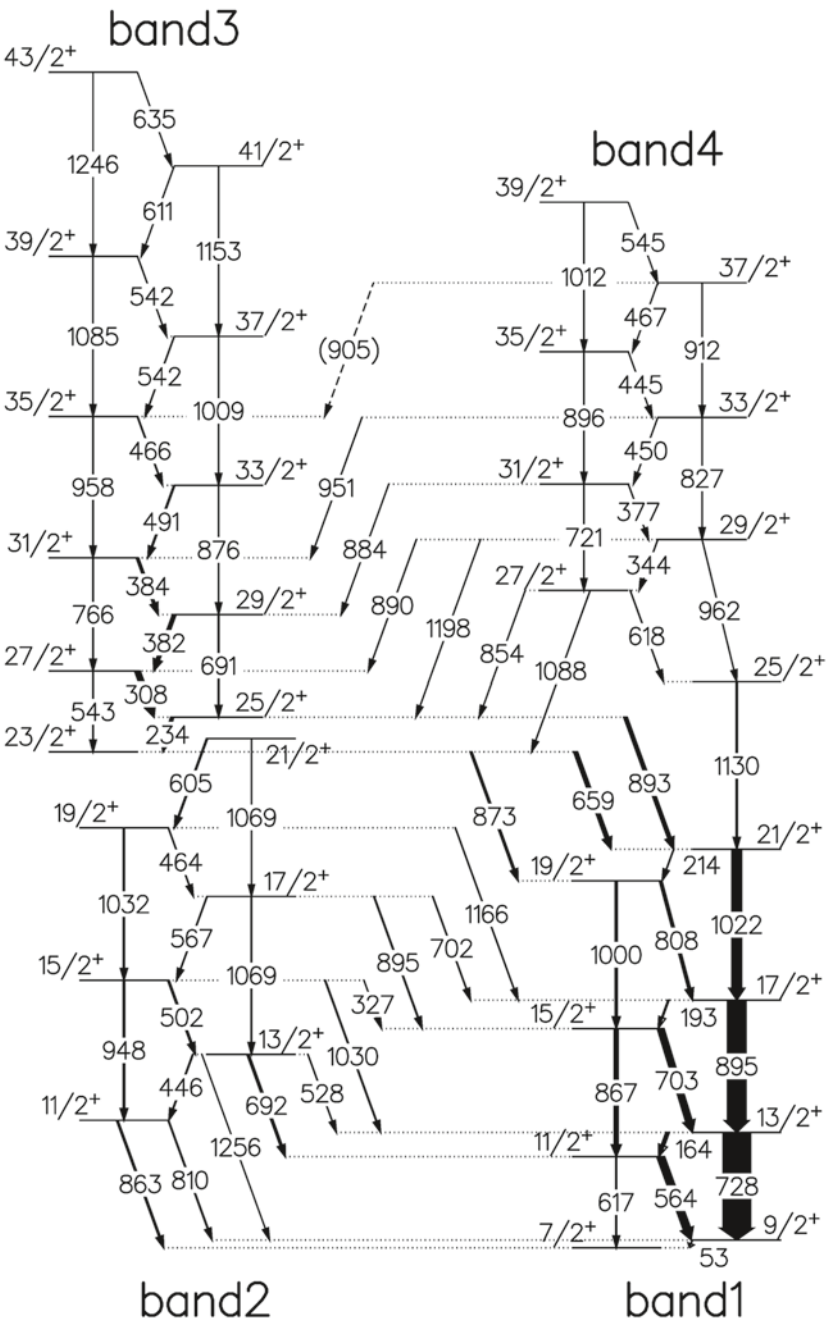

Fig. 4.8 Partial level scheme of ^{103}Rh [46]. (Figure reproduced with permission from [46])

Table 4.5 Lifetimes and the deduced $B(M1)$ and $B(E2)$ values for some levels in band 3 in ^{103}Rh [19]

J^{π} ($\hbar$)	τ (ps)	$B(M1)$ $(\mu_N)^2$	$B(E2)$ (e^2b^2)
$23/2^+$	0.99 ± 0.27	–	–
$25/2^+$	0.95 ± 0.17	2.3 ± 0.4	0.077 ± 0.014
$27/2^+$	1.0 ± 0.1	1.8 ± 0.2	0.14 ± 0.03
$29/2^+$	0.72 ± 0.23	1.2 ± 0.4	0.11 ± 0.04

determined from the experimentally deduced multipolarities of several gamma-rays [46] and the adopted J^{π} values of the relevant levels in band 1 from [51]. The typicality in band 3 and band 4 is that there are a number of interconnecting $\Delta I = 1$ and $\Delta I = 2$ gamma-ray transitions, probably of the $M1 + E2$ and $E2$ types, respectively. This indicates that these bands may have the same positive parity and same $\pi g_{9/2} \otimes \nu(h_{11/2})^2$ configuration.

Lifetime measurements by the recoil distance Doppler shift method of some of the levels in bands 1 and 3 in ^{103}Rh were reported in [19]. The results for band 3 are given in Table 4.5 together with the deduced values of $B(M1)$ and $B(E2)$.

High-spin states in ^{105}Rh were investigated in [47] using the ^{96}Zr (^{13}C, p3n) reaction at ^{13}C beam energies of 51 and 58 MeV. The emitted gamma-rays were detected in the EUROBALL IV array. The DIAMANT charged particle array [52, 53] was used to eliminate the stronger (^{13}C, xn) reaction channels. A partial level scheme of ^{105}Rh obtained from the results of the experiment is shown in Fig. 4.9. Two $\Delta I = 1$ bands, band 4 (upper part) and band 5 were newly found in the work [47]. For the determination of multipolarities and multipole character of gamma-rays, DCO ratios and linear polarisation of the gamma-rays with sufficient intensities, were measured. Mixing ratios were also determined from these measurements for the strong 466 keV $27/2^- \rightarrow 25/2^+$ (band 5 to band 1) and 821 keV $29/2^- \rightarrow 27/2^-$ (band 5 to band 4) transitions to be δ (466 keV) $= 0.24 \pm 0.08$ and δ (821 keV) $= 0.37 \pm 0.08$, respectively.

In an earlier investigation [54] in ^{105}Rh, band 1 and lower spin part of band 4 were reported and were assigned the $\pi g_{9/2}{}^{-1}$and $\pi g_{9/2}{}^{-1} \otimes \nu(h_{11/2})^2$ nucleon configurations, respectively. The spins and parity of bands 4 and 5 were assigned from the adopted J^{π} values for band 1 from [54] and the multipolarities of the interconnecting 466, 821 and 1,015 keV gamma-ray transitions determined in [47]. An $E2$ character was adopted in [47] for the 1,015 keV $\Delta I = 2$ transition. Like in ^{103}Rh, in ^{105}Rh, a similar pattern of decay of a number of interconnecting gamma-ray transitions from band 5 to band 4 with $\Delta I = 1$ $M1 + E2$ and $\Delta I = 2$ $E2$ transitions was found in the work. This indicates that bands 4 and 5 are of same positive parity and may have $\pi g_{9/2}{}^{-1} \otimes \nu(h_{11/2})^2$ nucleon configuration.

High-spin states in the odd-A nucleus ^{135}Nd were investigated in an experiment [49], using the reaction ^{110}Pd (^{30}Si, 5n) at ^{30}Si beam energy of 133 MeV. Two experiments were performed. In one experiment, emitted gamma-rays were detected in an array of three Compton-suppressed HPGe detectors. In the other experiment, the large-array Gammasphere was used. The partial level scheme of ^{135}Nd as obtained in the work is shown in Fig. 4.10.

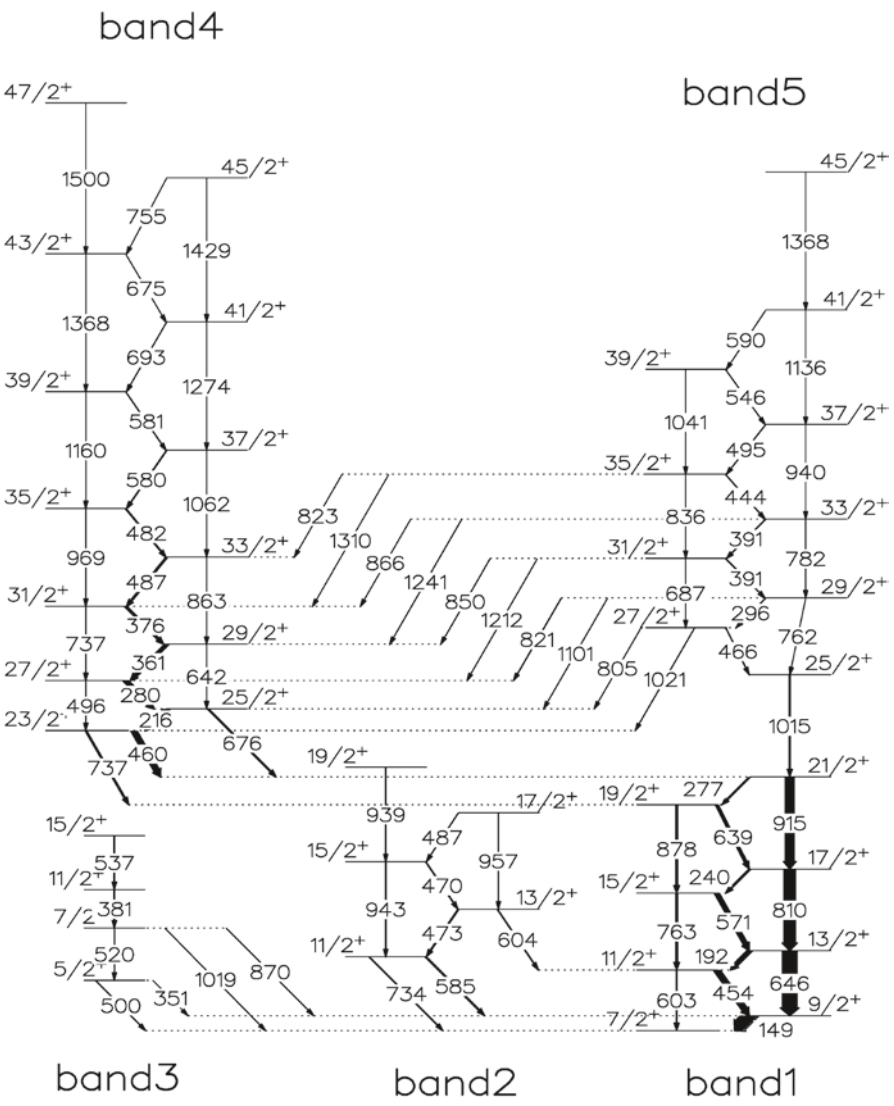

Fig. 4.9 Partial level scheme of ^{105}Rh [47]. (The figure reproduced with permission from [47])

Multipolarities of the inband and the interconnecting gamma-ray transitions were determined in the work [49] from the DCO and angular distribution measurements. The A_2/A_0 ratios obtained for the interconnecting 648 and 670 keV transitons are as follows: −(0.654 ± 0.030) and −(0.564 ± 0.022), respectively. This established their $\Delta I = 1$ character. The other linking transition of 896 keV was established to be quadrupole ($E2$) transition based on the ratio of its intensity at forward angles to that at 90°. The peculiar feature of the level scheme of ^{135}Nd is that there are a number of linking gamma-ray transitions, some out of these are strong, from band B to

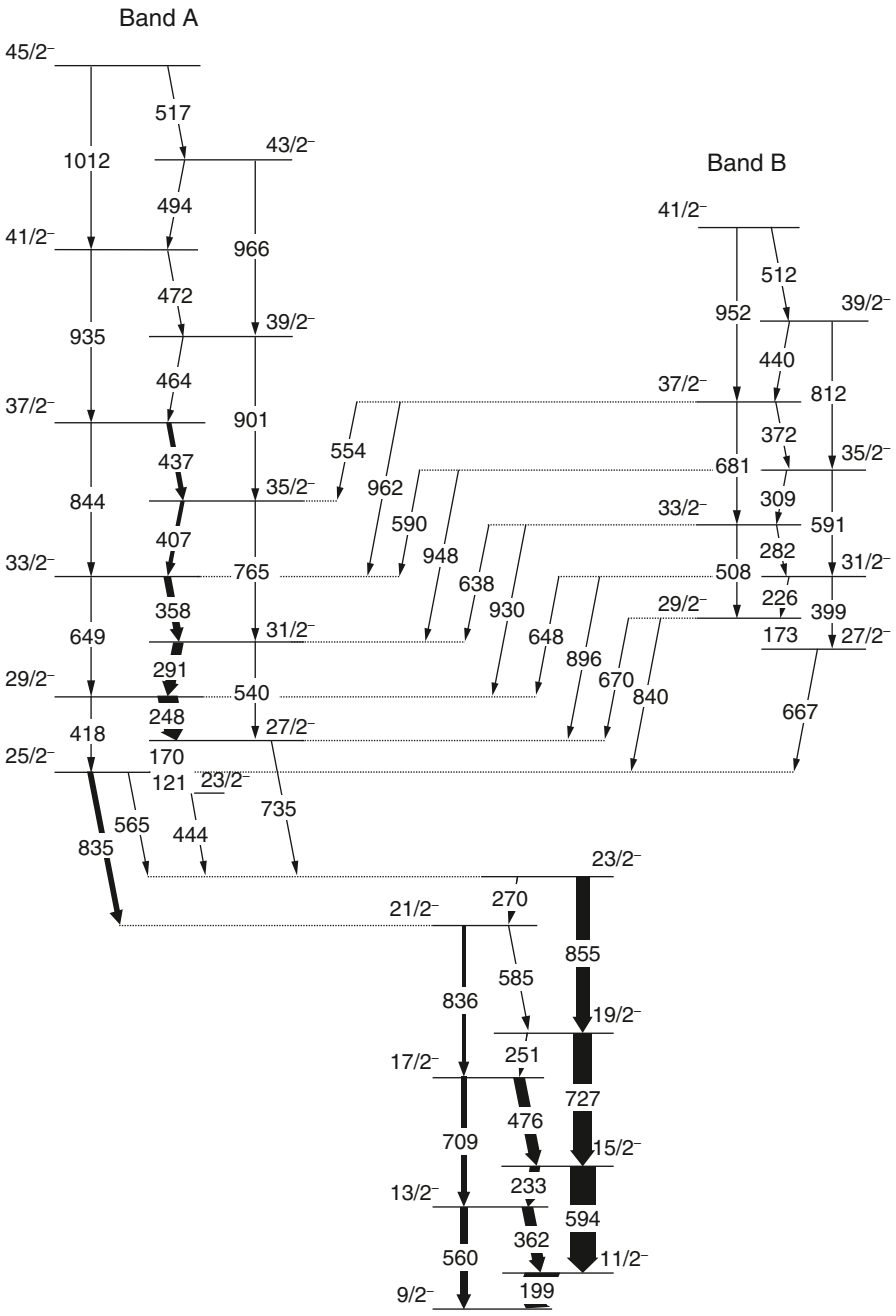

Fig. 4.10 Partial level scheme of ^{135}Nd [49, 55]. (Figure reproduced with permission from [55])

Table 4.6 Experimental values of level lifetimes and the deduced values of the reduced transition probabilities, $B(M1)$ and $B(E2)$, from lifetimes and the measured branching ratios in ^{135}Nd [50]

J^{π} ($\hbar$)	τ (ps)	$B(M1)$ $(\mu_N)^2$	$B(E2)$ (e^2b^2)
Band A			
$29/2^-$	1.00 (5)	3.2 (2)	0.32 (2)
$31/2^-$	0.75 (8)	2.5 (3)	0.32 (3)
$33/2^-$	0.44 (2)	2.2 (2)	0.32 (3)
$35/2^-$	0.28 (2)	2.4 (3)	0.32 (3)
$37/2^-$	0.23 (2)	1.7 (3)	0.32 (4)
$39/2^-$	0.22 (2)	2.1 (3)	0.13 (3)
$41/2^-$	0.18 (2)	2.1 (3)	0.19 (3)
$43/2^-$	0.16 (2)	2.0 (3)	0.21 (4)
Band B			
$31/2^-$	1.46 (2)	2.7 (3)	0.28 (3)
$33/2^-$	0.87 (6)	2.1 (2)	0.28 (3)
$35/2^-$	0.64 (5)	2.2 (2)	0.28 (4)
$37/2^-$	0.48 (3)	1.7 (2)	0.29 (4)
$39/2^-$	0.24 (4)	1.9 (3)	0.11 (3)

the Yrast band A. This, along with their determined mixed $M1/E2$ multipolarity for the $\Delta I = 1$ and $E2$ character for the $\Delta I = 2$ transitions, show that band A and band B have the same parity and same nucleon configuration. The spins and parity of levels in Yrast band A have been adopted from [56, 57] and for band B the J^{π} values are established using these values and the determined multipolarities of the inband and the interconnecting gamma-ray transitions.

The configuration assigned in [56, 57] for the Yrast band A in ^{135}Nd is $\pi(h_{11/2})^2 \otimes \nu h_{11/2}{}^{-1}$. Therefore, based on the above arguments, the configuration of band B in this nucleus is also $\pi(h_{11/2})^2 \otimes \nu h_{11/2}{}^{-1}$.

In another experiment [50], lifetimes of several levels in band A and band B in ^{135}Nd were measured using the Doppler shift attenuation method. Gamma-rays emitted in the decay of high-spin states in ^{135}Nd, populated in the ^{100}Mo (^{40}Ar, 5n) reaction, were detected in five and higher fold coincidence events, using the Gammasphere array. Analysis of data led to the determination of lifetimes of $29/2^-$ to $43/2^-$ levels in band A and $31/2^-$ to $39/2^-$ levels in band B. These values along with the reduced transition probabilities, $B(M1)$ and $B(E2)$, obtained from lifetimes and measured branching ratios are listed in Table 4.6.

4.5 Discussion

Several theoretical attempts have been made to investigate and describe the phenomenon of chirality in odd–odd nuclei. These are mainly within the framework of (1) various versions of the particle–hole–core coupling model [5, 10, 12, 13, 15, 30, 36, 43, 58–64], (2) tilted-axis cranking (TAC) model with various approaches [5, 7, 8, 28, 35, 50, 65–67] and (3) the interacting boson–fermion–fermion model [42, 43, 68–70]. A summary of the theoretical approaches is given in [3, 60, 64, 71].

In a very recent study [64], using the core–particle–hole coupling (CPHC) model to describe chiral rotation in odd–odd nuclei in $A \sim 130$ mass region, the even–even nuclear core which in general is treated as a triaxial rigid rotor in such calculations, has been considered in two extreme versions. These are, a rigid and a γ-unstable (soft) core. The single-particle configuration adopted was $\pi h_{11/2} \otimes \nu h_{11/2}^{-1}$. The justification of using the core as γ-soft comes from the microscopic calculations of potential energy surfaces which show that the $A \sim 130$ nuclei are soft to γ-deformation. Comparing the results of calculations (CPHC) for the rigid and the soft cores showed that the chiral rotational properties of the nucleus, with rigid maximally triaxial ($\gamma = 30°$) and with soft core are qualitatively very similar.

In the present section, the experimental results given in the previous section (Sect. 4.4) will be discussed in terms of the predicted fingerprints of nuclear chirality (Sect. 4.3). These fingerprints can be summarised as (1) near energy degeneracy of doublet bands, (2) spin independence of the factor $S(I)$ as a function of spin, (3) characteristic staggering of the inband $B(M1)/B(E2)$ ratios, (4) very similar $B(M1)$ and $B(E2)$ strengths for the partner bands and (5) very similar other physical properties, like, for example, aligned angular momenta.

As mentioned in Sects. 4.4.1 and 4.4.2, candidate chiral doublet bands have been observed in a number of odd–odd and odd-A nuclei. These bands are based on the following unique parity high-j configurations: (1) $\pi g_{9/2}^{-1} \otimes \nu h_{11/2}$ in $A \sim 100$ odd–odd nuclei, (2) $\pi h_{11/2} \otimes \nu h_{11/2}^{-1}$ in $A \sim 130$ odd–odd nuclei, (3) $\pi g_{9/2}^{-1} \otimes \nu (h_{11/2})^2$ in $A \sim 100$ odd-A nuclei and (4) $\pi (h_{11/2})^2 \otimes \nu h_{11/2}^{-1}$ in $A \sim 130$ odd-A nuclei. All these configurations are essentially free from admixing with nearby lower-j orbitals. For the partner bands in a nucleus to be chiral, the nuclear structure for the bands should be very similar. A stringent test for it is obtained from the reduced transition probabilities, $B(M1)$ and $B(E2)$, deduced from lifetime measurements of states in the bands. Such measurements are available in the odd–odd nuclei ^{128}Cs, ^{132}La, ^{134}Pr and in an odd-A nucleus ^{135}Nd. These nuclei will, therefore, be considered in the discussion to follow in terms of excitation energies of the doublet bands, the $S(I)$ factors, the alignments and the absolute values of $B(M1)$ and $B(E2)$ as a function of spin/rotational frequency.

Let us first consider the excitation energies of the partner bands in the above-mentioned four nuclei.

In Fig. 4.11 are plotted the excitation energies of the partner bands in ^{128}Cs [10] relative to a rigid-rotor reference, as a function of spin. The normalisation factor $1/\mathcal{I}_{\text{rigid}}$ chosen as 0.01 MeV/$\hbar^2$ [72]. The excitation energy difference of ~200 keV is almost constant between the Yrast band and the partner band. For ^{132}La [30], the excitation energies relative to a rigid-rotor reference for the doublet bands are plotted as a function of spin in Fig. 4.12. In this nucleus, the energy difference of ~390 keV between the bands is also nearly constant.

The excitation energies for the doublet bands in ^{134}Pr are plotted relative to a rigid-rotor reference, as a function of spin, in Fig. 4.13 [43]. The situation in this odd–odd nucleus is interesting. Compared to the monotonic behaviour of the partner bands in ^{128}Cs and ^{132}La nuclei, with spin (Figs. 4.11 and 4.12), the scenario in the doublet bands in ^{134}Pr is dramatic [14, 43]. The Yrast band (band 1) crosses

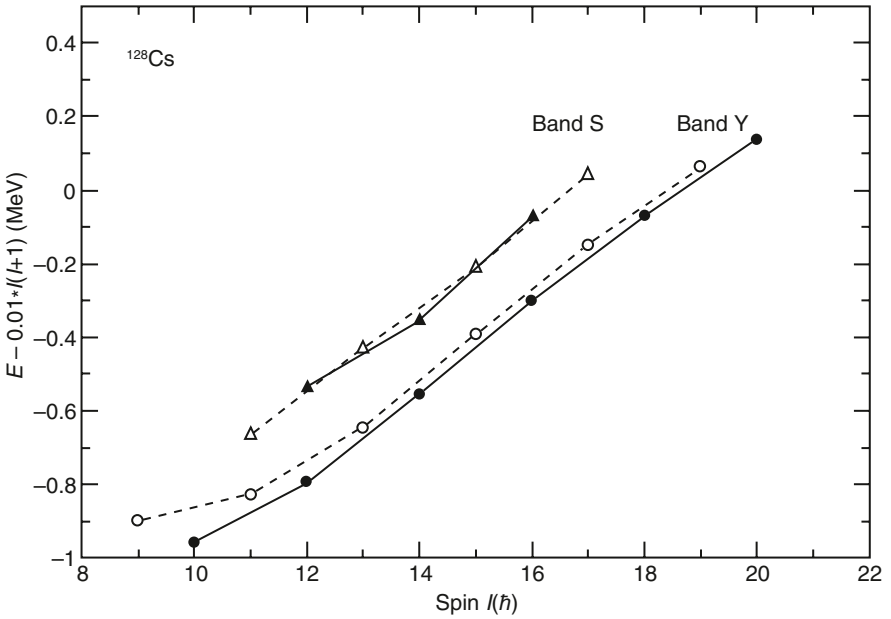

Fig. 4.11 Excitation energies of partner bands in ^{128}Cs, relative to a rigid-rotor reference. The normalisation factor is chosen as 0.01 [72]. *Open (closed) symbols* correspond to odd (even) spin states. (Data taken from [10])

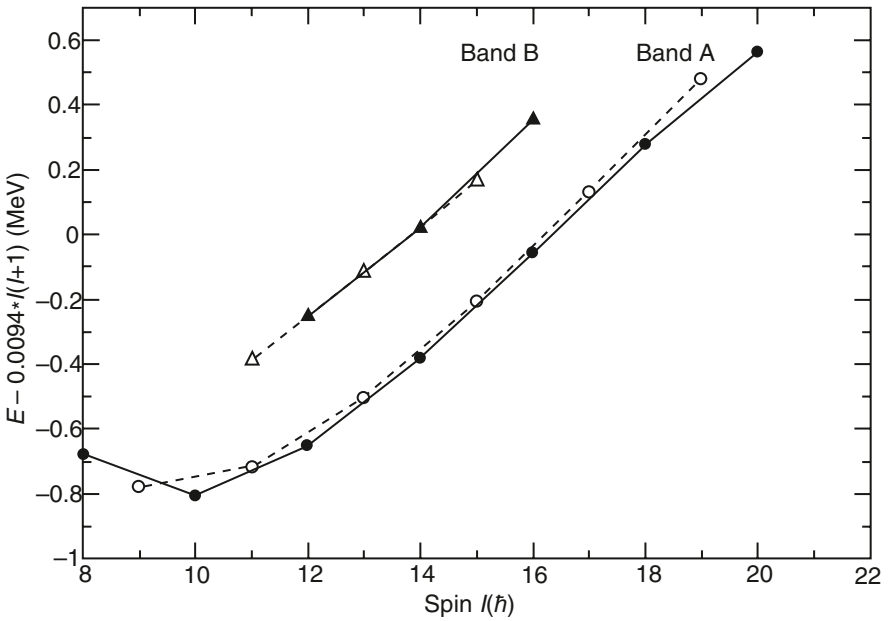

Fig. 4.12 Same as in Fig. 4.11 but for the partner bands in ^{132}La. (Data taken from [30])

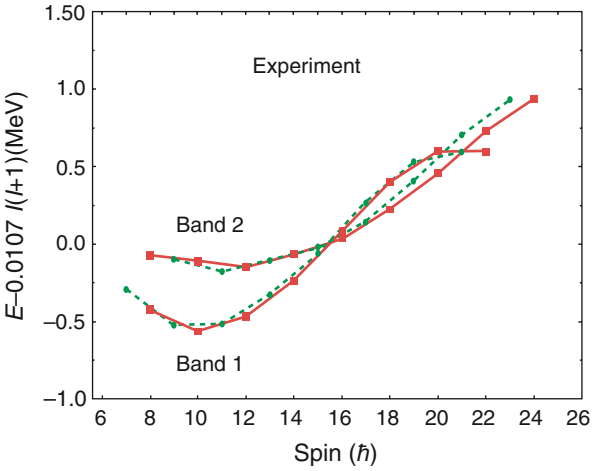

Fig. 4.13 Excitation energies of partner bands relative to a rigid-rotor reference, as a function of spin in ^{134}Pr for even and odd spin states. Normalisation factor is 0.0107 as in [14]. (Figure reproduced with permission from [43])

the partner band (band 2) between $I = 15$ and $16\hbar$. Above $I = 16\hbar$, band 2 splits in energy. As seen later in Fig. 4.20, the 2-quasiparticle (qp) band 1 becomes a 4-qp band above the bandcrossing frequency of $\hbar\omega \sim 0.46$ MeV. So, the 4-qp band 1 then crosses the energy split band 2 at $I \sim 21\hbar$.

For the doublet bands of configuration $\pi(h_{11/2})^2 \otimes \nu h_{11/2}^{-1}$ in the odd-A nucleus ^{135}Nd, the excitation energies of the partner bands relative to a rigid-rotor reference are plotted as a function of spin in Fig. 4.14 [50, 63]. As can be seen in the figure, the two bands are closest in energy ~94 keV at $I = 39/2$ before diverging in energy again.

After considering the relative excitation energies of the partner bands as a function of spin in the three odd–odd nuclei ^{128}Cs, ^{132}La and ^{134}Pr and in the odd-A nucleus ^{135}Nd, it can be inferred that in none of the nuclei, the normal energy degeneracy condition is satisfied except that in ^{135}Nd where the closest approach in energy between the bands is ~94 keV at a single spin and not in a spin range.

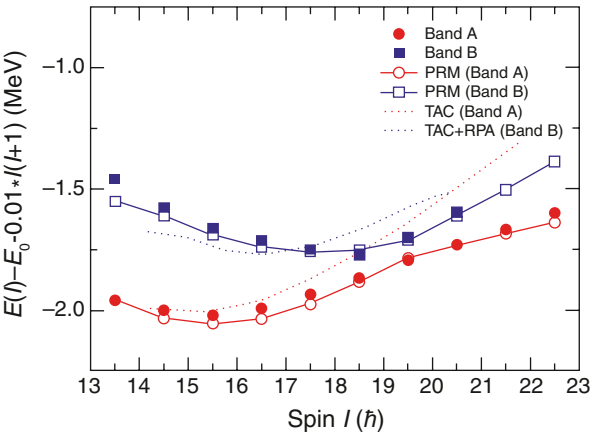

Fig. 4.14 Same as in Fig. 4.13 but for the odd-A nucleus ^{135}Nd. Normalisation factor is 0.01. E_0 is the band-head energy. *Closed (open) symbols* are the data points (theoretical predictions). The *dotted lines* are also predictions from theory. (Figure reproduced with permission from [63])

The quantity $S(I)$ (= $[E(I) - E(I-1)]/2I$) has been explained in Sect. 4.3. For a near orthogonal geometry of the valence nucleon angular momenta and the core rotational angular momentum, $S(I)$ should be essentially independent of spin. This quantity has been plotted as a function of spin for the candidate chiral doublet bands in the odd–odd nuclei ^{128}Cs, ^{132}La, ^{134}Pr and for similar bands in the odd-A nucleus ^{135}Nd and are shown in Figs. 4.15, 4.16, 4.17 and 4.18, respectively. For ^{128}Cs (see Fig. 4.5 for level scheme), there is staggering of the $S(I)$ values for the Yrast band Y, although its amplitude decreases with increasing spin. For the partner band S, the behaviour of $S(I)$ is different and the staggering vanishes for higher spins. In ^{132}La (see Fig. 4.6 for level scheme), for the Yrast band A, staggering of $S(I)$ with spin exists. This effect is almost absent for the partner band B. In ^{134}Pr (see Fig. 4.7 for level scheme), the energy staggering in band 1 at low spins is larger than in band 2. Above spin $I = 18$, the staggering in $S(I)$ of band 2 becomes larger while that in band 1 becomes very small. The behaviour of $S(I)$ with spin in ^{128}Cs, ^{132}La and ^{134}Pr is different between the doublet bands. The condition for the doublet bands to be chiral is that not only $S(I)$ should be independent of spin but the behaviour of the partners should be very similar. Therefore, according to these criteria, the doublet bands in the odd–odd nuclei ^{128}Cs, ^{132}La and ^{134}Pr do not qualify to be chiral partner bands.

The behaviour of $S(I)$ as a function of spin for the doublet bands in the odd-A nucleus ^{135}Nd (see Fig. 4.10 for level scheme) based on the $\pi(h_{11/2})^2 \otimes \nu h_{11/2}^{-1}$ configuration is quite different than in the odd–odd nuclei discussed above. The plot of the quantity $S(I)$ of the partner bands in ^{135}Nd, as a function of spin, is shown in Fig. 4.18. No significant staggering is observed for both the partner bands in this nucleus. In band A, for $I > 35/2$, $S(I)$ is practically independent of spin, a condition

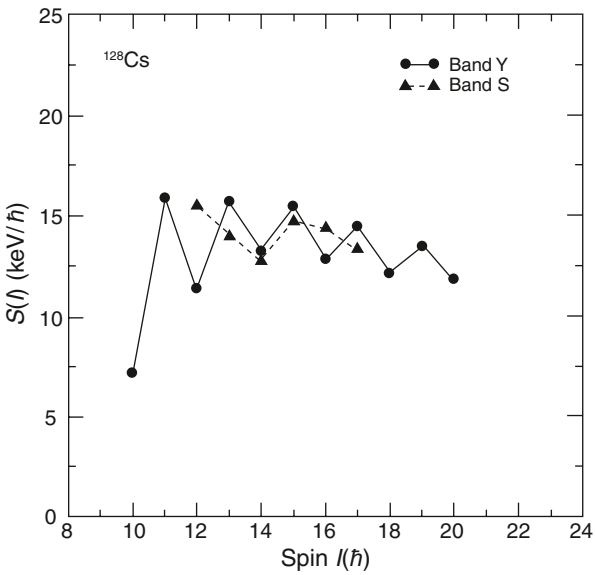

Fig. 4.15 Plot of $S(I)$ (= $[E(I) - E(I-1)]/2I$) as a function of spin for the doublet bands in the odd–odd nucleus ^{128}Cs. (Data taken from [10])

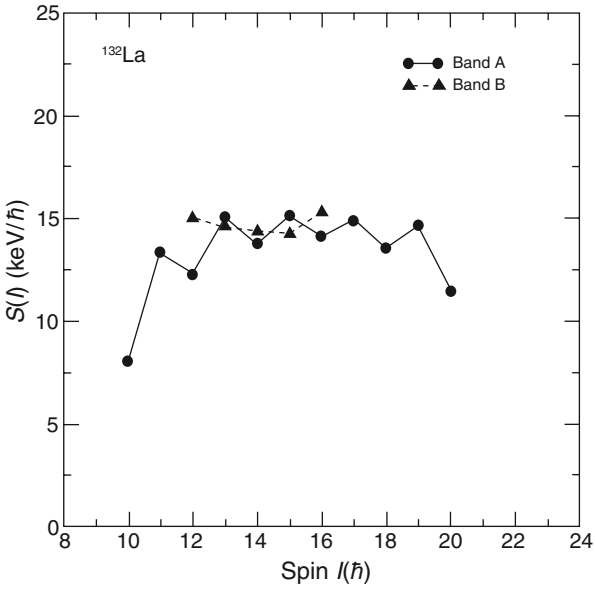

Fig. 4.16 Plot of $S(I)$ $(= [E(I) - E(I-1)]/2I)$ as a function of spin for the doublet bands in the odd–odd nucleus ^{132}La. (Data taken from [30] and Fig. 4.6)

required for static chirality. In the partner band B, although $S(I)$ varies smoothly with spin but it increases with increasing spin. This behaviour is at variance with that depicted by band A. But the scenario is closest to that expected for chiral bands. Therefore, the doublet bands in ^{135}Nd may qualify to be the chiral partner bands.

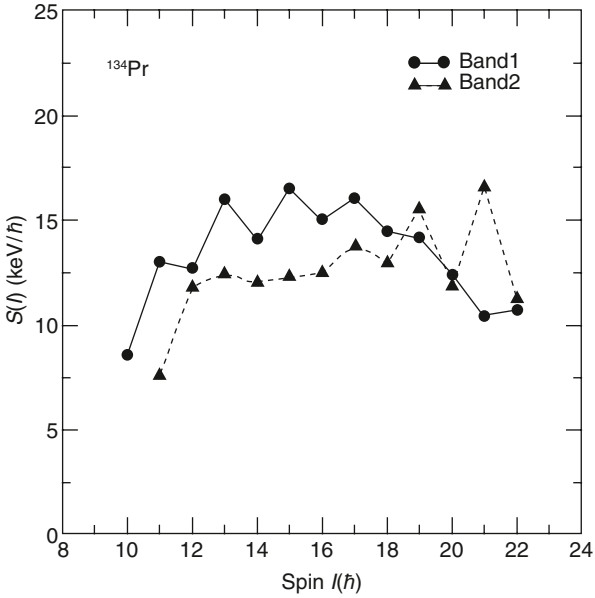

Fig. 4.17 Plot of $S(I)$ $(= [E(I) - E(I-1)]/2I)$ as a function of spin for the doublet bands in the odd–odd nucleus ^{134}Pr. (Data taken from [43])

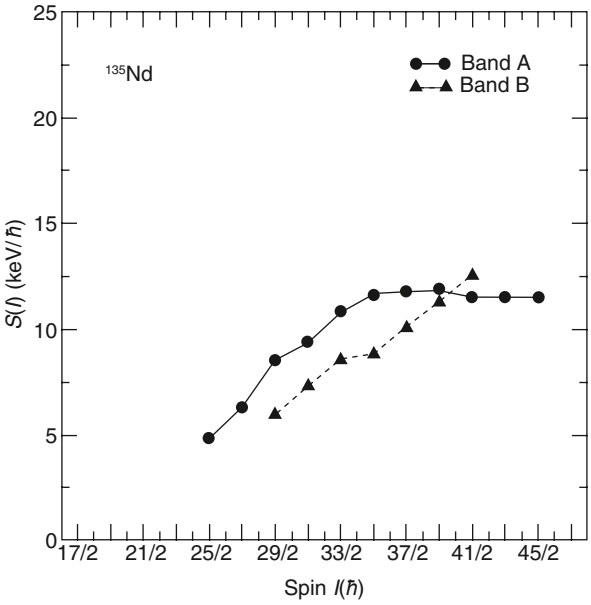

Fig. 4.18 Plot of $S(I)$ $(= [E(I) - E(I-1)]/2I)$ as a function of spin for the doublet bands in the odd-A nucleus ^{135}Nd. (Data taken from [49, 55])

Plots of particle alignment, i_x as a function of rotational frequency, $\hbar\omega$, for the candidate chiral bands based on the $\pi h_{11/2} \otimes \nu h_{11/2}^{-1}$ configuration in ^{128}Cs [40], ^{132}La [40] and ^{134}Pr [14] nuclei are shown in Figs. 4.19 and 4.20. In ^{128}Cs and ^{132}La, the alignments show a similar behaviour. In contrast, in ^{134}Pr, in the rotational frequency range $0.35 < \hbar\omega < 0.5$ MeV (spin range $14 < I < 18$), alignment difference

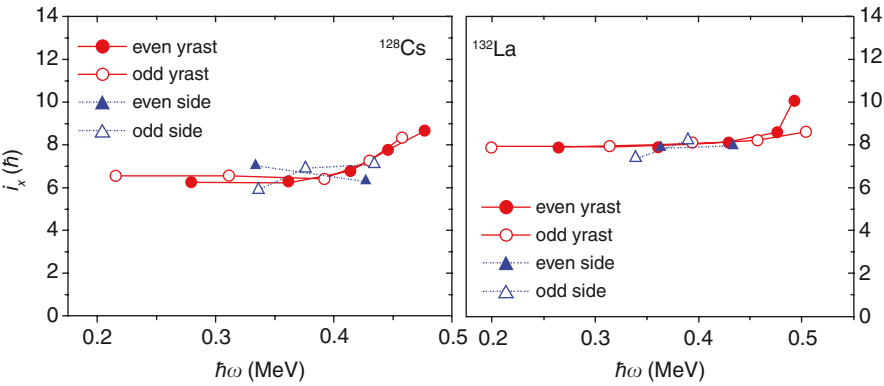

Fig. 4.19 Particle alignment, i_x, as a function of rotational frequency, $\hbar\omega$, for the doublet bands in ^{128}Cs and ^{132}La. The Harris parameters used were as follows: for ^{128}Cs, $\mathcal{I}_0 = 16\hbar^2$ MeV^{-1}, $\mathcal{I}_1 = 33\hbar^4$ MeV^{-3} and for ^{132}La, $\mathcal{I}_0 = 11\hbar^2$ MeV^{-1}, $\mathcal{I}_1 = 37\hbar^4$ MeV^{-3} [40]. (Figure reproduced with permission from [40])

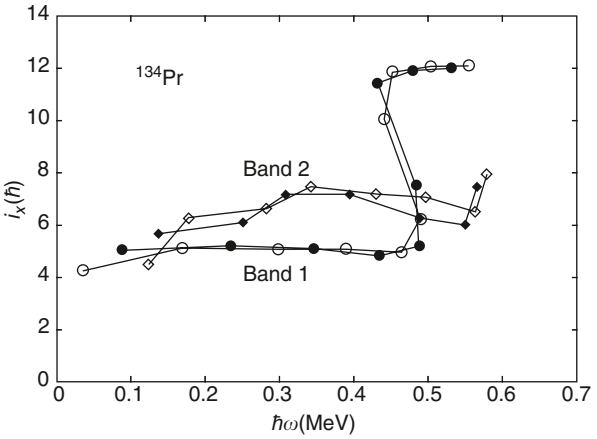

Fig. 4.20 Particle alignment, i_x, as a function of rotational frequency, $\hbar\omega$, for the doublet bands in ^{134}Pr. *Filled (open) symbols* are for $\alpha = 0$ (1) bands. The Harris parameters used were $\mathcal{I}_0 = 15\hbar^2$ MeV^{-1}, $\mathcal{I}_1 = 30\hbar^4$ MeV^{-3}. (Figure reproduced with permission from [14])

between the bands is ~2$\hbar$. This difference is rather large and the partner bands in this nucleus cannot be considered to have a very similar structure.

Let us look at the situation of particle alignment, i_x, in the candidate chiral doublet bands based on $\pi(h_{11/2})^2 \otimes \nu h_{11/2}^{-1}$ configuration in the odd-A nucleus ^{135}Nd. This is shown as a function of rotational frequency, in Fig. 4.21 [73]. The maximum alignment difference between the two bands is $\gtrsim 1\hbar$. This is a borderline case for similar alignment.

Let us consider the reduced transition probabilities, $B(M1)$ and $B(E2)$, as deduced from lifetime measurements in the odd–odd ^{128}Cs [39–41], ^{132}La [39–41] and

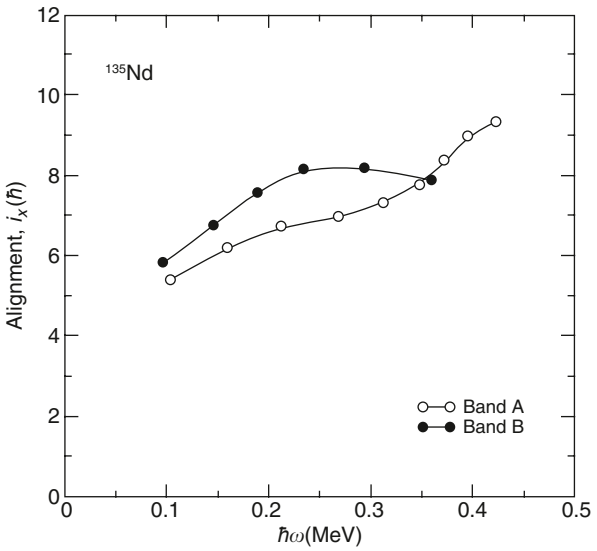

Fig. 4.21 Particle alignment, i_x, as a function of rotational frequency, $\hbar\omega$, for the partner bands, *band A* (○) and *band B* (●) in ^{135}Nd. The Harris parameters used were $\mathcal{I}_0 = 17\hbar^2$ MeV^{-1}, $\mathcal{I}_1 = 25\hbar^4$ MeV^{-3}. (Figure reproduced with permission from [73])

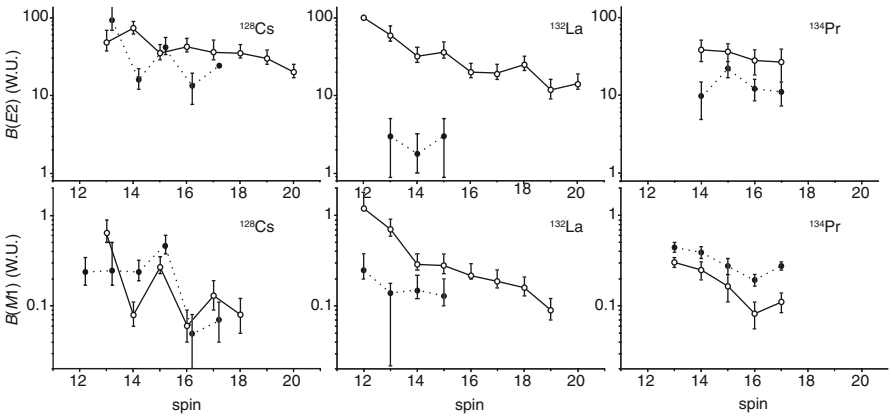

Fig. 4.22 Experimentally deduced values of $B(E2)$ (*upper panel*) and $B(M1)$ (*lower panel*) as a function of spin for the partner bands (Yrast: *open symbols*, partner: *closed symbols*) in odd–odd ^{128}Cs, ^{132}La and ^{134}Pr nuclei [40, 42, 43]. (Figure reproduced with permission from [4])

^{134}Pr [42, 43] nuclei (see also Sect. 4.4.1). The values of $B(M1)$ and $B(E2)$ in these nuclei are plotted in Fig. 4.22 [4]. From this figure, it is found that these values in the partner bands in ^{132}La and ^{134}Pr are different. In ^{128}Cs, although the $B(M1)$ and $B(E2)$ values in the partner bands are different but in comparison to ^{132}La and ^{134}Pr, the agreement is better. The characteristic staggering pattern in $B(M1)$ values is seen only in ^{128}Cs. The overall behaviour of the reduced transition probabilities as a function of spin clearly indicates that the intrinsic structures of the partner bands are not similar in ^{132}La and ^{134}Pr nuclei. Therefore, in the present definition, these doublet bands cannot qualify as chiral partners.

In Fig. 4.22, for ^{134}Pr, only those values were plotted for which data were available for both the partner bands. The full range of deduced $B(M1)$ and $B(E2)$ values from experimental data for this nucleus are shown in Fig. 4.23 [43].

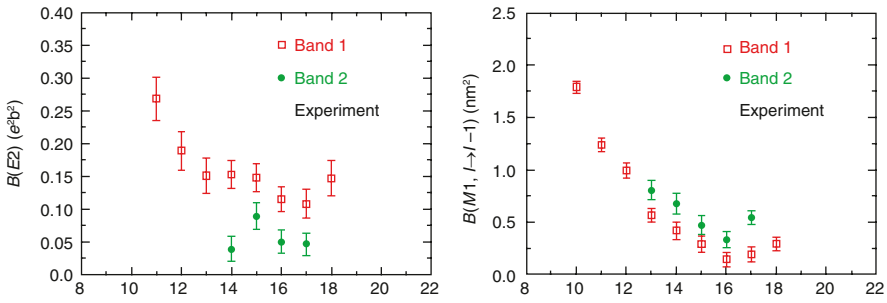

Fig. 4.23 Experimentally deduced values of $B(E2)$ and $B(M1)$ from lifetime measurements in the partner bands in ^{134}Pr [43], as a function of spin. Note the difference of units on the Y-axes in this and Fig. 4.22. (Figure reproduced with permission from [43])

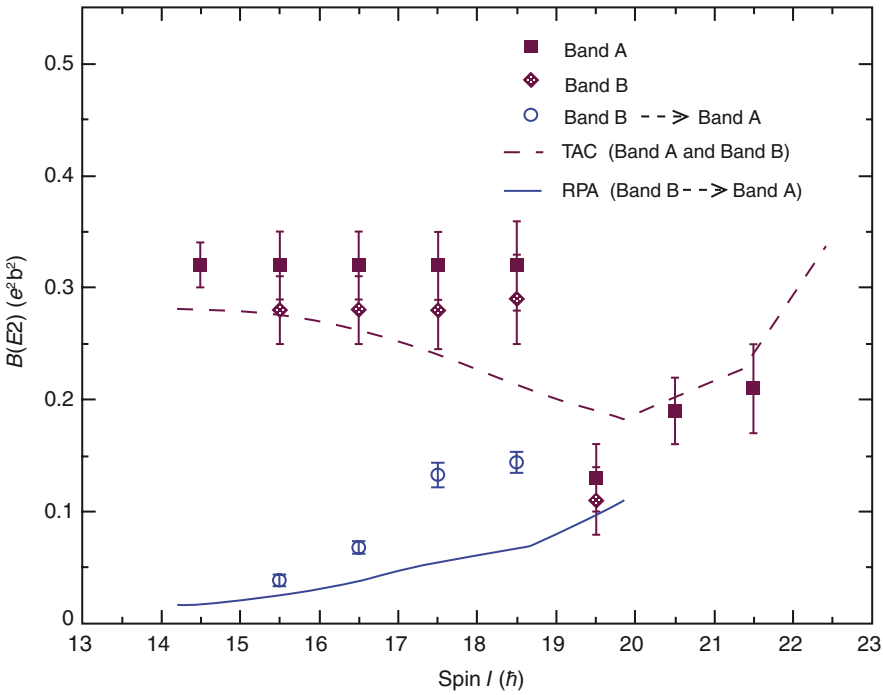

Fig. 4.24 Experimentally deduced values of reduced transition probability $B(E2)$ for the partner bands, *band A* and *band B* in ^{135}Nd [50]. (Figure with permission reproduced in part from [50])

In ^{135}Nd, the reduced transition probabilities, $B(M1)$ and $B(E2)$, were deduced form lifetime measurements of levels in band A and band B (see Fig. 4.10 for level scheme). These values are listed in Table 4.6 in Sect. 4.4.2 and plots of $B(E2)$ and $B(M1)$ as a function of spin are shown in Figs. 4.24 and 4.25, respectively. It is found that within the experimental uncertainties, the $B(E2)$ and $B(M1)$ values as a function of spin are essentially the same for the doublet bands in this nucleus. This clearly establishes that the intrinsic structure of the doublet bands in ^{135}Nd is very similar. In the $B(M1)$ values, with increasing spin, the characteristic staggering in values is also noticed. These results establish a pure chiral character for these partner bands of configuration $\pi(h_{11/2})^2 \otimes \nu h_{11/2}^{-1}$ in ^{135}Nd. These findings are of considerable importance.

In the above discussion, the partner bands in the odd–odd ^{128}Cs, ^{132}La and ^{134}Pr nuclei and in the odd-A ^{135}Nd nucleus were considered in terms of their excitation energies, the quantity $S(I)$, particle alignments, i_x, and the reduced transition probabilities, $B(M1)$ and $B(E2)$. These considerations strongly indicate that the best candidate for static nuclear chirality are the doublet bands in ^{135}Nd nucleus.

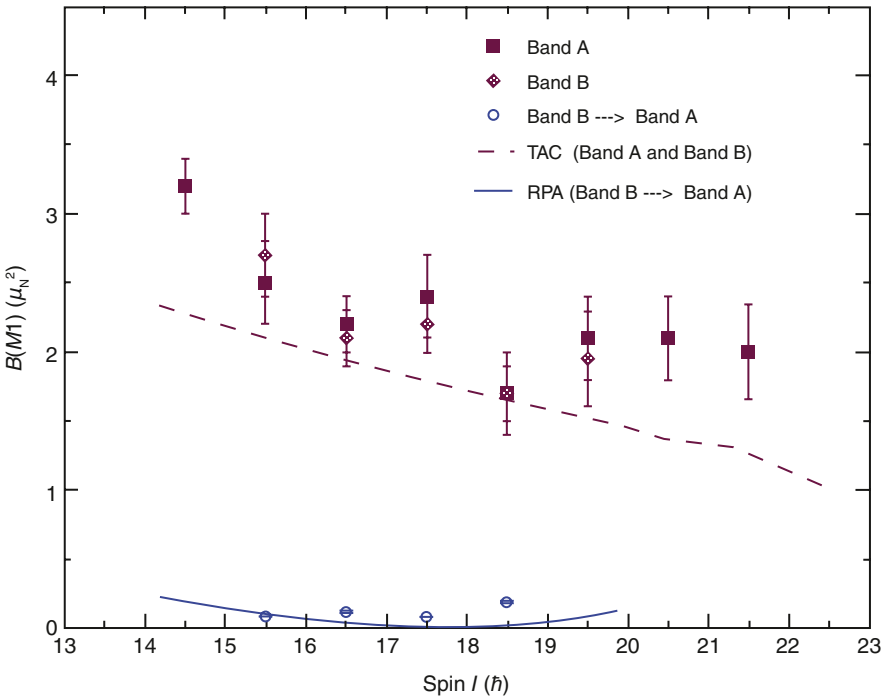

Fig. 4.25 Experimentally deduced values of reduced transition probability $B(M1)$ for the partner bands, *band A* and *band B* in ^{135}Nd [50]. (Figure with permission reproduced in part from [50])

4.6 Conclusions and Perspectives

During the last about a decade or so, in nuclear structure physics, a sizable effort, both experimental and theoretical, has gone into search for the possible occurrence of static chirality at moderate spins in deformed ($\beta_2 \sim 0.22$) nuclei in different mass regions, $A \sim 100$, ~135 and ~188.

In Sect. 4.5, the experimental results in three odd–odd nuclei ^{128}Cs, ^{132}La, ^{134}Pr and one odd-A nucleus ^{135}Nd were discussed. The basis, as mentioned earlier, for choosing these cases for discussion, is that lifetime measurements of states in the partner bands are available in these nuclei. The reduced transition probabilities, $B(M1)$ and $B(E2)$, deduced from lifetimes are compared for the partner bands. This is the most crucial test for the occurrence of chirality as it tells whether nuclear structure in the partner bands is very similar or not. Such comparisons have shown that the best candidate chiral bands for the occurrence of stable chirality are in odd-A nucleus ^{135}Nd. But for the phenomenon to exist, it should be wide spread, in a number of nuclei in different mass regions. To achieve this aim, lifetime measure-

ments in other nuclei where the doublet bands are present, are very much required. Search for partner bands in nuclei in other mass regions will be helpful.

References

1. P. Joshi et al., J. Phys. G: Nucl. Part. Phys. 31, S 1895 (2005).
2. T. Koike et al., J. Phys. G: Nucl. Part. Phys. 31, S 1741(2005).
3. J. Meng et al., Mod. Phys. Lett. A 23, 2560 (2008).
4. E. Grodner et al., Acta Phys. Pol. B 39, 531 (2008).
5. S. Frauendorf and J. Meng, Nucl. Phys. A 617, 131 (1997).
6. A. Bohr and B. R. Mottelson, in *Nuclear Structure,* Vol 2 (Benjamin, New York, 1975).
7. K. Starosta et al., Phys. Rev. Lett. 86, 971 (2001).
8. V. Dimitrov, S. Frauendorf. and F. Donev, Phys. Rev. Lett. 84, 5732 (2000).
9. C. M. Petrache et al., Z. Phys. A 344, 227 (1992); Nucl. Phys. A 597, 106 (1996).
10. T. Koike et al., Phys. Rev. C 67, 044319 (2003).
11. C. Vaman et al., Phys. Rev. Lett. 92, 032501 (2004).
12. T. Koike et al., Phys. Rev. Lett. 93, 172502 (2004).
13. J. Peng et al., Phys. Rev. C 68, 044324 (2003).
14. C. M. Petrache et al., Phys. Rev. Lett. 96, 112502 (2006).
15. B. Qi et al., Phys. Rev. C 79, 041302 (R) (2009).
16. P. Joshi et al., Eur. Phys. J. A 24, 23 (2005).
17. J. Gizon et al., Nucl. Phys. A 658, 97 (1999).
18. Pankaj Joshi, priv. comm.
19. T. Suzuki et al., Phys. Rev. C 78, 031302 (R) (2008).
20. P. Joshi et al., Phys. Lett. B 595, 135 (2004).
21. P. Joshi et al., Phys. Rev. Lett. 98, 102501 (2007) and references therein.
22. A. M. Bizzeti - Sona et al., Z. Phys. A 352, 247 (1995).
23. N. Fotiades et al., Phys. Rev. C 67, 064304 (2003).
24. M.- G. Porquet et al., Eur. Phys. J. A 15, 463 (2002).
25. Shouyu Wang et al., Phys. Rev. C 74, 017302 (2006).
26. T. Koike et al., Phys. Rev. C 63, 061304 (R) (2001).
27. A. J. Simons et al., J. Phys. G. Nucl. Part. Phys. 31, 541 (2005).
28. G. Rainovski et al., Phys. Rev. C 68, 024318 (2003).
29. G. Rainovski et al., J. Phys. G. Nucl. Part. Phys. 29, 2763 (2003).
30. K. Starosta et al., Phys. Rev. C 65, 044328 (2002).
31. R. A. Bark et al., Nucl. Phys. A 691, 577 (2001).
32. K. Starosta, in *Nuclei at the Limits,* eds., T. L. Khoo and D. Sewerynaik, AIP Conf. Proc. No.764 (AIP, New York, 2005) p.77.
33. C. W. Beausang et al., Phys. Rev. C 36, 1810 (1987).
34. C. W. Beausang et al., Nucl. Phys. A 682, 394c (2001).
35. A. A. Hecht et al., Phys. Rev. C 63, 051302 (R) (2001).
36. D. J. Hartley et al., Phys. Rev. C 64, 031304 (R) (2001).
37. D. L. Balabanski et al., Phys. Rev. C 70, 044305 (2004).
38. E. A. Lawrie et al., Phys. Rev. C 78, 021305 (R) (2008).
39. J. Srebrny et al., Acta Phys. Pol. B 36, 1063 (2005).
40. E. Grodner et al., Phys. Rev. Lett. 97, 172501 (2006).
41. E. Grodner et al., Intl. J. Mod. Phys. E 15, 548 (2006).
42. D. Tonev et al., Phys. Rev. Lett. 96, 052501 (2006).
43. D. Tonev et al., Phys. Rev. C 76, 044313 (2007).
44. J. R. B. Oliveira et al., Phys. Rev. C 39, 2250 (1989).

45. J. Timár et al., Eur. Phys. J. A 16, 1 (2003).
46. J. Timár et al., Phys. Rev. C 73, 011301 (R) (2006).
47. J. Timár et al., Phys. Lett. B 598, 178 (2004).
48. J. Timár et al., Phys. Rev. C 76, 024307 (2007).
49. S. Zhu et al., Phys. Rev. Lett. 91, 132501 (2003).
50. S. Mukhopadhyay et al., Phys. Rev. Lett. 99, 172501 (2007).
51. H. Dejbakhsh et al., Phys. Rev. C 37, 621 (1988).
52. J. N. Scheurer et al., Nucl. Instrum. Methods. A 385, 501 (1997).
53. J. Gál et al., Nucl. Instrum. Methods. A 516, 502 (2004).
54. F. R. Espinoza-Quinones et al., Phys. Rev. C 55, 2787 (1997).
55. U. Garg., priv. Comm. (October 2009).
56. W. F. Piel et al., Phys. Rev. C 35, 959 (1987).
57. E. M. Beck et al., Phys. Rev. Lett. 58, 2182 (1987).
58. M. S. Fetea et al., J. Phys. G: Nucl. Phys. 31, S 1847 (2005).
59. S. Y. Wang et al., Phys. Rev. C 75, 024309 (2007).
60. S. Q. Zhang et al., Phys. Rev. C 75, 044307 (2007).
61. S. Y. Wang et al., Phys. Rev. C 77, 034314 (2008).
62. S. Y. Wang et al., Chin. Phys. C 33, Suppl. 1, 37 (2009).
63. B. Qi et al., Phys. Lett. B 675, 175 (2009).
64. Ch. Droste et al., Eur. Phys. J. A 42, 79 (2009).
65. V. I. Dimitrov et al., Phys. Rev. C 62, 024315 (2000).
66. P. Olbratowski et al., Phys. Rev. Lett. 93, 052501 (2004).
67. P. Olbratowski et al., Phys. Rev. C 73, 054308 (2006).
68. S. Brant et al., Phys. Rev. C 69, 017304 (2004).
69. S. Brant et al., Phys. Rev. C 78, 034301 (2008).
70. S. Brant et al., Phys. Rev. C 79, 054326 (2009).
71. K. Higashiyama et al., Phys. Rev. C 72, 024315 (2005).
72. A. V. Afanasjev et al., Phys. Repts. 322, 1 (1999).
73. U. Garg, priv. comm. (January, 2010).

Partial List of Books, Review and Some Other Articles Mainly in High Spin Nuclear Structure Physics

Note: The references for Superdeformation, Hyperdeformation, Band termination and Nuclear isomers and other review articles in high spin physics listed below may be useful and handy for the readers, as the present monograph includes discussion only on a limited number of topics on the subject.

Books

1. Nuclear Structure Vol. I: Single – particle motion by Aage Bohr and Ben R. Mottelson, World Scientific (1998). (First Edition W.A. Benjamin (1969)).
2. Nuclear Structure Vol. II: Nuclear deformations by Aage Bohr and Ben R. Mottelson. World Scientific (1998). (First Edition W.A. Benjamin (1975)).
3. The electromagnetic interaction in nuclear spectroscopy edited by W.D. Hamilton, North Holland (1975).
4. In-beam gamma-ray spectroscopy by H. Morinaga and T. Yamazaki, North Holland (1976).
5. Fast nuclear rotation, Z. Szymanski, Clarendon Press, Oxford (1983).
6. Gamma-ray and electron spectroscopy in nuclear physics by H. Ejiri and M.J.A. de Voigt, Clarendon Press, Oxford (1989).
7. Shapes and shells in nuclear structure by Sven Gösta Nilsson and Ingemar Ragnarsson, Cambridge University Press (1995).
8. Nuclear structure from a simple perspective, Second Edition by R.F. Casten, Oxford University Press (2000).
9. Basic ideas and concepts in nuclear physics – An introductory approach, Third Edition by K. Heyde, Taylor & Francis (2004).
10. Handbook of nuclear properties, Eds. Dorin Poenaru and Walter Greiner, Clarendon Press, Oxford (2008).
11. Fundamentals of nuclear models by David J. Rowe and John L. Wood, World Scientific (2010).

Superdeformation

1. Superdeformed shapes at high angular momentum, P.J. Nolan and P.J. Twin, Ann. Rev. Nucl. Part. Sci., 38, 533 (1988).
2. Structure of superdeformed bands in the A ≈ 150 mass region, W. Nazarewicz, R. Wyss and A. Johnson, Nucl. Phys. A 503, 285 (1989).

S. C. Pancholi, *Exotic Nuclear Excitations,* Springer Tracts in Modern Physics 242,
DOI 10.1007/978-1-4419-8038-0, © Springer Science+Business Media, LLC 2011

3. Superdeformations – A theoretical overview, Sven Åberg, Nucl. Phys. A 520, 35c (1990).
4. Spin alignment in superdeformed rotational bands, F.S. Stephens, Nucl. Phys. A 520, 91c (1990).
5. Nuclear shapes in mean field theory, S. Åberg, H. Flocard and W. Nazarewicz, Ann. Rev. Nucl. Part. Sci., 40, 439 (1990).
6. Superdeformed nuclei, Robert V.F. Janssens and Teng Lek Khoo, Ann. Rev. Nucl. Part. Sci., 41, 321 (1991).
7. Nuclear superdeformation at high spins, J. Dudek, Prog. Part. Nucl. Phys., 28, 131 (1992).
8. Identical bands in deformed and superdeformed nuclei, C. Baktash, B. Hass and W. Nazarewicz, Ann. Rev. Nucl. Part. Sci., 45, 485 (1995).
9. Identical superdeformed bands, B. Haas, Prog. Part. Nucl. Phys., 38, 1 (1997).
10. Tunneling from super – to normal – deformed minima in nuclei, Teng Lek Thoo, *Tunneling in Complex Systems,* Proc. from the Institute for Nuclear Theory, ed., Steven Tomsovic, Vol. 5, p.229 (World Scientific 1998).
11. Nuclear superdeformation data tables, X.-L. Han and C.-L. Wu, At. Data and Nucl. Data Tables, 73, 43 (1999).
12. Collective excitations in the superdeformed well, F. Hannachi et al., Acta Phys. Pol. 32, 1083 (2001).
13. Table of superdeformed nuclear bands and Fission isomers: Third edition, Balraj Singh, Roy Zywina and Richard B. Firestone, Nucl. Data Sheets, 97, 241 (2002).

Hyperdeformation (Additional Literature Search Recommended)

1. Search for the nuclear hyperdeformation: Motivations and new strategies, J. Dudek, N. Schunck and N. Dubray, Acta Phys. Pol. 36, 975 (2005).
2. Spectroscopy of strongly deformed nuclei – From super to hyperdeformation, P. Fallon, Acta Phys. Pol. 36, 1003 (2005).
3. Search for hyperdeformation, H. Hübel, Acta Phys. Pol. 36, 1015 (2005).
4. Light charged particles as a gateway to hyperdeformation, B. Herskind et al., Acta Phys. Pol. 38, 1421 (2007).

Band Termination

1. Properties of terminating bands in nuclei, Ingemar Ragnarsson, Zheng Xing, Tord Bengtsson and Mark A. Riley, Phys. Scr. 34, 651 (1986).
2. Termination of rotational bands: Disappearance of quantum many-body collectivity, A.V. Afanasjev, D.B. Fossan, G.J. Lane and I. Ragnarsson, Physics Reports, 322, 1 (1999).

Nuclear Isomers

1. Energy traps in atomic nuclei, Philip Walker and George Dracoulis, NATURE, 399, 35 (6 May 1999).

2. Exotic isomers in deformed atomic nuclei, P.M. Walker and G.D. Dracoulis, Hyperfine Interactions 135, 83 (2001).
3. K – isomers as a probe of nuclear structure and advanced applications, F.G. Kondev in Proc. International Conference on nuclear data for science and technology, AIP Conf. Proc. 769 (2005) p.225.
4. Nuclear isomers: stepping stones to the unknown, P.M. Walker in Proc. 12th International Symposium on Capture gamma-ray spectroscopy and related topics, AIP Conf. Proc. 819 (2006) p.16.
5. Invited lectures in Workshop on nuclear isomers: Structure and applications, May 19 – 21, (2010), University of Surrey, Guildford, UK, www.surrey.ac.uk/physics/news/events/2010/.

Other Review Articles

1. Gamma-rays following (α, xn) reactions, H. Morinaga and P.C. Gugelot, Nucl. Phys. 46, 210 (1963).
2. Compound nuclear reactions induced by heavy ions, T. Darrah Thomas, Ann. Rev. Nucl. Part. Sci. 18, 343 (1968).
3. Nuclear spectroscopy with heavy ions, J.O. Newton, Prog. Nucl. Phys. 11, 53 (1969).
4. Nuclear rotation at high angular velocities, A. Johnson and Z. Szymanski, Phys. Reports., 7, 182 (1973).
5. Nuclear moment of inertia at high spin, Raymond A. Sorensen, Rev. Mod. Phys. 45, 353 (1973).
6. Equilibrium configurations of rotating charged or gravitating liquid masses with surface tension II, S. Cohen, F. Plasil and W.J. Swiatecki, Annals of Physics 82, 557 (1974).
7. Some current themes in nuclear research, A. Bohr and B.R. Mottelson, Phys. Scr. 10 A, 13 (1974).
8. Coriolis effects and rotation alignment in nuclei, F.S. Stephens, Rev. Mod. Phys. 47, 43 (1975).
9. Phenomena in fast rotating heavy nuclei, R.M. Lieder and H. Ryde, Adv. Nucl. Phys. 10, 1 (1978).
10. Lifetime measurements of excited nuclei by Doppler-shift methods, T.K. Alexander and J.S. Forster, Adv. Nucl. Phys. 10, 197 (1978).
11. Nuclei at high angular momentum, R.M. Diamond and F.S. Stephens, Ann. Rev. Nucl. Part. Sci. 30, 85 (1980).
12. Description of high spin states, A. Faessler, M. Ploszajczak and K.W. Schmid, Prog. Part. Nucl. Phys.5, 79 (1981).
13. Collective and single particle motion in deformed nuclei at high spin, B. Herskind, Proc. Int. Conf. Nucl. Phys. – Florence 1983, Vol. II, Eds. P. Blasi and R.A. Ricci, Tipografia Compositori - Bologna (1983) p.117.
14. High spin phenomena in atomic nuclei, M.J.A. de Voigt, J. Dudek and Z. Szymański, Rev. Mod. Phys. 55, 949 (1983).
15. Band crossings at very high spins, Tord Bengtsson, Prog. Part. Nucl. Phys. 9, 523 (1983).
16. Heavy – ion fusion reactions, Ulrich Mosel in Treatise on heavy- ion science, ed. D. Bromley, Vol 2 (1984) p.3.
17. High angular momentum phenomena, Ikuko Hamamoto in Treatise on heavy-ion science, ed. D.A. Bromley, Vol. 3 (1985) p.313.
18. Quasiparticle levels in rotating rare earth nuclei: A cranked shell- model dictionary, R. Bengtsson, S. Frauendorf and F.-R. May, At. Data Nucl. Data Tables 35, 15 (1986).
19. Recent nuclear structure studies in rapidly rotating nuclei, J.D. Garrett, G.B. Hagemann and B. Herskind, Ann. Rev. Nucl. Part. Sci. 36, 419 (1986).
20. Escape suppressed spectrometer arrays: A revolution in γ – spectroscopy, J.F. Sharpey-Schafer and J. Simpson, Prog. Part. Nucl. Phys. 21, 293 (1988).

21. The evolution of nuclear structure at high spin, P.J. Twin in *Trends in Nuclear Physics,* Proc. International School of Physics 'Enrico Fermi', Course CIII, Varenna on Lake Como, 23 June – 3 July 1987, Eds., P. Kienle, R.A. Ricci and A. Rubbino, North Holland (1989) p.201.
22. Pairing fluctuations in rapidly rotating nuclei, Y.R. Shimizu et al., Rev. Mod. Phys. 61, 131 (1989).
23. 'Identical' bands in normally-deformed nuclei, J.D. Garrett, C. Baktash and C.H. Yu in Proc. International Conference on High spin physics and Gamma-soft nuclei, Pittsburgh, U.S.A., September 17-21, 1990, Eds. J.X. Saladin, R.A. Sorensen and C.M. Vincent, World Scientific (1991) p.257.
24. Topics in nuclear structure at high spins, Ikuko Hamamoto, Nucl. Phys. A 522, 63c (1991).
25. Shape coexistence effects of super- and hyperdeformed configurations in rotating nuclei with $58 \leq Z \leq 74$, T.R. Werner and J. Dudek, At. Data Nucl. Data Tables 50, 179 (1992).
26. Tracking the effects of intruder states in nuclei, L.L. Riedinger et al., Prog. Part. Nucl. Phys. 28, 75 (1992).
27. Some new aspects of nuclear structure at high spins, M.A. Deleplanque, Nucl. Phys. A 557, 39c (1993).
28. Rapidly rotating nuclei 1992, B.R. Mottelson, Nucl. Phys. A 557, 717c (1993).
29. Large arrays of escape suppressed gamma-ray detectors, P.J. Nolan, F.A. Beck and D.B. Fossan, Ann. Rev. Nucl. Part. Sci. 44, 561 (1994).
30. Large arrays of escape suppressed spectrometers for nuclear structure experiments, C.W. Beausang and J. Simpson, J. Phys. G: Nucl. Part. Phys. 22, 527 (1996).
31. Signature inversion in odd-odd deformed nuclei, L.L. Riedinger et al., Prog. Part. Nucl. Phys. 38, 251 (1997).
32. Frontiers of nuclear structure, Witold Nazarewicz, Nucl. Phys. A 630, 239c (1998).
33. GRETA: utilizing new concepts in γ - ray detection, M.A. Deleplanque et al., Nucl. Instru. Meth. Phys. Res. A 430, 292 (1999).
34. Experimental methods of nuclear spectroscopy: High spin states, Ranjan K. Bhowmik in *Structure of atomic nuclei,* Proc. SERC School, Puri, India November 18 – December 7, 1996, ed., L. Satpathy, Narosa Publishing House, New Delhi (1999) p. 259.
35. Shape coexistence phenomena in medium mass nuclei, A. Petrovici et al., Prog. Part. Nucl. Phys. 43, 485 (1999).
36. Tilted axis rotation in nuclei, A. Ansari in *Nuclear structure and dynamics,* Proc. Nat. Workshop on Nuclear structure and dynamics, IIT Roorkee, Eds., A.K. Jain and R.K. Bhowmik, August 1999, Phoenix Publishing House Pvt. Ltd., New Delhi (2000) p. 38.
37. Spontaneous symmetry breaking in rotating nuclei, Stefan Frauendorf, Rev. Mod. Phys. 73, 463 (2001).
38. High spin properties of atomic nuclei, David Ward and Paul Fallon, Adv. Nucl. Phys. 26, 167 (2001).
39. Gamma-ray tracking arrays, R.M. Lieder et al., Prog. Part. Nucl. Phys. 46, 399 (2001).
40. High-lying collective rotational states in nuclei, A. Bracco and S. Leoni, Rep. Prog. Phys. 65, 299 (2002).
41. The influence of microscopic structures on rotational motion in nuclei, R. Wadsworth and P.J. Nolan, Rep. Prog. Phys. 65, 1079 (2002).
42. Magnetic moments and nuclear structure, K.-H. Speidel, O. Kenn and F. Nowacki, Prog. Part. Nucl. Phys. 49, 91 (2002).
43. Nuclear magnetic and quadrupole moments for nuclear structure research on exotic nuclei, Gerda Neyens, Rep. Prog. Phys. 66, 633 (2003).
44. Developments in large gamma-ray detector arrays, I.Y. Lee, M.A. Deleplanque and K. Vetter, Rep. Prog. Phys. 66, 1095 (2003).
45. Reaching the limits of nuclear stability, M. Thoennessen, Rep. Prog. Phys. 67, 1187 (2004).
46. The nuclear structure of heavy-actinide and trans-actinide nuclei, M. Leino and F.P. Hessberger, Ann. Rev. Nucl. Part. Sci. 54, 175 (2004).
47. Trends in nuclear physics, A. Richter, Nucl. Phys. A 751, 3c (2005).

48. Mean field description of high spin states, Wojciech Satula and Ramon A. Wyss, Rep. Prog. Phys. 68, 131 (2005).
49. Table of nuclear magnetic dipole and electric quadrupole moments, N.J. Stone, At. Data Nucl. Data Tables 90, 75 (2005).
50. Table of three-quasiparticle rotational bands in deformed nuclei, $153 \leq A \leq 187$, Sukhjeet Singh, Sham Sunder Malik, Ashok Kumar Jain and Balraj Singh, At. Data Nucl. Data Tables 92, 1 (2006).
51. Description of structure and properties of superheavy nuclei, Adam Sobiczewski and Krzysztof Pomorski, Prog. Part. Nucl. Phys. 58, 292 (2007).
52. Shell structure of exotic nuclei, J. Dobaczewski et al., Prog. Part. Nucl. Phys. 59, 432 (2007).
53. From Ge(Li) detectors to gamma-ray tracking arrays – 50 years of gamma spectroscopy with germanium detectors, J. Eberth and J. Simpson, Prog. Part. Nucl. Phys. 60, 283 (2008).
54. Magnetic rotation – past, present and future, A.K. Jain and Deepika Choudhury, Proc. Intl. Symp. Nucl. Phys.- Part I, Eds. R.K. Choudhury, A.K. Mohanty, A. Saxena, K. Mahata and S. Santra, Mumbai, December 8 – 12, 2009, PRAMANA 75, 51 (2010).
55. The AGATA triple cluster detector, Andreas Wiens et al., Nucl. Instru. Meth. Phys. Res. A 618, 223 (2010) and references therein.
56. Gamma-ray tracking detectors: physics opportunities and status of GRETINA, I-Yang Lee, Nucl. Phys. A 834, 743c (2010).

Index

S. C. Pancholi, *Exotic Nuclear Excitations,* Springer Tracts in Modern Physics 242,
DOI 10.1007/978-1-4419-8038-0, © Springer Science+Business Media, LLC 2011